Winter 2003

In-situ study of the influence of additives on the growth behavior of copper electrodeposits on copper single crystal

Aiwen Wu

University of New Hampshire, Durham

IN-SITU STUDY OF THE INFLUENCE OF ADDITIVES ON THE GROWTH BEHAVIOR OF COPPER ELECTRODEPOSITS ON COPPER SINGLE CRYSTAL

BY

Aiwen Wu

MS in Chemical Engineering (1993)
BS in Chemical Engineering (1988)
Tsinghua University, Beijing, China

DISSERTATION

Submitted to the University of New Hampshire
In partial fulfillment of
The requirements for the degree of

Doctor of Philosophy

In

Engineering: Chemical

December, 2003

UMI Number: 3111514

INFORMATION TO USERS

The quality of this reproduction is dependent upon the quality of the copy submitted. Broken or indistinct print, colored or poor quality illustrations and photographs, print bleed-through, substandard margins, and improper alignment can adversely affect reproduction.

In the unlikely event that the author did not send a complete manuscript and there are missing pages, these will be noted. Also, if unauthorized copyright material had to be removed, a note will indicate the deletion.

UMI®

UMI Microform 3111514

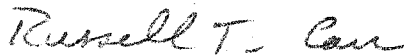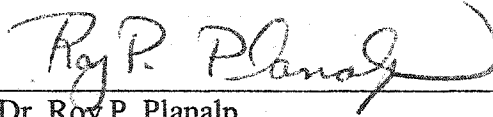This dissertation has been examined and approved.

_____

Dissertation Director, Dr. Dale P. Barkey
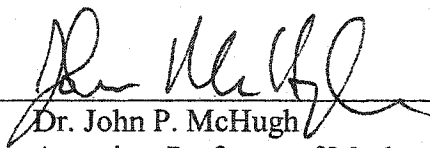Professor of Chemical Engineering

_____

Dr. Palligarnai T. Vasudevan
Professor of Chemical Engineering

_____

Dr. Russell T. Carr
Professor of Chemical Engineering

_____

Dr. Roy P. Planalp
Associate Professor of Chemistry

_____

Dr. John P. McHugh
Associate Professor of Mechanical Engineering

_____
Date

ACKNOWLEDGEMENTS

First and foremost I would like to express my deepest gratitude to my advisor, Dr. Dale P. Barkey, for his support, trust, and guidance during the course of this project. He was always more than willing to help me see a good idea through to its conclusion as well as to contribute ideas of his own. More than through any specific suggestions, however, he has taught by example. If I acquired a small fraction of the insight and grace with which he consistently approaches difficult problems, my years spent in UNH have not been wasted. I consider myself privileged for having had the opportunity to conduct research in the field of electrodeposition under his direction.

I would also like to thank my dissertation committee members, Dr. Russell T. Carr, Dr. Palligarnai T. Vasudevan, Dr. Roy P. Planalp, and Dr. John McHugh, for their careful review of this dissertation and valuable advice.

Many thanks go to Mr. Jonathan E. Newell for his timely help at experimental setup.

I extend my thanks to Dr. Bill Wu, former member of Dr. Barkey's group, for his many helpful suggestions and numerous discussions despite the large distance between us. I truly enjoyed the discussions and learned a great deal.

Finally I wish to thank deeply my wife, Hua Tian, and our parents for their love and support during my studies. They have always expected only the best from me and I owe my achievements to them.

iii

TABLE OF CONTENTS

vi

LIST OF TABLES

LIST OF FIGURES

viii

x

ABSTRACT

IN-SITU STUDY OF THE INFLUENCE OF ADDITIVES ON THE
GROWTH BEHAVIOR OF COPPER ELECTRODEPOSITS ON
COPPER SINGLE CRYSTAL

By

Aiwen Wu

University of New Hampshire, December, 2003

Trace organic additives are known to be essential in obtaining desired metal electrodeposits in the microelectronic industry, however, fundamental design principles for their use and a scientific understanding of their interaction during electrodeposition is lacking. In the present study we investigated electrodeposition of copper on the Cu(100) surface in air-saturated or dearated acid-sulfate plating solutions containing several combinations of chloride and additives benzotriazole (BTA) and 3-mercapto propane sulfonic acid (MPSA) under galvanostatic pulse-current conditions. The electrodeposition process was followed using in-situ atomic force microscopy (AFM). AFM images were quantitatively analyzed by pattern-recognition and scaling procedures.

In the absence of additives, copper deposits grew in a layer-by-layer mode from the earliest stage of deposition. The surface consisted of smooth terraces separated by steps. The scaling analysis result was consistent with a process dominated by surface diffusion and step growth.

In chloride containing solutions, square-pyramidal mounds were initiated and grew to cover the surface. Mound slope increased with deposition time with no indication of reaching a steady-state value. This growth mode was consistent with a surface diffusion mechanism. The scaling result was similar to the additive-free system, but indicated that surface diffusion was more dominant in the presence of chloride.

xi

BTA inhibited the surface and produced nucleation-limited growth at hemispheroidal centers whose height to base radius aspect ratio increased linearly with deposition time. Nucleation and growth of three-dimensional nodules started randomly across the entire surface. The nodules were smaller in size than the mounds observed without BTA. The number and density of nodules were much higher than the mounds density. The deposit growth was dominated by a roughening mechanism that can be described by the random roughening term of a stochastic model.

In the presence of MPSA, growth was not confined to nucleation centers, and the (100) symmetry was visible in the main features. However, pyramidal mounds did not develop. None of the existing models described sufficiently the surface growth mechanism for this case.

Roughening of copper deposits in oxygen-free solution was faster than in oxygen-saturated solution. The results of scaling analysis and pattern-recognition analysis were in agreement with kinetic studies conducted by other researchers. The presence of dissolved oxygen in solutions did not remarkably affect the scaling behavior for each examined solution.

Chapter 1

INTRODUCTION

1.1 Purpose

Over the past decades, electrodeposition phenomenon have been studied through many different approaches due to both its complexity and its industrial importance. Electrodeposition of metals is used in a large variety of process technologies, including electroplating, electroforming, electrorefining, and electrowinning. More recently, electrodeposition has been growing increasingly important in the microelectronics industry due to the continuing trend toward miniaturation, cost reduction, and high-performance packaging. Electrodeposition has had a major impact as an interconnection technology for integrated circuit packages. Among metals, copper is particularly favored as a metallization material due to its conductivity, solderability, reliability, and cost.

Regardless of application, the commercial success of many electrodeposition operations depends on control of deposit morphology. To achieve smooth, uniform deposits with the desired physical properties, trace amounts of organic additives are used in plating baths. Organic additives complicate the electrodeposition process, and little fundamental understanding exists on how such additives affect the growth of deposits and physical properties of electrodeposited metal films. Industrial application of such compounds remains empirical.

1

The average behavior of electrochemical deposition processes on large scales is well described by simple kinetic and transport equations. However, microscopic processes that determine the average macroscopic behavior are not well understood. The development of electrochemically manufactured devices with sub-micron features requires a more complete description of microscopic processes, especially the mediating effect of organic additives during the process. The challenge is to develop models describing molecular processes occurring at the solid-liquid interface and incorporate these models into the existing theory.

Progress in the understanding of electrodeposition process has been helped by new techniques used to probe the solid-liquid interface with atomic resolution and to observe the development of growing electrodeposits. These techniques include atomic force and scanning tunneling microscopes and in-situ spectroscopes. The new in-situ techniques promise to increase understanding of the complex phenomena controlling electrodeposition and to relate macroscopic morphology development to molecular events.

The purpose of the present work was to investigate the copper electrodeposition on copper single crystal surface with a special attention to the influence of organic additives on the growth behavior of copper electrodeposits. The basic electrolyte system was the acid copper sulfate bath with chloride and dissolved oxygen, both of which are usually present in commercial plating baths. They act in a synergistic or competitive way with organic additives under practical conditions. The organic additives, benzotriazole (BTA) and 3-mercapto-1-propanesulfonic acidic sodium salt (MPSA) were chosen due to their widespread use industrially. Atomic force microscopy (AFM) was used to measure

2

surface morphology in-situ at sub-micron length scales. Quantitative information was obtained from AFM images. Scaling analysis and pattern recognition analysis were used to provide a quantitative description of the effect of additives on growth behavior of copper electrodeposits.

1.2 Electrodeposition of Metals

Electrodeposition of metal is performed by immersing a conductive surface in a solution containing ions of the metal to be deposited. The surface is electrically connected to an external power supply and current is passed through the solution into the surface. This causes reaction of the metal ions M^{n+} with electrons (e^-) to form metal M:

$$M^{n+} + ne^- = M \tag{1.1}$$

The process of metal electrodeposition is considered to proceed in at least three steps, as shown in Figure 1.1. [1]

1. Transport of metal ions from the bulk solution to the interface.

2. Adsorption of metal ions onto the electrode surface and transfer of electrons at the electrode to form adatoms.

3. Surface diffusion of adatoms, nucleation, and growth.

Step 1 is a bulk mass-transport process. The flux of each species in the electrolytic solution is governed by the transport equation, which accounts for the contribution of migration, diffusion, and convection: [2]

$$N_i = -n_i \mu_i F C_i \nabla \Phi - D_i \nabla C_i + C_i V \tag{1.2}$$

3

where N_i is molar flux of species i. The first term on the right side represents the transport by migration in the electric field $\nabla\Phi$. The second term represents transport by diffusion and is proportional to the gradient of concentration ∇C_i. The last term represents transport by convection with the fluid velocity V. n_i is the charge number carried by an ion, μ_i is the mobility of an ion, and F is Faraday constant. D_i is the diffusion coefficient of species i.
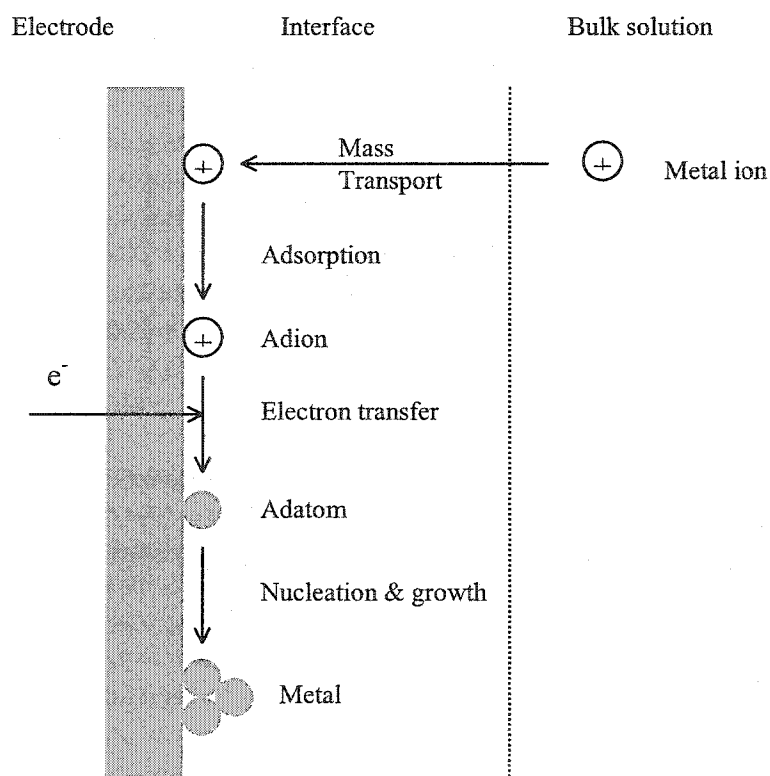
Figure1.1 Steps involved in the process of metal electrodeposition.

4

In electrodeposition, the activated kinetics of ionic discharge is important. The driving force for the electrode reaction is the surface overpotential η_s. The overpotential is defined as the deviation of the electrode potential Φ from its equilibrium value Φ_e, which describes equilibrium between the electrode and the solution in contact with it.

$$\eta_s = \Phi - \Phi_e \qquad (1.3)$$

The rate of the electrode reaction is the rate of deposition of metals, and can be measured by the current density at the electrode. The current density depends on the driving force and is thus related to the surface overpotential. Copper deposition is often well described by the Butler-Volmer equation:

$$i = i_0[\exp(\frac{\alpha_a F}{RT}\eta_s) - \exp(-\frac{\alpha_c F}{RT}\eta_s)] \qquad (1.4)$$

where i_0 is exchange current density, a kinetic parameter that depends on the composition at the interface and the temperature. α_a and α_c are transfer coefficients. The parameters i_0, α_a, and α_c can be obtained from experimental polarization curve of the current density i versus the overpotential η_s.

If the overpotential applied to the electrode becomes sufficiently negative, all metal ions that reach the electrode react. The rate becomes transport limited and reaches a constant maximum known as the limiting current density i_l

$$i_l = k_l n F C_b \qquad (1.5)$$

5

where k_l is the mass transfer coefficient which depends on electrode geometry and flow conditions and C_b is the bulk concentration of metal ions.

Figure 1.2 shows a current-potential curve typical of an electrodeposition process. As potential is scanned from the equilibrium potential to more negative values, the current increases in an exponential manner (Tafel region) where the overall deposition rate is determined largely by charge transport at the cathode. As potential continues to increase, mass transport becomes predominant, and a limiting current is reached. At this condition the concentration of metal ions at the electrode surface is zero.
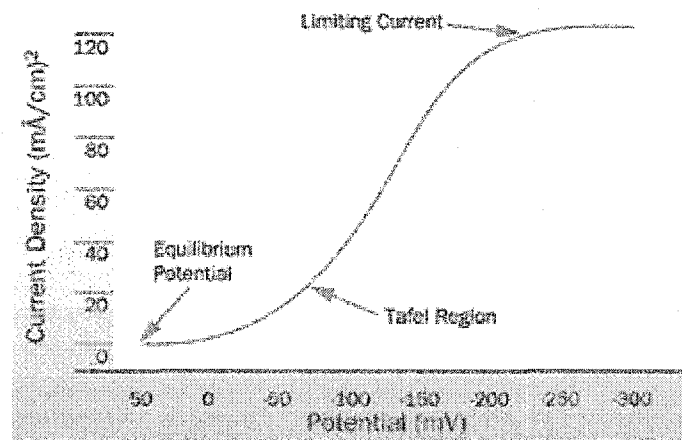
Figure 1.2 Current-potential curve typical of an electrodeposition process.

The growth velocity of deposit is proportional to the current density i

$$\vartheta = \frac{i\widetilde{V}}{nF} \tag{1.6}$$

where ϑ is the growth velocity, $\widetilde{V}$ is molar volume of metal, and n is the number of electrons transferred in discharging the ion to the metal state.

6

1.3 Atomistic Aspects of Electrodeposition of Metals

In the electrodeposition of metals a metal ion M^{n+} is transferred from solution onto the metal surface. A simplified atomistic representation of the this process is

$$M^{n+}(solution) \Rightarrow M \ (surface) \qquad (1.7)$$
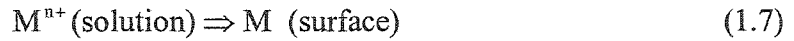
Atomic processes that constitute the electrodeposition process can be seen by presenting the structure of the initial, M^{n+}(solution), and the final state, M(surface). Since metal ions in the aqueous solution are hydrated the structure of the initial state in Equation (1.7) is represented by $[M(H_2O)_x]^{n+}$. The structure of the final state is the M adion (adatom) at the kink site. Thus, the final step of the overall reaction, Equation (1.7), is the incorporation of M^{n+} adion into the crystal lattice. Because of surface inhomogeneity the transition from the initial state $[M(H_2O)_x]^{n+}$ to the final state M(crystal)

$$[M(H_2O)_x]^{n+} (solution) \Rightarrow M(crystal) \qquad (1.8)$$

can proceed via either of two mechanisms: (1) step-edge site ion-transfer mechanism or (2) terrace site ion-transfer mechanism. [3][4]

Step-Edge Ion-Transfer Mechanism. The step-edge site ion-transfer, or direct transfer mechanism, is illustrated in Figure 1.3. It shows that ion transfer from the solution takes place on a kink site of a step edge or on any other site on the step edge. In both cases the result of the ion transfer is a M adion in the metal crystal lattice. In the first case, a direct transfer to a kink site, the M adion is in the half-crystal position, where it is

7

bonded to the crystal lattice with one half of the bonding energy of the bulk ion. In the second case, a direct transfer to the step edge other than kink, the transferred metal ion diffuses along the step edge until it finds a kink site. Thus, in a step-edge site ion-transfer mechanism there are two possible paths: direct transfer to a kink site and the step-edge diffusion path.

Solution ion

Kink atom
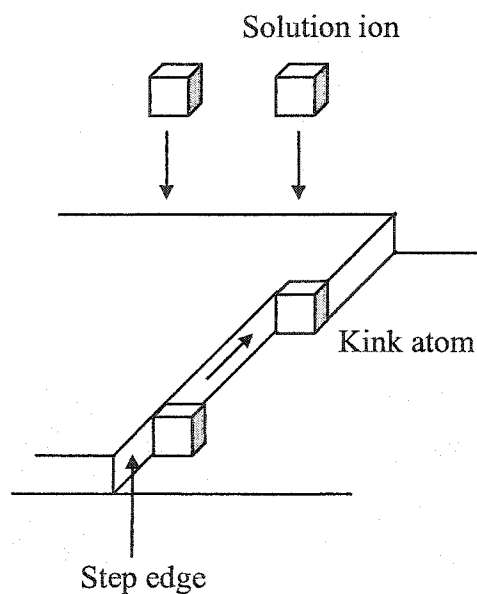
Step edge

Figure 1.3 Schematic of step edge ion-transfer mechanism.

Terrace Ion-Transfer Mechanism. In the terrace site transfer mechanism a metal ion is transferred from the solution to the flat face of the terrace region (Figure 1.4). At this position the metal ion is in the adion state having most of its water of hydration. It is weakly bound to the crystal lattice. From this position it diffuses on the surface, seeking a position of lower energy. The final position is a kink site.

8

Solution ion
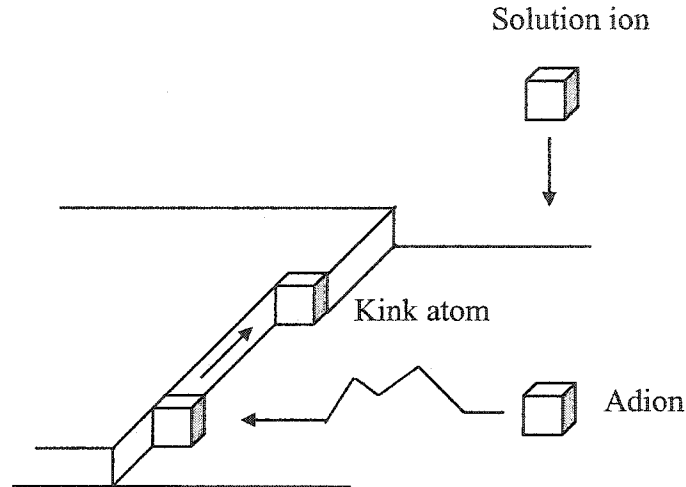
Figure 1.4 Schematic of terrace ion-transfer mechanism. Ion transfer to the terrace site, surface diffusion, and incorporation at kink site.

The relevant microscopic processes taking place on the crystal interface include deposition, desorption, and surface diffusion. The morphology of the interface is determined by the interplay between them. Lorenz[5] studied the electrodeposition of Cu, and found that only one tenth or less of the surface area participated in the crystallization process. He concluded that surface diffusion was highly hindered and direct ion transfer and attachment played a predominant role in Cu deposition. However, Schmidt et al.[6] analyzed AFM images of copper electrodeposits in acid sulfate solution by means of scaling analysis and attributed surface texture to surface diffusion.

1.4 Roughening of a singular surface

Generally the surface types can be sorted into three categories: a) fully rough or self-affine, b) smooth, and c) singular or vicinal.

9

The concept of self-affinity is described mathematically by the following relation:

$$H(r) = \kappa' H(\kappa r) \qquad\qquad (1.9)$$

where H(r) is the height at point r on the surface. If a surface, $\kappa' H(\kappa r)$ is indistinguishable from H(r), then H is self-affine.

In metal electrodeposition, deposits are grown far away from equilibrium conditions. The way in which a singular (atomically flat) surface roughens during growth under non-equilibrium conditions has been the subject of extensive theoretical study. One theoretical approach to the problem of surface roughening during growth is the dynamic scaling hypothesis, often termed kinetic roughening. The general formalism, proposed by Family and Vicsek[7], presumes that the growth surface evolves into a temporal and scale invariant structure. The theoretical expectation is that roughening during crystal growth can lead to a self-affine surface that exhibits dynamic scaling. Typically the dynamic scaling of the correlation functions is reflected in power law behavior in space and time (see Section 4.3.1). Since the corresponding exponents do not depend on the microscopic details of the system under investigation it is possible to divide growth processes according to the values of these characteristic exponents into kinetic universality classes. The association with one particular class depends only on a few properties of the growth dynamics like conservation laws, the importance of defects in the growing film, etc. The determination of these relevant features is one of the important problems that have to be addressed by the theory of kinetic roughening. Conversely, as soon as these relations are known the determination of scaling exponents allows conclusions about the physical processes that dominate the growth dynamics. The details of the scaling theory will be described in Chapter 4.

Chapter 2

LITERATURE REVIEW

2.1 Copper Electrodeposition

Copper is the most extensively used plating metal due to its high conductivity and low resistivity. It is electrodeposited for a number of engineering and decorative applications that require a wide range of mechanical and physical properties. Two important applications of electrodeposited copper involve its use in the through-holes of printed circuit board and as microelectronic interconnects. The use of copper in the fabrication of interconnects in microelectronics devices is a significant development in materials in the semiconductor industry. Electrodeposition has become the preferred method of depositing copper for interconnects. It offers a number of advantages including high yield, excellent fidelity of shape replication and pattern transfer, ease of producing high respect ratio structures, rapid processing and relatively low cost.[8]

Acid copper sulfate plating solutions containing copper(II) sulfate and sulfuric acid are widely used for the plating of printed circuit board and microelectronic interconnects. These plating baths provide the relative thick, ductile, and rapidly-formed copper deposits needed in the microelectronics industry.[9]

11

Compared to other metals electrodeposition of copper is relatively simple since electrodeposition can proceed without hydrogen evolution for a wide range of conditions and in an acid solution, copper is free of a surface oxide.[10]

Copper is largely present as cupric ions in acid copper baths, but small amount of cuprous ions are often present especially when complexes are formed with organic addition species.[11]

Mattson and Brockris[12] studied deposition and dissolution of copper in acidic copper sulfate solution using galvanostatic method. It was found that the reaction obeyed the Butler-Volmer equation and that the transfer coefficients α_a and α_c based on experimental measurement were close to the theoretical values 1.5 and 0.5, respectively. They proposed a two-step electron transfer mechanism for copper electrodeposition at acidic sulfate solution with Cu^+ as an intermediate. The process composed of two elementary reactions:

$$Cu^{2+} + e^- \longrightarrow Cu^+ \qquad (2.1)$$

$$Cu^+ + e^- \longrightarrow Cu \qquad (2.2)$$
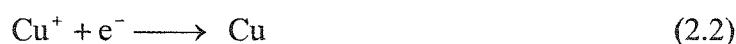
The redox reaction between Cu^{2+} and Cu^+ was found to be the rate controlling reaction while Cu^+ exists in reversible equilibrium with Cu at the electrode surface. This was later verified by many other researchers using different methods. [13-17]

Gerischer[18] reported a ratio of approximately 1:10 between the exchange current density of reaction (2.1) and reaction(2.2). Albaya et al.[19] examined the copper electrodeposition from acidic copper sulfate electrolyte using galvanostatic pulse method.

12

The exchange current density of reaction (2.2) was found to be three orders of magnitude larger than that of reaction (2.1). Chassaing et al.[20] concluded that the charge transfer mechanism is independent of the substrate by performing impedance measurements on various copper substrates.

The presence of Cu^+ has been verified experimentally using a rotating ring disk electrode (RRDE), but the source of intermediate, Cu^+, has been a topic of debate. It has been suggested that the disproportion reaction:

$$Cu + Cu^{2+} \longrightarrow 2Cu^+ \tag{2.3}$$

could also be a source of the intermediate ion Cu^+. De Agostini et al. showed that the source of the intermediate (either reaction (2.1) or (2.3)) depended on the age of the copper surface.[21] They proposed that reaction (2.3) dominated on freshly deposited surfaces and that chemical equilibrium kept the Cu^+ intermediate concentration constant. On surfaces that have undergone some aging, such as surface oxidation, reaction (2.1) facilitated the generation of Cu^+. It follows that when the formation of Cu^+ is dominated by reaction (2.1), reaction (2.2) has to be slow, and vice-versa. If the above situation was not true we would have an equilibrium between the Cu^{2+}/Cu species which has not been observed experimentally. It is clear that most experimental studies indicate the formation of copper deposits to be dominated by a two-step reaction mechanism described by reactions (2.1) and (2.2). However, it has also been shown not be a unique path for the reduction of copper during electrodeposition.

13

2.2 Use of Organic Additives during Copper Electrodeposition

In many copper electrodeposition applications, small amounts of organic materials are introduced into the plating bath, which have specific functions in the deposition process. These additives, often adsorbed at the cathode surface, affect the kinetics and growth mechanism of electrodedposition and consequently modify the structure, morphology, and properties of the resulting deposits. Additives are classified according to their function, such as levelers, brighteners, structure modifiers, and wetting agents.[22] The use of additives can also assist in causing the electrodeposition to occur preferentially in the bottoms of high aspect ratio trenches used in microelectronic industry. This results in copper deposits that are free of seams and voids, leading to better microelectronic device performance.[23] During the course of electrodeposition, the additives can be consumed by incorporation into the deposits and/or electrochemical reaction at the cathode or anode.[24]

A large variety of additives are used in copper electrodeposition. A list of additives covered in patents granted from 1973-1995 is included in reference.[24] Many of these additives contain nitrogen or sulfur. Although additives have been used for decades, most development and use of additives have been of a more empirical nature, and there is a lack of fundamental understanding of their role in the electrodeposition process. Plating baths typically contain more than one additive, and how these additives work in conjunction with one another is not yet fully understood.[9] A number of questions have been raised in the search for fundamental understanding of the action of additives in the electrodeposition process. The following is a list of some of these questions.

14

- How do the additives interact with copper and each other as a function of potential?

- How do the additives interact with the growing copper deposit?

- What decomposition products of the additives are produced during the electrodeposition process?

- How do the additives affect both the kinetics and growth mechanism of electrodeposition and the structure and properties of the resulting electrodeposit?

- How does the mode of action of the additives relate to their molecular structure?

- How do the additives affect electrodeposition in trenches and vias of the scale used in the microelectronic industry?

A variety of in-situ microscopic, electrochemical, and spectroscopic techniques are used in an attempt to explore the answers to these and other questions relating to the effect of additives on copper electrodeposition.

The influence of additives on copper electrodeposition kinetics has been studied by various techniques. Electrochemical and spectroscopic measurements[25-27] showed that polyethylene glycol (PEG) and chloride ions act cooperatively to inhibit the deposition. Electrochemical quartz crystal microbalance measurements showed a synergistic interaction of PEG and chloride ions in inhibiting the deposition.[28] Using electrochemical techniques, copper deposition was found to be retarded in the presence of thiourea and benzotriazole.[29] A complex electrode process was suggested. The impact of a range of nitrogen-containing and sulfur-containing compounds on copper deposition was evaluated by cyclic voltammetry, and inhibition of underpotential deposition of copper on gold was reported.[30]

The effect of additives on morphology of the deposits has been examined by scanning tunneling microscopy (STM) and atomic force microscopy (AFM). Copper deposition with benzotriazole,[6][31] sulfonium-alkane-sulfonate,[32] and thiourea[6][33] yields smoother deposits compared to deposits obtained from additive-free solutions. Addition of sodium dodecyl sulfate, however, leads to a three-dimensional growth of copper.[34] The effects of multi-additive plating baths were investigated using electron microscopes, and additive-additive interactions were found to be crucial to the leveling activity.[35] The influence of additives on quasi two-dimensional growth of copper deposits has been examined.[36]

2.2.1 Benzotriazole

Benzotriazole (BTA) been widely studied and used as both corrosion inhibitor and as electrodeposition additive.[37-47] The generalized molecular structure of BTA is shown as:
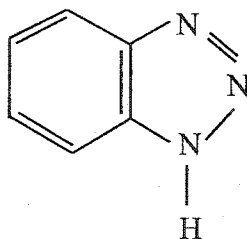
The inhibiting effect of BTA during electrodeposition is thought to be due to a complex formation mechanism, however the nature of the complex is still a topic of debate. BTA in acid copper sulfate solutions has been shown to form both cupric and cuprous complexes.[37] It was reported that the cuprous BTA complex, Cu(I)BTA, was the only stable complex in an aerated solution.[40] Vogt et al. found that the formation of

Cu(I)BTA was potential-dependent and was affected by the BTA concentration and solution pH.[41] At BTA concentrations above 200 μM, Cu(I)BTA was found to precipitate on the surface. It was further proposed that the electrodeposition process proceeded through the formation of the intermediate complex Cu(I)BTA. [40] At open circuit, BTA adsorbs on the substrate surface. When a current is passed, cupric ions first reduce into cuprous ions. The cuprous ions form a polymeric complex with the adsorbed BTA.

$$Cu^{2+} + e^- \longrightarrow Cu^+ \tag{2.4}$$

$$Cu^+ + BTA \longleftrightarrow Cu(I)BTA \tag{2.5}$$

Subsequently, the cuprous complexes reduce, and the copper atoms are released.

$$Cu(I)BTA + e^- \longrightarrow Cu + BTA \tag{2.6}$$

Reduction of Cu(I)BTA continues concomitant with diffusion of cupric ions to the interface and formation of Cu(I)BTA complex (reaction 2.4 and 2.5). Copper deposits nucleate and grow as more copper adatoms release. The "free" BTA may form polymeric complexes with cuprous ions. Another route for the free BTA is to include into copper deposits.

Surface-enhanced Raman spectroscopy (SERS) was used to elucidate the surface structure of the Cu(I)BTA complex. The results supported earlier findings that a film of Cu(I)BTA was formed.[42][43] A recent SERS study suggested that BTA and deprotonated

17

BTA⁻ interacted with copper through the triazole nitrogen with their molecular planes perpendicular (or tilted) to the surface.[43] Calculation suggested that the polymeric complex was in the form as:[44]
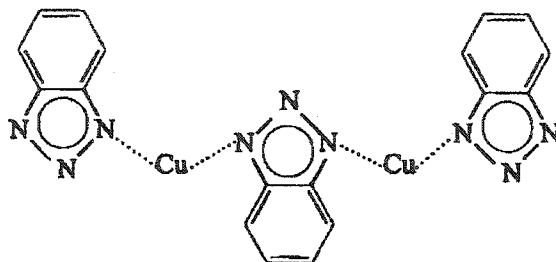
Loshkarev et al. however argued that the additive concentration of BTA used during electrodeposition was too small to complex with a significant fraction of copper and that direct adsorption of BTA had to account for the observed inhibition.[45] It was further shown that the effectiveness of BTA as deposition inhibitor increased with pH.[45][46]

BTA incorporated into electrodeposits at high current densities (> 70 mA/cm^2) has been reported.[47] The incorporation of BTA supports an adsorption mechanism mediating the inhibition process. However, the exact nature of the adsorbed species is still unclear. Both the cuprous complex and BTA appear to mediate the inhibition process through adsorption at the interface.

BTA has been shown to influence the surface morphology of copper electrodeposits.[38][39] Concentration as low as 10^{-6} M BTA has been shown to significantly alter surface morphology.[38] STM results by Armstrong and Muller[39] suggested that BTA eliminated preferential growth of specific crystallographic planes and imposed uniform kinetics.

18

Schmidt[6] et al. studied the effects of BTA on copper electrodeposition using in-situ AFM and found an increase in the nuclear number density. They showed that BTA promoted smooth copper deposits.

2.2.2 SPS and MPSA

Although the use of BTA in acid copper plating solutions does produce smoother copper deposits, BTA is not used in modern commercial plating baths. Bis-(3-sulfopropyl)-disulfide (SPS) and its thiol analog, 3-mercapto-1-propanesulfonate acid (MPSA), are currently used in commercial plating baths, especially in microelectronics industry. The structural forms of SPS and MPSA are shown as follows:

$$SPS: \quad SO_3^- - (CH_2)_3 - S - S - (CH_2)_3 - SO_3^-$$

$$MPSA: \quad SO_3^- - (CH_2)_3 - SH$$
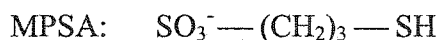
Farndon et al.[48] studied the effect of the additive SPS on the deposition of copper from acid sulfate solutions using potential sweep techniques and found that the kinetics for copper deposition were more favorable in the presence of SPS. They showed that SPS was first electroreduced to MPSA. MPSA then reduces Cu^{2+} to produce a Cu(I) thiolate complex and SPS is regenerated. The SPS can again be reduced while the Cu(I) complex undergoes reduction to produce copper metal and MPSA. A possible reaction mechanism was proposed as follows:

19

$$HO_3S(CH_2)_3SS(CH_2)_3SO_3H + 2H^+ + 2e^- \longleftrightarrow 2HS(CH_2)_3SO_3H \qquad (2.7)$$

$$
\begin{aligned}
4HS(CH_2)_3SO_3H + 2Cu^{2+} &\longrightarrow 2Cu(I)S(CH_2)_3SO_3H \\
&+ HO_3S(CH_2)_3SS(CH_2)_3SO_3H + H^+ + e^-
\end{aligned}
\qquad (2.8)$$

$$Cu(I)S(CH_2)_3SO_3H + H^+ + e^- \longrightarrow Cu + HS(CH_2)_3SO_3H \qquad (2.9)$$
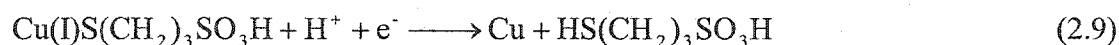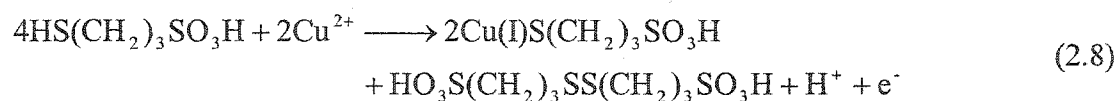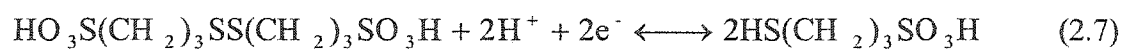
SPS is therefore able to participate in repeated oxidation and reduction cycles and depolarization occurs because Cu^{2+} reduction to Cu^+ occurs chemically in reactions involving the additive in contrast to a purely electrochemical Cu^{2+} to Cu^+ electroreduction process.

It has also been shown that SPS and MPSA have a significant effect on the structure of copper electrodeposits. Using scanning electron microscopy (SEM) and transmission electron microscopy (TEM), Kelly and West [35][49] investigated the role of SPS in the copper deposition on microprofiled electrodes from an acid copper sulfate solution containing polyethylene glycol (PEG) and Cl. SEM and TEM micrographs showed that the additive SPS removed the columnar structure of the deposit and affected micro-sized, unoriented grains. Moffat et al.[50] demonstrated superfilling electrodeposition of copper in 500 nm trenches ranging from 500 nm to 90 nm in width using an acid copper sulfate electrolyte containing Cl, PEG, and MPSA additives. The films deposited from Cl-PEG-MPSA electrolyte exhibit spontaneous recrystallization at room temperature that results in a drop in resistivity.

2.3 Effects of Chloride ions on Copper Electrodeposition

The chloride ion (Cl⁻) is a common additive in commercial electrodeposition baths and is one of the few non-organic additives. It is generally agreed that Cl⁻ is a complexing ligand and that Cl⁻ even in small concentration can increase the reaction rate of copper electrodeposition from acidic sulfate solutions.[51] In Cl⁻-containing sulfate plating system, Cl⁻ ions form complexes with Cu^+ and Cu^{2+}, such as $CuCl$, $CuCl_2^-$, and $CuCl_3^{2-}$.[52] The complex formation in this system is controlled by chloride concentration. At low chloride concentration, the complex $CuCl_2^-$ is predominant, and $CuCl_3^{2-}$ complex formation is negligible.[53]

The deposition reactions in the presence of chloride ions probably proceed as

$$Cu^{2+} + 2Cl^- + e^- \longrightarrow CuCl_2^- \qquad (2.10)$$

$$CuCl_2^- + e^- \longrightarrow Cu + 2Cl^- \qquad (2.11)$$
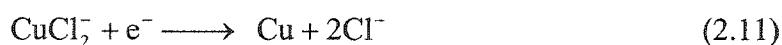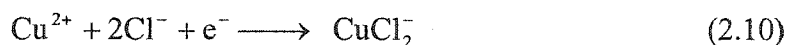
where Equation (2.11) is the rate-limiting step.

The sparingly soluble CuCl is also present in the Cl⁻-containing acidic sulfate solutions. The following reactions also take place during the cathodic polarization of copper

$$Cu^+ + Cl^- \longrightarrow CuCl \qquad (2.12)$$

$$CuCl + Cl^- \longrightarrow CuCl_2^- \qquad (2.13)$$

21

Yoon et al.[54] proposed that there was a "critical Cl⁻ concentration" for the formation of such an insoluble CuCl film on the electrode surface. Above the "critical Cl⁻ concentration", CuCl is precipitated on the metal surface by reaction (2.12) and dissolved to $CuCl_2^-$ by reaction (2.13). Wu showed that chloride promotes the cathodic reduction process even in the trace amounts.[55] However, when the chloride concentration is further increased to 10 mM, the cathodic reduction process is blocked due to CuCl film formation. He concluded that chloride ion changes the reaction mechanism of copper deposition.

Several mechanisms have been proposed to explain the catalytic effect of chloride ion on the deposition of copper. Shi et al.[51] and Ehlers et al.[56] reported that Cl⁻ was much more readily adsorbed on metal surfaces than sulfate, therefore, Cl⁻ had a substantial surface coverage even in the presence of sulfate. It has been postulated that the increase in reaction rate is caused by the adsorbed Cl⁻ complexing with the metal ion. Chloride stabilizes cuprous ion by forming complexes with it, effectively increasing the amount of cuprous ions diffusing to electrode surface from cupric to cuprous reaction.[57][58] Another explanation for the increase in reaction rate is through ion bridging where the complexed ion accelerates the flow of electrons from the electrode to the metal ion.[59]

In acidic sulfate solutions the Cl⁻ has been shown to accelerate the copper discharge.[20] Chassaing and Wiat[20] studied the effects of Cl⁻ in copper electrodeposition using impedance analysis. They found that chloride accelerated the second electron transfer reaction found in reaction (2.2).

The trace amounts of Cl⁻ in copper sulfate solution have been shown to have a significant influence on the deposit electrocrystallization and morphology. Chassaing and

22

Wiat[20] found that Cl⁻ promoted epitaxial growth on Cu(100) and Cu(110). Pradhan et al.[60] reported chloride had a significant effect on cryatallographic orientations of copper deposits. At low concentration of chloride, the (220) plane is predominant, whereas at high concentration the (111) plane is predominant.

Gauvin and Winkler[61] showed that addition of chloride as sodium chloride to the acidic sulfate solution (0.55M CuSO₄/1.5M H₂SO₄) had no obvious influence on copper deposition when the concentration of sodium chloride was below 9 mg/L. Above this concentration, the copper deposits become fine grained.

Nageswar and Setty[62] reported that chloride ions present in acidic sulfate solution modified the growth forms of copper electrodeposited on Cu(100) surface. At a Cl⁻ concentration of 10^{-4} mol/L, there was breaking of layers producing a ridge type of growth. At a Cl⁻ concentration of 3.5×10^{-3} mol/L, pyramids were observed. At 10^{-2} mol/L, triangle pyramids of CuCl were formed and at higher chloride concentration, polycrystalline deposits were produced. Nageswar also extended the study of the effect of chloride ions on the morphology of copper electrodeposits on Cu(111) plane,[63] and found that in the presence of chloride ions the pyramidal type of growth on a Cu(111) plane changed to a layer type of growth due to specific adsorption of chloride ions.

Moffat[64] used in-situ scanning tunneling microscopy (STM) to examine the influence of chloride ion adsorption on the structure of steps on copper surfaces. Chloride is shown to form potential dependent adlayer structures on Cu(100) and Cu(111) which strongly affects the orientation of the surface steps. The adlayer acts as a template guiding step evolution during metal deposition. Moffat also examined step faceting and disordering on Cu(100) caused by adsorption of chloride in the solution without copper

23

ions.[65] Vogt et al.[66] observed that an ordered overlayer of chloride on Cu(100) reversibly stabilizes the [100] step direction, and suggested that faceting of the step is induced by the overlay geometry. Wu and Barkey,[67] using AFM, imaged faceted monoatomic steps on Cu(111) in an acid copper sulfate solution containing 2mM chloride at low current density during deposition, and measured the velocity of singular steps. More recently, they also observed faceting of Cu(100) surface induced by chloride.[68]

As an additive chloride is not used alone but in combination with other additives like polyethylene glycol (PEG). It is believed that there is some kind of interaction between PEG and Cl⁻ when used as an electrodeposition additive.[69] There are many examples in the literature about additives when used alone do not produce a significantly good deposit, but the quality of the deposit is dramatically increased when combined with other additives.[70]

In the present research, the chloride-containing electrolyte was 0.2 M CuSO$_4$/1.0 M H$_2$ SO$_4$/1.0 mM HCl. Two additional solutions were produced by adding 0.1 mM MPSA or 0.1 mM BTA to the solution. Appendix A contains the calculations of equilibrium composition for the chloride solutions used in the present research. The results are presented in Table 2.1 below.

Table 2.1 Equilibrium composition: 0.2 M CuSO$_4$/1.0 M H$_2$ SO$_4$/1.0 mM HCl

$[Cu^+]$	3.622×10^{-5} M	$[Cu^{2+}]$	0.1997 M	$[Cl^-]$	6.519×10^{-4} M
$[CuCl]_{aq}$	1.183×10^{-5} M	$[CuCl_2^-]$	1.771×10^{-5} M	$[CuCl_3^{2-}]$	1.003×10^{-8} M
$[Cu_2Cl_4^{2-}]$	2.342×10^{-9} M	$[CuCl^+]$	3.007×10^{-4} M	$[CuCl_2]$	5.516×10^{-8} M
$[CuCl_3^-]$	2.102×10^{-11} M	$[CuCl_4^{2-}]$	2.957×10^{-15} M	$[H^+]$	2.001 M
$[SO_4^{2-}]$	1.2 M	$[Cl^-]_{Total}$	0.001 M		

2.4 Effects of Oxygen on Copper Electrodeposition

Dissolved oxygen is of particular interest since it is normally present in industrial copper sulfate plating systems through sparging system or simple exposure to air. As discussed before, in copper electrodeposition from acid sulfate solution, the reduction of cupric ion to metal proceeds through two elementary steps. In solutions exposed to air, dissolved oxygen consumes the cuprous ion[71]

$$Cu^+ + \frac{1}{4}O_2 + H^+ \longrightarrow Cu^{2+} + \frac{1}{2}H_2O \qquad (2.14)$$
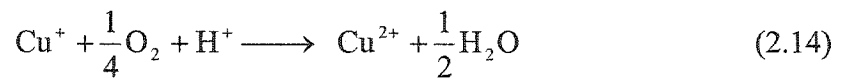
Barkey et al.[72] proposed a mechanism where oxygen diffuses to a reaction-plane within the diffusion layer and oxidizes the cuprous diffusing away from the electrode surface. Since oxygen and cuprous react rapidly and irreversibly in solution at a reaction plane within the diffusion layer,[11] at steady state, no cuprous exists outside the reaction-plane and no oxygen exists between the electrode surface and the reaction-plane. One of the effects due to this reaction-plane is that cuprous and therefore cuprous complexes with organic additives are limited to the region between the reaction-plane and the electrode surface. The cupric hydrate limits its activity with these additives. The additives diffuse to the region within the reaction-plane where they function as desired. Therefore, the presence of dissolved oxygen in solutions may improve the effectiveness of additives.

In sulfate plating solutions containing both chloride and dissolved oxygen, chloride and oxygen are competitors in the copper cathodic reduction process since chloride ions stabilize the cuprous ions while oxygen oxidizes the cuprous ions. The influence of chloride may be greater than that of oxygen because chloride is more strongly adsorbed

on the electrode surface, and chloride changes the deposition mechanism and increases the reaction rate.

2.5 SPM Studies of Copper Electrodeposition

The experimental techniques used to studies the kinetics of metal electrodeposition generally rely on information that originates from the entire electrode surface and represents the integration of the contributions from individual locations on the electrode. Although this characteristic may not be important for the study of homogeneous surfaces, it can be critical for the study of energetically inhomogeneous surfaces such as a metal electrode which have a variety of features like steps, kinks, and screw dislocations that affect local rate of processes occurring during electrodeposition. A breakthrough in the study of structural problems came through the introduction of local probe microscopies, particularly STM and AFM, which are characterized collectively as scanning probe microscopies (SPM). Both techniques employ a sharp and sensitive probe which is scanned over a surface and senses the variations of a physical parameter as a function of the position on the surface, therefore can map the height variation on the sample. The application of SPM to structural problems at the electrified solid-liquid interface is one of the most important advances in electrochemistry over the past decade.[73]

Nanoscale study of the solid-liquid interface has been greatly enhanced by the development of the Atomic Force Microscope (AFM) since its introduction by Binnig et al in 1985.[74] AFM enables in-situ examination of atomic level details on surfaces. Furthermore, it does not require an electrically conductive sample for image generation. It works equally well on dielectrics, including metal oxides or adsorbed organic films.

26

This is not the case with Scanning Tunneling Microscope (STM) or Scanning Electron Microscope (SEM). The use of an inert tip makes this technique especially suitable for work in electrochemical environments.

AFM and other in-situ imaging techniques are powerful tools that can produce images of events directly at the liquid-solid interface during electrodeposition. Such images provide a rich source of qualitative observations that can test hypotheses of mechanism. However, the utility of qualitative results can be enhanced by a more quantitative treatment of information contained in such images. Based on methods for quantitative analysis of surfaces grown at the gas-solid interface, Schmidt et al.[6] proposed a procedure for extracting quantitative information from AFM images. They applied this method to analyze the AFM images of growing copper deposits from additive-free and additive-containing acidic sulfate solutions to provide insight into the mechanism of their growth. For additive-free deposits, it was concluded that surface morphology was dominated by surface diffusion. In solutions containing benzotriazole, surface diffusion was strongly inhibited. In solutions containing thiourea, growth was dominated by three-dimensional island formation. The different mechanisms suggested for each solution indicate that this quantitative image analysis shows promise and its refinement for electrodeposition application is worthy of further study.

27

Chapter 3

EXPERIMENTAL

3.1 Introduction

Copper electrodeposits on copper single crystal formed in acid copper sulfate electrolyte under galvanostatic conditions were imaged with a commercially available AFM, NanoScope E (Digital Instruments, Santa Barbara, CA).

In order to examine the influence of chloride and organic additives on the growth behavior of copper electrodeposits, experiments were performed in conventional sulfate plating solutions of 0.2M $CuSO_4$/1.0M H_2SO_4 containing typical low concentrations of HCl and organic additives. In addition, air-saturated and deaerated solutions were used respectively to examine the effect of oxygen on the surface growth.

3.2 Experimental Setup

The main experimental setup is shown in Figure 3.1 and 3.2. It consists of a Digital Instruments NanoScope E atomic force microscope equipped with a 14 μm scanner, a standard AFM fluid cell obtained from Digital Instruments, and a computer-controlled EG&G Instruments VersaStat II Potentiostat/Galvanostat for controlling the current applied to the fluid cell. The AFM fluid cell is equipped with a gold-coated spring clip which holds a tip assembly. The assembly contains a pyramidal Si_3N_4 45° tip mounted on

28

a gold-coated 200 μm V-shaped silicon cantilever. The cantilevers have a force constant of 0.06 N/m.

3.2.1 AFM operation

The working principle of an AFM is based on the deflection of a very sensitive cantilever due to repulsive forces between atoms on the sample surface and atoms at the cantilever tip. This deflection is measured using a laser beam while the sample is scanned. Scanning in the horizontal, or X, Y direction, as well as motion in the vertical, or Z direction, are performed by a piezo-electric translator. The computer subsystem controls the xyz translations and records the reflected laser beam signal. Dedicated software reconstructs these data into a topographic picture of the sample surface based on either a height or a deflection feedback mode. Figure 3.3 shows the principle of measurement of an AFM.

In height mode, the displayed data comes from the voltage output to the Z piezo. A feedback loop directs the Z piezo to move the sample up or down to maintain a constant cantilever deflection. The Z piezo signal thus describes the surface height as function of position in the X-Y plane. Because the total force applied on the sample is constant, this mode is also referred as *Constant Force* mode.

29
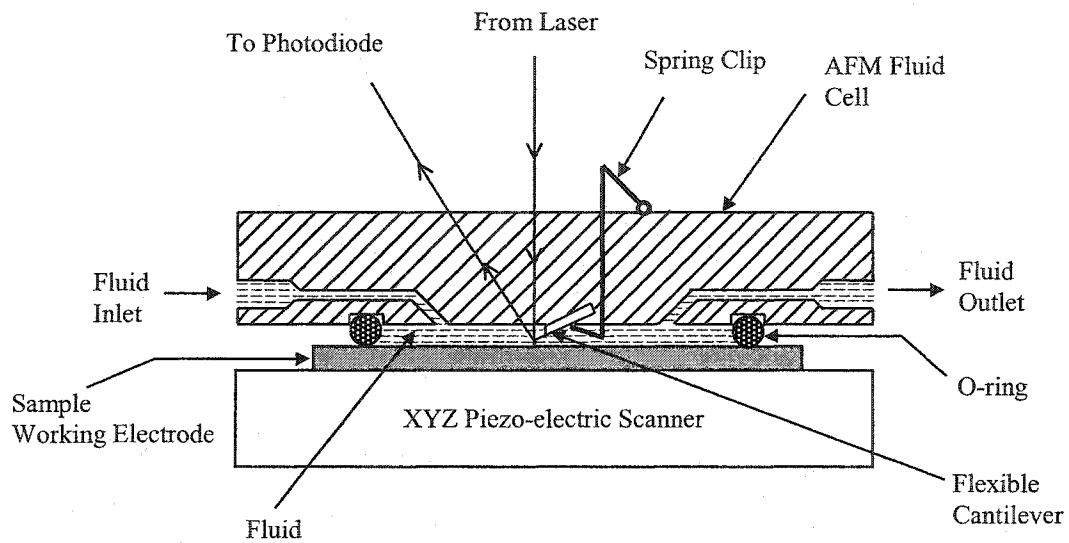
Figure 3.1 Schematic view of the AFM electrochemical cell for in-situ study of metal electrodeposition.

30

AFM with Electrochemical Cell

Optical Head

Reference Electrode

Counter Electrode

Digital NanoScope E Controller

Sample

Working Electrode

EG&G VersaStat II Potentiostat/ Galvanostat

Tip

Base

Scanner
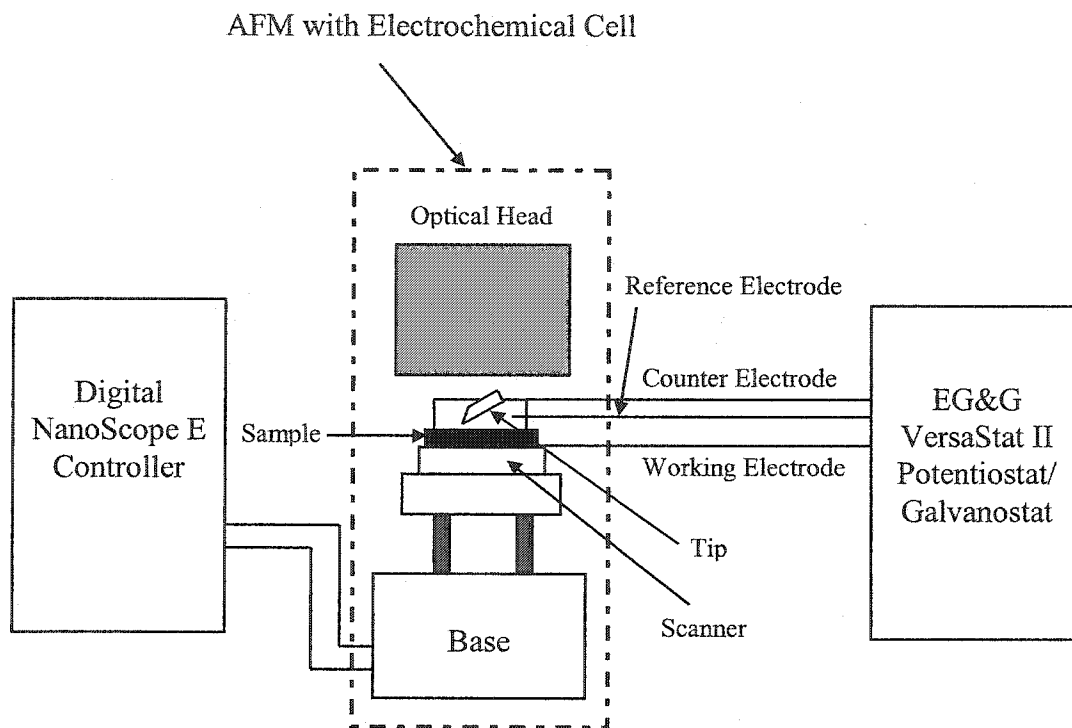
Figure 3.2 Schematic illustration of AFM in-situ examination of a sample surface in electrolyte under electrochemical control using a Potentiostat/Galvanostat.

31

In deflection mode, the cantilever is held at constant height and the cantilever deflection signal is captured and displayed. This data describes the surface height. This mode is also referred as *Constant Height* mode.
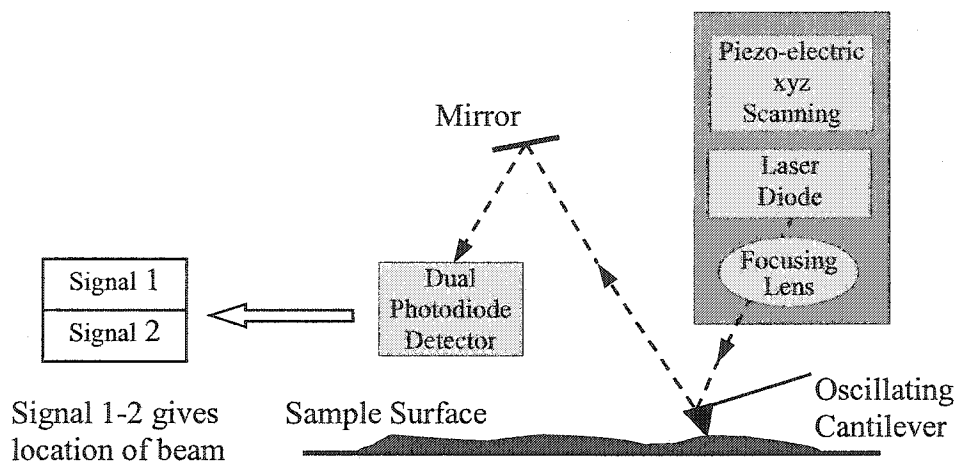
Figure 3.3 The principle of measurement of an atomic force microscope.

3.2.2 Electrochemical Cell

A commercially available fluid cell, supplied by Digital Instruments, was used for in-situ electrodeposition experiments. The cell was made of glass and had an indentation where the cantilever was placed and held in place with a spring clip (see Figure 3.1). A sulfuric acid-resistant ethane propylene diethylene O-ring (35 durometer) was fitted between the fluid cell and the sample and defined the side walls of the electrochemical cell. The sample and the bottom surface of the fluid cell comprise the bottom and top walls of the electrochemical cell respectively. The surface area exposed to solution during electrodeposition was 0.3 cm^2. Two glass tubes were fitted to the inlet and outlet ports of the fluid cell to hold electrolyte solution (not shown in Figure 3.1). Solution was

then driven into the cell through the inlet and outlet ports. Solution driving can often be problematic since slow driving may result in the formation of bubbles in the cell, which interfere with imaging and disrupt electrical conduct between the working and counter electrodes.

A copper single-crystal disk of orientation (100) (99.999%, 12 mm in diameter and 2mm thick, Monocrystals Incorporated) was mounted on the top of the scanner and was used as working electrode. A single crystal plane is preferred to study the electrochemical behavior of copper electrodeposition since it possesses a well-defined crystal orientation while the surface of polycrystalline copper is an irregular ensemble of randomly oriented crystal planes. The use of single crystal plane allows for a more uniform initial surface for electrodeposition experiments. The counter electrode was a piece of coiled copper wire fitted in the outlet tube of the fluid cell.

3.2.3 Power Supply for the Electrochemical Cell

An EG&G VersaStat II Potentiostat/Galvanostat system controlled by a computer (Compaq Presario 5000) with Head Start Creative Electrochemistry Software (EG&G PARC, Version 1.70) installed was used for galvanostatic pulse-current electrodeposition experiments. The maximum potential and current output capability for this system are 20V for potentiostatic and 200 mA for galvanostatic control, respectively.

In this research, galvanostatic deposition was selected over potentiostatic since it corresponds to constant flux of material to the surface, a condition that is implied in scaling analysis of vapor deposited surfaces.[75] The use of galvanostatic pulse-current deposition technique can lead to electrodeposits with improved physical properties such

33

as smaller grain size, greater brightness, and less internal stress than those prepared with conventional direct-current methods.[76]

To prevent the interfacial concentration of copper ions falling to less than 70% of the bulk concentration, a square-wave pulse-current program was imposed. A current waveform for the galvanostatic pulsed electrodeposition is illustrated in Figure 3.4. In this study, the pulse-on period, t_{on} and the relaxation period, t_{off}, were set to 1 second and 9 seconds, respectively. i_p is the peak-pulse current, which was set to 10mA, corresponding to about 30mA/cm^2 current density.
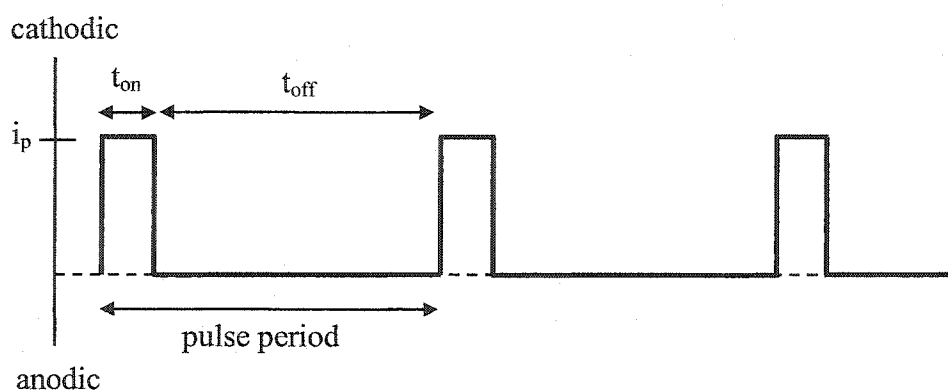
Figure 3.4 Current waveform for pulsed electrodeposition.

3.3 Experimental Materials and Preparation

3.3.1 Substrate Preparation

The copper single-crystal disk was first mechanically polished using a fine grinding/polishing system, which comprises a Struers RotoPol-11 polishing machine and a Struers RotoForce-1 sample mover (Struers Inc., Westlake, OH). The sample surface was polished with diamond compounds of 6 and 3 μm particle size as well as colloidal silica suspension successively.

34

Figure 3.5 shows the schematic view of the grinding/polishing machine setup. In a grinding/polishing process, the samples are held by a rotating specimen mover plate with the polished surface facing the horizontal rotating polishing wheel. On the top of the wheel is a removable abrasive cloth on which the lubricant or colloidal silica suspension is poured. The specimen mover plate and wheel rotate in the same direction and speed but with the two rotating axes offset by some distance. The rotating speed of the specimen mover plate and wheel and the pressure applied on the samples can be varied by adjustment of the control panel. A lubricant delivery system is used to quantify the amount of lubricant applied to the polishing process.

The polishing procedures are outlined below.
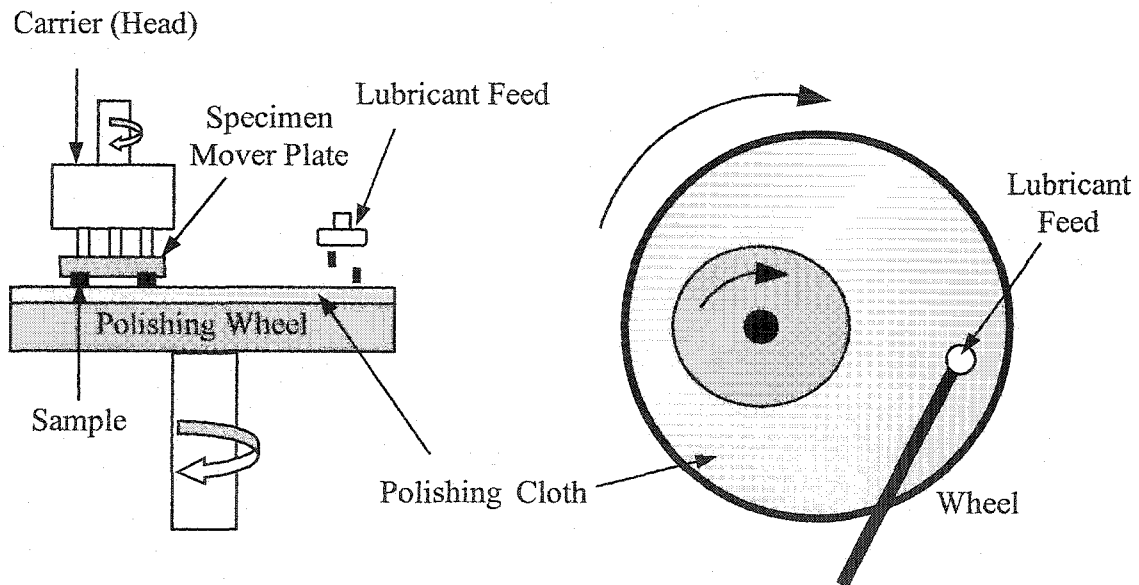
Figure 3.5 Schematic diagram of a grinding/polishing machine.

Step #1 Grind sample until surface is uniform and perpendicular to disc axis

Rotating speed	150 rpm
Disc surface	Cloth MD-Pan (Struers catalogue # 40500083)
Diamond compound	6 μm DP-Spray (Struers catalogue # 40600135)
Total load (Newtons)	25
Lubricant	Ultrapure Water
Lube dosing	7 drops per minute
Time	5-20 minutes, depends on the sample initial quality
Etchant	none
Clean sample	Rinse with ultrapure water

Step #2 Polish sample until surface is uniform and scratch free

Rotating speed	150 rpm
Disc surface	Cloth MD-Mol (Struers catalogue # 40500077)
Diamond compound	3 μm DP-Spray (Struers catalogue # 40600136)
Total load (Newtons)	20
Lubricant	DP-Lubricant Red, HQ (Struers catalogue # DEPPO)
Lube dosing	7 drops per minute
Time	5 minutes
Etchant	none
Clean sample	Rinse with ultrapure water

36

Step #3 Polish/Etch sample until surface is uniform and mirrorlike

Rotating speed	150 rpm
Disc surface	Cloth MD-Chem (Struers catalogue # 40500092)
Total load (Newtons)	20
Lubricant	OP-S Suspension (Struers catalogue # 40700000) (see Etchant recipe)
Lube/Etchant dosing	1) Wet entire disc surface prior to polish (w/5ml) 2) Then dose the surface again after 20 seconds (w/5ml) 3) Then dose the surface w/copious amounts of ultrapure water after 40 seconds have elapsed
Time	1 minute
Etchant	Make etchant solution immediately before use 1) 10 ml of OP-S Suspension in 50ml beaker 2) Add 6 drops (0.2 ml of NH_4OH) to same beaker 3) Add 9 drops (0.3 ml of H_2O_2) to same beaker

Step #4 Clean sample until surface is uniform, mirrorlike, and deposit free

Clean in ethanol	1) Insert disk sample, polished side up, into ethanol. 2) Insert test tube into the Ultrasonic cleaning apparatus for one minute.
Rinse in ultrapure water	1) Insert disk sample, polished side up, into ultrapure water. 2) Insert test tube into the Ultrasonic cleaning apparatus for one minute.
Dry	Remove and shake sample, gently tamp the polished surface edge with a clean Kim-wipe to wick the remaining water from the surface.

Prior to each experiment, the sample was electropolished in 85% phosphoric acid for 2 minutes at a constant voltage of 2 V. Polishing was followed by successive rinses in concentrated sulfuric acid (96%), 10% nitric acid, 10% sulfuric acid, and ultrapure water.

3.3.2 Solution Preparation

Four plating solutions were used to study the growth behavior of copper electrodeposits under air-saturated and deaerated conditions.

(1) 0.2M $CuSO_4$/1.0M H_2SO_4

(2) 0.2M $CuSO_4$/1.0M H_2SO_4/1.0mM HCl

(3) 0.2M $CuSO_4$/1.0M H_2SO_4/1.0mM HCl/0.1mM BTA

(4) 0.2M $CuSO_4$/1.0M H_2SO_4/1.0mM HCl/0.1mM MPSA

Chemical reagents used for the preparation of electrolyte solutions are listed in Table 3.1.

Table 3.1 Chemical reagents used in the experiments

Chemicals	Formula	Content (%)	Source
Cupric sulfate pentahydrate	$CuSO_4 \cdot 5H_2O$	99.999	Aldrich
Sulfuric acid	H_2SO_4	95.5 – 96.5	EM Science
Hydrochloric acid	HCl	34.3	J. T. Baker
Benzotriazole (BTA)	$C_6H_5N_3$	99	Aldrich
3-mercapto-1-propanesulfonic acid, sodium salt (MPSA)	$HS(CH_2)_3SO_3Na$	90	Aldrich

38

All of the solutions were made with ultrapure water produced in a Nanopure II Ultra-filtration system. The resistivity of the water was 17-18 mΩ·cm.

In some experiments, the solutions, assumed to be air saturated, were directly driven into the fluid cell. In others, the solutions were first stored in a closed glass vessel and deaerated by sparging ultrapure nitrogen (99.99%, Northeast Airgas) for 40 minutes before being introduced into the AFM cell through PTFE tubing. Under this anaerobic environment, a piece of copper was placed in the reservoir to ensure equilibrium between solution and metal. The nitrogen was further purified by passing it through an indicating oxygen trap (VWR) before sparging it into the vessel.

3.3.3 Cleaning of Electrochemical Cell

A strict cleaning protocol was followed since trace mounts of impurity affect the growth of electrodeposits. All the glassware used in the experiment was first washed with hot water and mild detergent, rinsed with tap water and ultrapure water. It was then immersed in hot fuming sulfuric acid (96%) for 10 minutes, rinsed three times with ultrapure water, then boiled in ultrapure water for 10 minutes, and finally rinsed three times with ultrapure water and air-dried.

Great care must be taken in cleaning the fluid cell used in the AFM study. The cell was immersed in Nochromix (Godax Lab Inc.) concentrated sulfuric acid cleaning solution for several minutes to remove organic contaminants and metal. Immersion in the cleaning solution was carefully done in a way as to avoid contact between the acidic solution and the cantilever clip. After cleaning, the cell was rinsed thoroughly with copious amounts of ultrapure water.

39

Cleaning of the O-ring consisted of two steps. In the first step the O-ring was immersed in a warm solution of mild detergent for two hours. It was then rinsed thoroughly with ultrapure water, immersed in a 1:1 (vol.) mixture of water and H_2SO_4 for two hours, finally rinsed with ultrapure water.

3.4 Experimental Procedures

The single-crystal copper disk of (100) orientation was mounted on the scanner and the O-ring was put on the top of the disk. The optical head with attached fluid cell was placed in the center of disk with the O-ring fitting into the V-groove on the bottom of the fluid cell. Head stabilizing springs were installed and the head was leveled with a set of screws. The glass tubes were fitted into the inlet and outlet ports of the fluid cell. Then electrolyte solution was then driven into the fluid cell, and the working, counter, and reference electrode were connected to the galvanostat.

The AFM was engaged after adjustment of the laser signal. Images were captured in height and deflection mode simultaneously. Galvanostatic pulse-current electrodeposition experiments were performed at a current density of 30 mA/cm^2. AFM images (8 μm x 8 μm) of surface morphology were acquired after intervals of five current pulses. During the electrodeposition process for the solutions containing organic additives, the AFM tip was held in a small (10 nm x 10 nm) scanning region. After five current pulses the scanning size was increased to 8 μm x 8 μm and a surface image was captured. This technique of capturing AFM in-situ data was used to eliminate tip removal of organic additives adsorbed on the substrate at the area of interest. After an image was captured the fluid cell was flushed by the fresh solution to prevent the copper depletion in the

40

solutions. By repeating the electrodeposition, imaging and flushing steps, a sequence of images of copper electrodeposits on the single crystal copper were obtained for further qualitative and quantitative analysis. Cumulatively, the current was applied to the solution for 50 seconds, which corresponds to about 0.6 μm of deposited metal, and ten images were obtained for each deposition experiment.

41

Chapter 4

RESULTS AND DISCUSSION

4.1 Introduction

Deposits were formed on copper single crystal disks of (100) orientation using a galvanostatic pulse-current deposition technique. A current density of $30mA/cm^2$ was used to simulate practical deposition rates. A short pulse-on period of 1 second was used to avoid depletion of metal ions and transport-limited growth. The morphology of deposits was characterized as a function of deposition time for additive-free and additive-containing solutions under air-saturated and deaerated conditions. Four different plating solutions were used:

(1) 0.2M $CuSO_4$/1.0M H_2SO_4

(2) 0.2M $CuSO_4$/1.0M H_2SO_4/1.0mM HCl

(3) 0.2M $CuSO_4$/1.0M H_2SO_4/1.0mM HCl/0.1mM BTA

(4) 0.2M $CuSO_4$/1.0M H_2SO_4/1.0mM HCl/0.1mM MPSA

Approximately three runs were carried out for each solution under air-saturated and deaerated conditions respectively. For each experiment, images were taken with $8\mu m$ scan size. The number of data points taken per scan line was 512. Images were then exported into an ASCII format with 512x512 Z-direction data points for data analysis. Scaling analysis and pattern-recognition procedures were used to analyze

42

electrodeposited surfaces grown from each solution. With the use of theoretical models, scaling analysis provided a statistical description of the spatial and temporal changes of the surface during the course of electrodeposition,[75][77] while pattern-recognition procedures were applied to identify and analyze the shapes of individual surface features.[78]

4.2 Results

These experiments were carried out at current densities of technological interest. Deposition produced changes too rapidly for representative images to be captured in real time. It was found that the images captured at open circuit were reproducible, and the surface did not change significantly during the off-time. Therefore, each image presented below represents the morphology observed at the end of a given period of deposition. Taken together, each series of AFM images represents evolution of deposit growth at the same location on the substrate surface as a function of deposition time.

4.2.1 Air-saturated 0.2M CuSO$_4$/1.0M H$_2$SO$_4$

Figure 4.1(a) - (e) shows a time sequence of AFM images captured during electrodeposition from air-saturated 0.2M CuSO$_4$/1.0M H$_2$SO$_4$ solution after deposition times of 10, 20, 30, 40, and 50 seconds. The crystal was clearly observed to grow in a layer-by-layer fashion from the earliest stage of deposition. The layer type of deposits formed with side faces, or macro-steps, all running in one direction. The surface consisted of smooth terraces 400 to 800 nm wide and separated by steps with a height of 6 to 10 nm. Although the change of surface structure was very slow, there was a gradual

43

decrease of distance between successive steps with increasing deposition time as layers caught up with neighboring layers. Initially the steps were oriented 45° from the (100) direction. Eventually, the steps were parallel to the (100) direction. Such a growth mode may be explained by supposing that addition occurs preferably on the edges of layers surface, rather than on their surface.

4.2.2 Deaerated 0.2M $CuSO_4$/1.0M H_2SO_4

Figure 4.2(a) - (e) represents a sequence of images of electrodeposition from deaerated 0.2M $CuSO_4$/1.0M H_2SO_4 solution after deposition times of 10, 20, 30, 40, and 50seconds. The growth of deposits was similar to that observed in air-saturated solution. The morphology of copper deposits was layer growth with straight layer edges. Compared to the deposits formed in air-saturated solution, the distance between the successive steps and the height of steps were smaller, and all the steps were parallel to the (100) direction from the beginning of deposition.
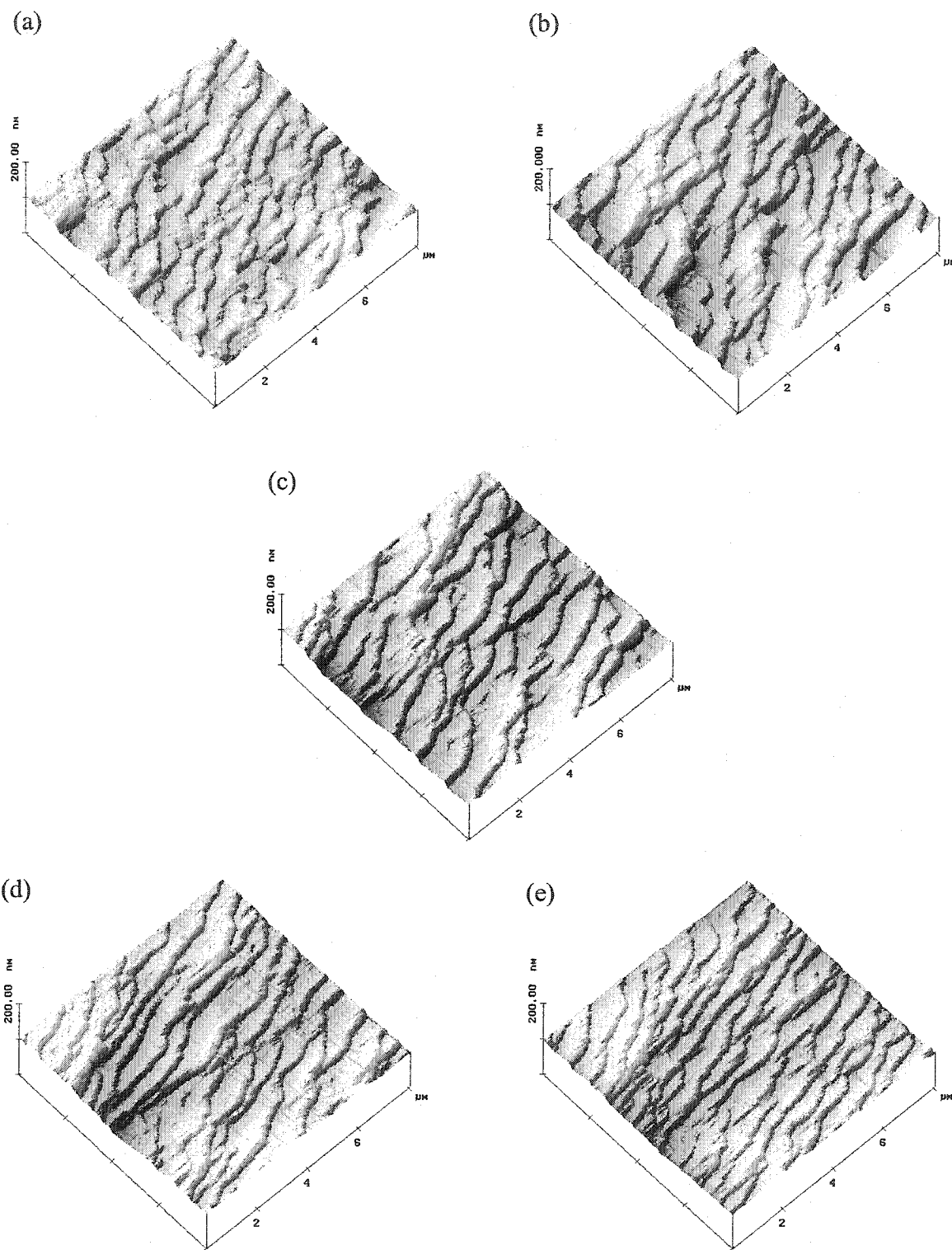
Figure 4.1 AFM images of Cu electrodeposition on single crystal copper from air-saturated 0.2M $CuSO_4$/1.0M H_2SO_4 solution at current density of 30 mA/cm^2 for deposition time of (a) 10s, (b) 20s, (c) 30s, (d) 40s, (e) 50s.

45
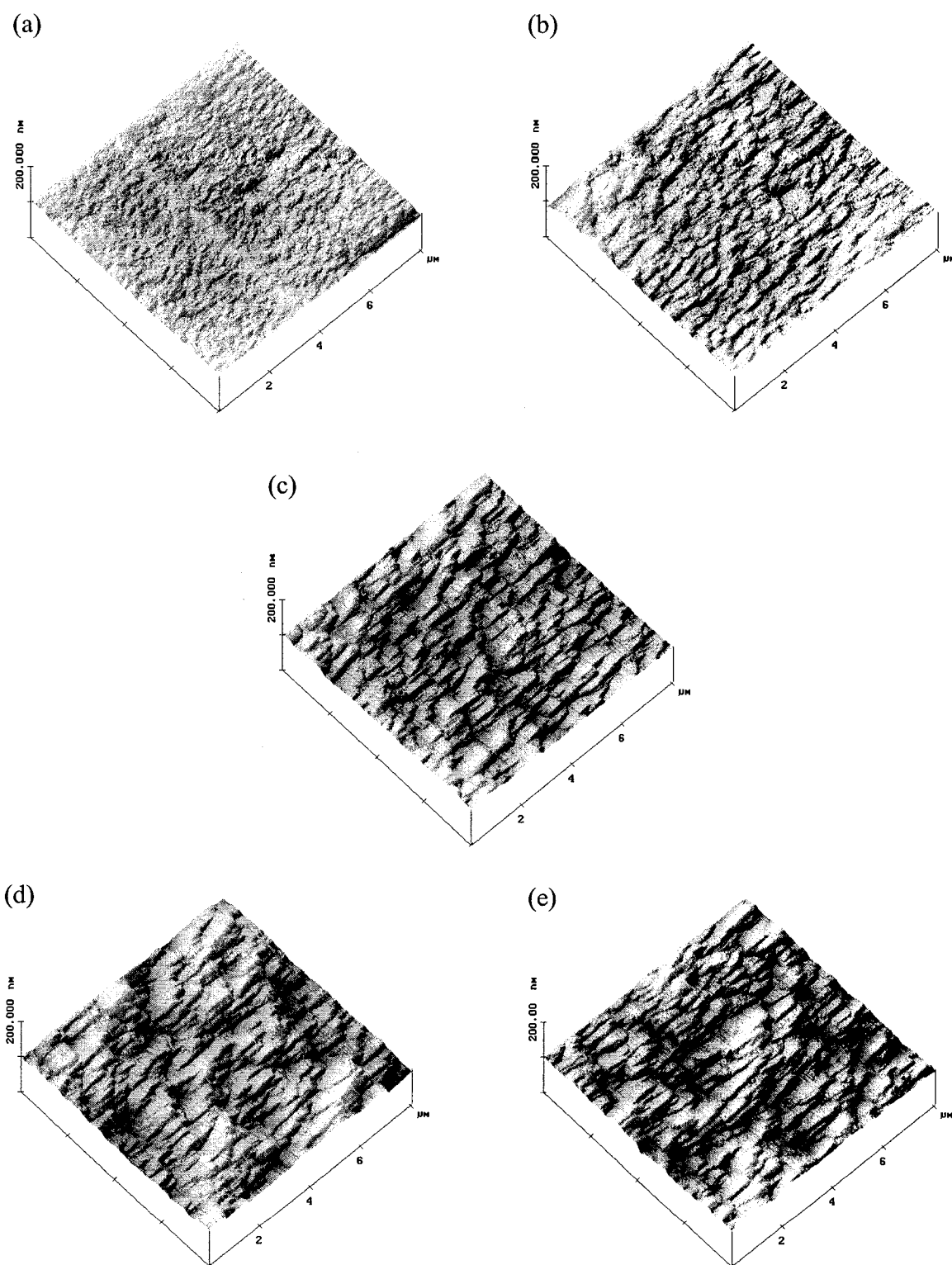
Figure 4.2 AFM images of Cu electrodeposition on single crystal copper from deaerated 0.2M CuSO₄/1.0M H₂SO₄ solution at current density of 30 mA/cm² for deposition time of (a) 10s, (b) 20s, (c) 30s, (d) 40s, (e) 50s.

46

4.2.3 Air-saturated 0.2M CuSO$_4$/1.0M H$_2$SO$_4$/1.0mM HCl

Figure 4.3 shows a series of AFM images of copper deposited from air-saturated 0.2M CuSO$_4$/1.0M H$_2$SO$_4$/1.0mM HCl solution after 10, 20, 30, 40, and 50 seconds. As shown in Figure 4.3 (a), at the very early stages of deposition, the shape of the deposits might not be well defined, but later the larger features appeared to be developing a better-defined shape (see Figure 4.3 (c)-(e)). The deposits consisted of extremely regular truncated square pyramids with edges parallel the (100) direction. The pyramids were observed to become quite large (*ca.* 1.5 μm) as deposition progressed. As more copper was deposited on the surface, the individual pyramids were seen to increase in size. However, no additional pyramids were observed to form after the formation of the initial ones. It is noteworthy that the faces of pyramidal side contained steps. In contrast to the layer growth mode seen in additive-free solution, a three-dimensional growth-mode was dominant in solutions containing Cl$^-$, although steps were still observed on the faces of the features. These observations indicate that Cl$^-$ has a strong influence on morphology of copper deposits.

4.2.4 Deaerated 0.2M CuSO$_4$/1.0M H$_2$SO$_4$/1.0mM HCl

Figure 4.4 shows a series of AFM images of copper deposited from deaerated 0.2M CuSO$_4$/1.0M H$_2$SO$_4$/1.0mM HCl solution after 10, 20, 30, 40, and 50 seconds. The main features were the same as those seen in Figure 4.3. The deposits were composed of square-pyramidal mounds. The number of mounds did not increase with deposition time, although their size increased.

Figure 4.3 AFM images of Cu electrodeposition on single crystal copper from air-saturated 0.2M CuSO₄/1.0M H₂SO₄/1.0mM HCl solution at current density of 30 mA/cm² for deposition time of (a) 10s, (b) 20s, (c) 30s, (d) 40s, (e) 50s.

48

Figure 4.4 AFM images of Cu electrodeposition on single crystal copper from deaerated 0.2M CuSO$_4$/1.0M H$_2$SO$_4$/1.0mM HCl solution at current density of 30 mA/cm^2 for deposition time of (a) 10s, (b) 20s, (c) 30s, (d) 40s, (e) 50s.

49

4.2.5 Air-saturated 0.2M CuSO$_4$/1.0M H$_2$SO$_4$/1.0mM HCl/0.1mM BTA

Figure 4.5 shows a series of images depicting the evolution of deposit morphology obtained from air-saturated 0.2M CuSO$_4$/1.0M H$_2$SO$_4$/1.0mM HCl/0.1mM BTA solution. Nucleation and growth of three-dimensional nodules started randomly across the entire imaged surface. The number of growth centers did not significantly change during the course of the deposition, while the existing centers increased gradually in size. This is indicative of an instantaneous nucleation process. After deposition of 50 seconds the size of individual nodules reached a few hundred nanometers in base width. The initial nodules did not merge with neighboring nodules. When compared to the very large pyramids formed from a solution containing only Cl⁻ (see Figure 4.3 (e)), the nodules were smaller in size, and randomly distributed over the imaging area, and the number density of nodules was considerably higher. The morphological differences between Figure 4.5 and Figure 4.3 indicate that BTA also significantly affects the deposition behavior of copper.

4.2.6 Deaerated 0.2M CuSO$_4$/1.0M H$_2$SO$_4$/1.0mM HCl/0.1mM BTA

Figure 4.6 provides a series of AFM images copper deposition from deaerated 0.2M CuSO$_4$/1.0M H$_2$SO$_4$/1.0mM HCl/0.1mM BTA solution. The growth was clearly similar to that observed in the same solution when saturated with air. Randomly distributed nuclei formed across the surface. Each individual nucleus continued to develop with time, and new nuclei did not form at later deposition times. The surface was dominated by the growth of the initial nuclei.
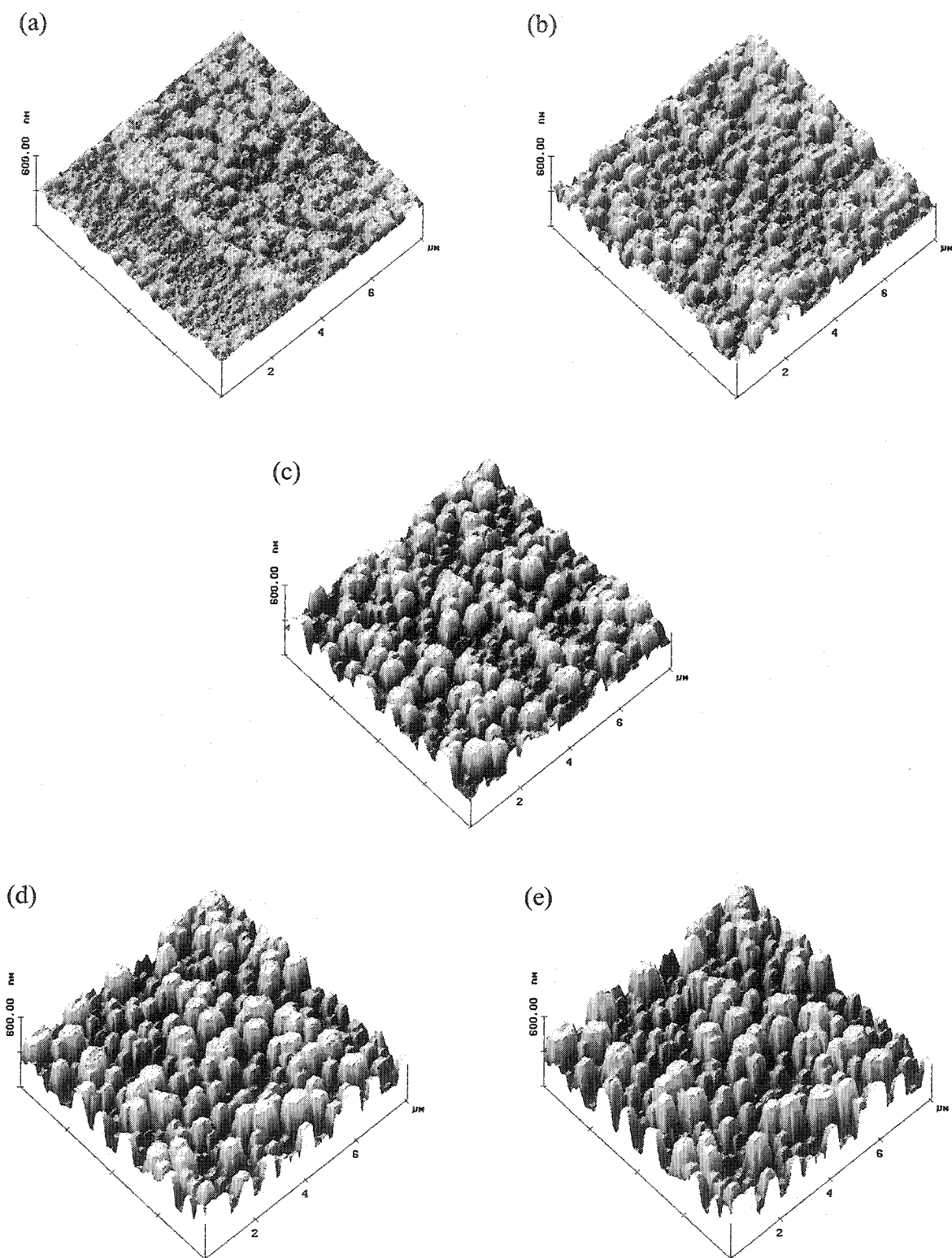
Figure 4.5 AFM images of Cu electrodeposition on single crystal copper from air-saturated 0.2M CuSO$_4$/1.0M H$_2$SO$_4$/1.0mM HCl/0.1mM BTA solution at current density of 30 mA/cm^2 for deposition time of (a) 10s, (b) 20s, (c) 30s, (d) 40s, (e) 50s.

51
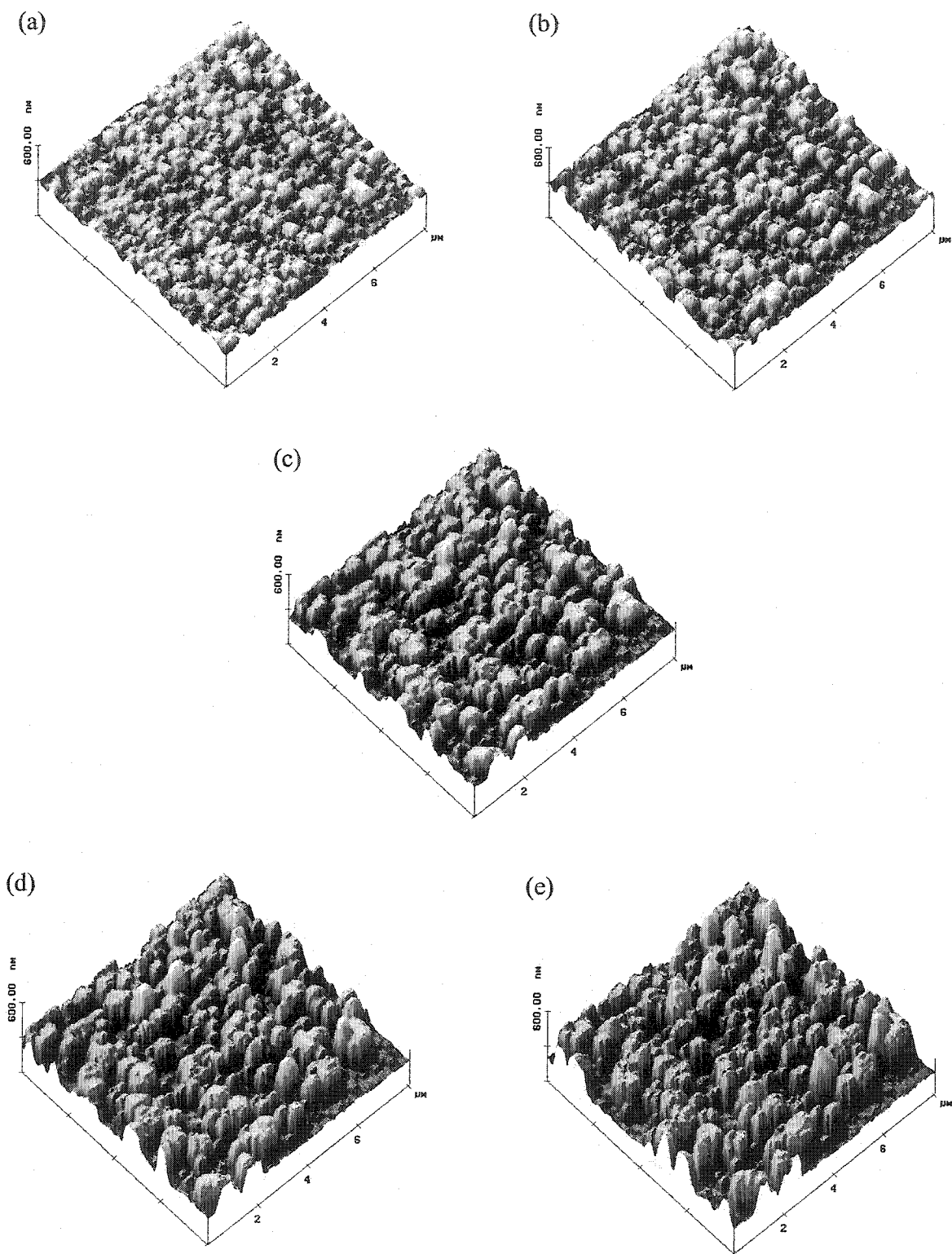
Figure 4.6 AFM images of Cu electrodeposition on single crystal copper from deaerated 0.2M $CuSO_4$/1.0M H_2SO_4/1.0mM HCl/0.1mM BTA solution at current density of 30 mA/cm^2 for deposition time of (a) 10s, (b) 20s, (c) 30s, (d) 40s, (e) 50s.

4.2.7 Air-saturated 0.2M CuSO$_4$/1.0M H$_2$SO$_4$/1.0mM HCl/0.1mM MPSA

Figure 4.7 shows five images, taken from a series of 10, showing deposition of copper from air-saturated 0.2M CuSO$_4$/1.0M H$_2$SO$_4$/1.0mM HCl/0.1mM MPSA solution. Deposits consisted of flat-topped mounds, which appeared to be intermediates between the clearly defined four-sided pyramids seen in Figure 4.3 and the rounded nodules seen in Figure 4.5. The symmetry of the underlying metal surface was visible, but distinct pyramids did not appear. The majority of the mounds were formed during the first 20 seconds of deposition. After that, the existing mounds grew laterally and vertically as more material was deposited and no new growth centers emerged. Eventually the large mounds merged partly, leaving deep recess between them. The growth behavior observed here can be attributed to the combined effect of the Cl$^-$ and MPSA in the solution.

4.2.8 Deaerated 0.2M CuSO$_4$/1.0M H$_2$SO$_4$/1.0mM HCl/0.1mM MPSA

Figure 4.8 shows a series of AFM images that illustrates the growth of copper deposit from deaerated 0.2M CuSO$_4$/1.0M H$_2$SO$_4$/1.0mM HCl/0.1mM MPSA solution. The deposit morphology was consistent with that obtained in the same solution when saturated with air. Large, three-dimensional, flat-topped mounds formed at the advanced stages of copper electrodeposition. No further growth occurred in the recess area between the large mounds as deposition proceeded. The morphological consistence between Figure 4.7 and Figure 4.8 indicates that dissolved oxygen in the plating solution did not affect the deposit morphology markedly under the conditions of this study.

(a)

(b)

(c)

(d)

(e)
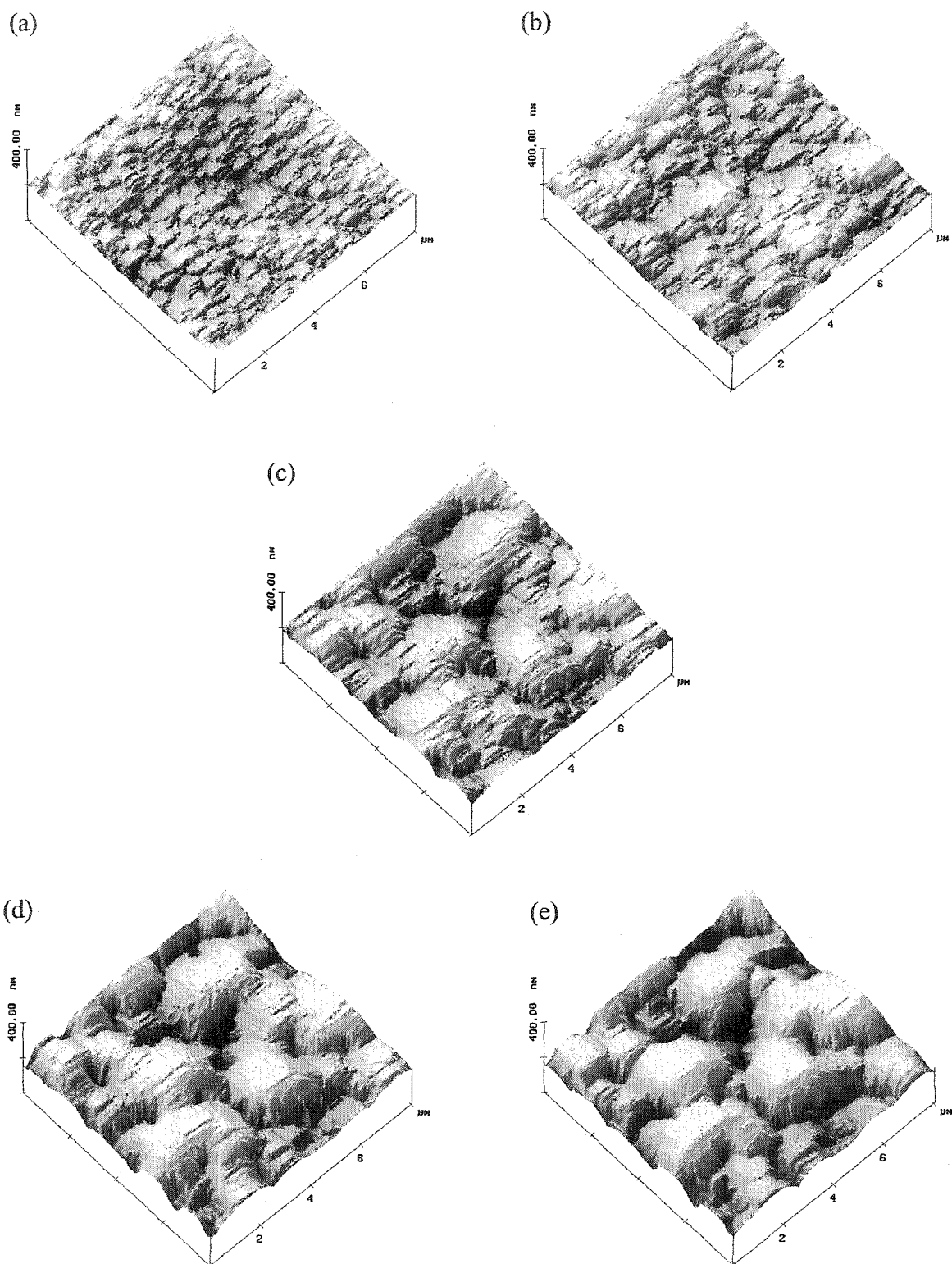
Figure 4.7 AFM images of Cu electrodeposition on single crystal copper from air-saturated 0.2M $CuSO_4$/1.0M H_2SO_4/1.0mM HCl/0.1mM MPSA solution at current density of 30 mA/cm^2 for deposition time of (a) 10s, (b) 20s, (c) 30s, (d) 40s, (e) 50s.
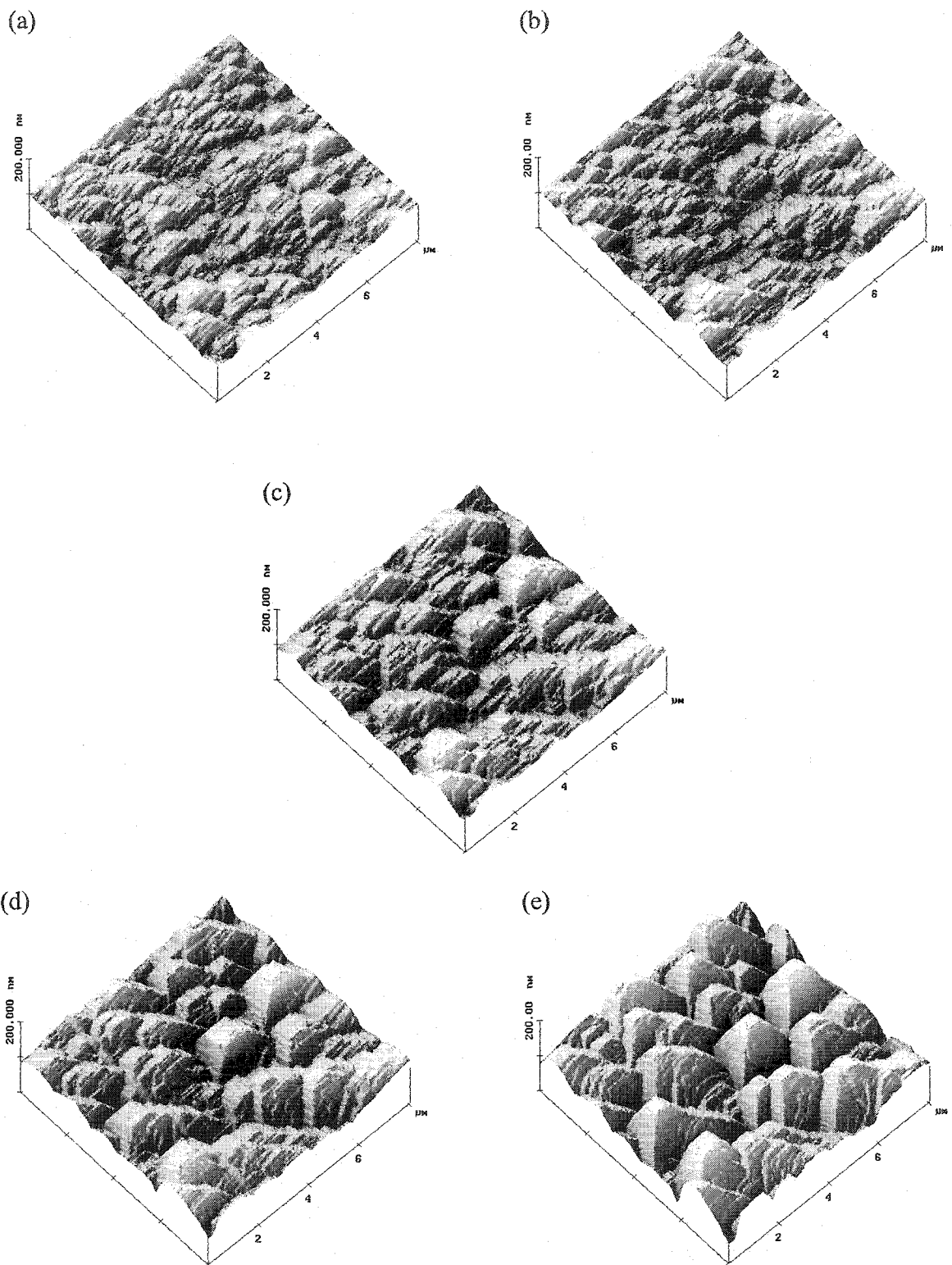
54
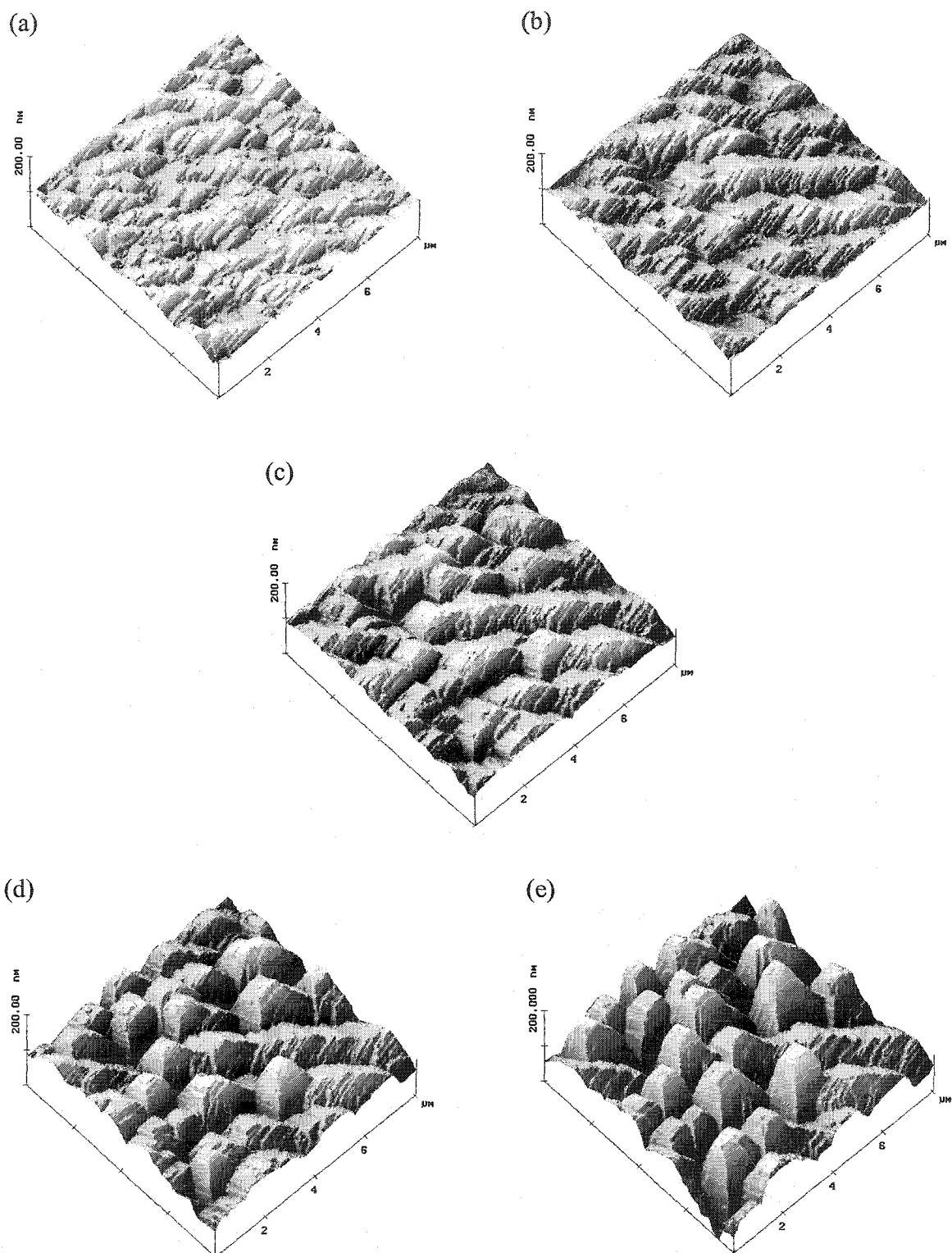
(a)

(b)

(c)

(d)

(e)
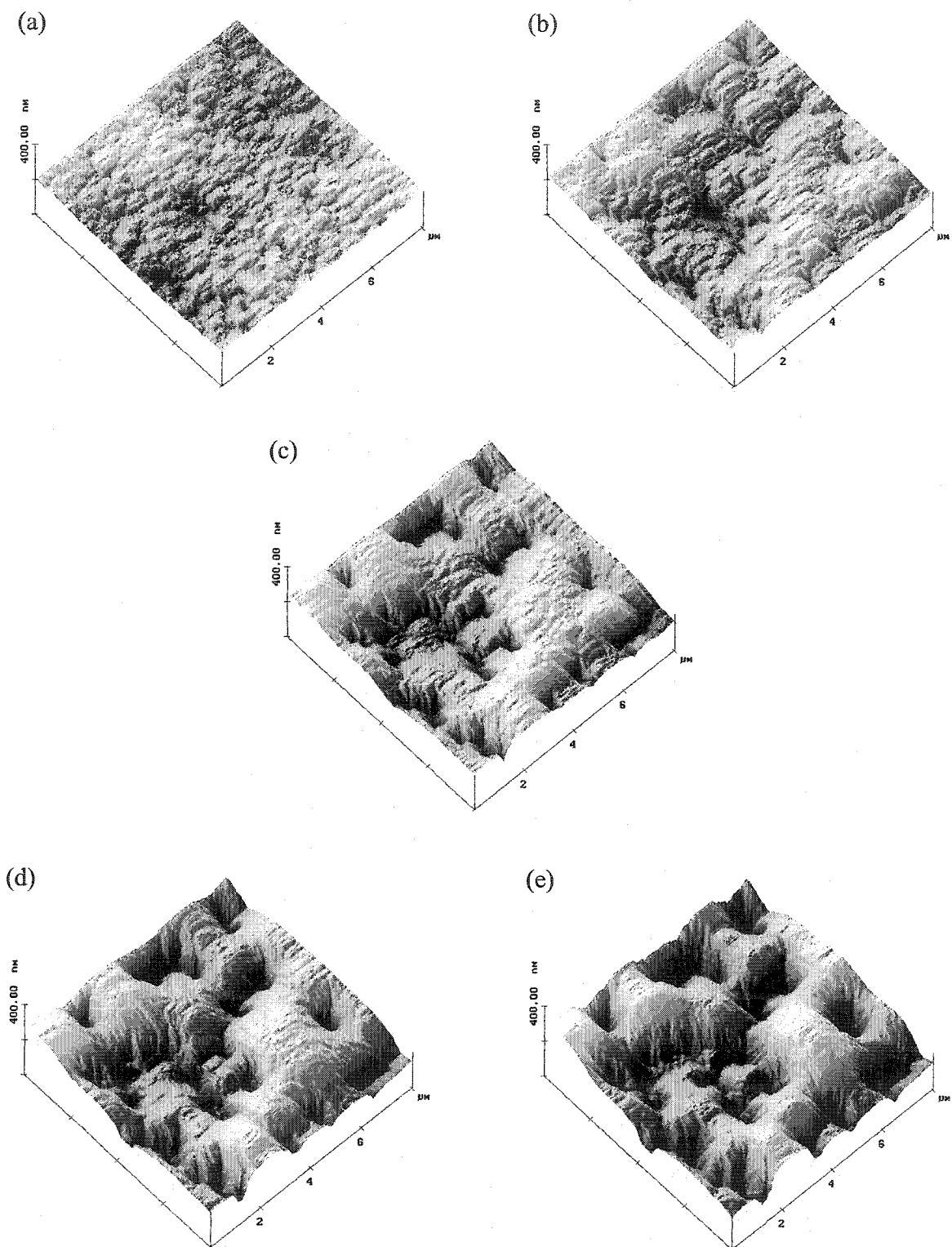
Figure 4.8 AFM images of Cu electrodeposition on single crystal copper from deaerated 0.2M $CuSO_4$/1.0M H_2SO_4/1.0mM HCl/0.1mM MPSA solution at current density of 30 mA/cm^2 for deposition time of (a) 10s, (b) 20s, (c) 30s, (d) 40s, (e) 50s.

55

4.3 Discussion

4.3.1 Scaling Analysis

The growth of surfaces is inherently a complex phenomenon and discussion of growth mechanisms so far has been primarily qualitative in nature. However, in addition to insights obtained by inspecting AFM images directly, surface growth can be analyzed quantitatively using the scaling methodology.[75][77] Scaling analysis of the surface roughness is based on the assumption that surfaces become rougher as they grow and correlates the roughness evolution with the mechanism by which surface grows. This type of analysis, which has also been applied to surface growth from vapor deposition, considers the surface growth as the result of competition between roughening processes such as stochastic arrival of species from a vapor or solution phase and lateral smoothing processes such as surface diffusion. Recent theoretical and experimental developments have shown that the molecular scale phenomena involved in surface growth leave a definite signature in the morphology of the surface.[75]

Scaling analysis applies strictly to surfaces that satisfy the condition of self-affinity.[7] A surface is characterized as self-affine when it exhibits self-resemblance over a range of scales; that is, the contour of a self-affine surface has the same appearance when viewed at various degrees of magnification. The concept of self-affinity is described mathematically by the following relation:

$$H(r) = \kappa' H(\kappa r) \qquad (4.1)$$

where H(r) is the height at point r on the surface. If a surface, defined by $\kappa' H(\kappa r)$ is indistinguishable from one defined by H(r), then H is self-affine. Self-affinity is a more

general case of the scaling phenomenon of self-similarity (H(r) = κH(κr)), which is used to describe a fractal surface. Schmidt et al.[6] and Iwasaki et al.[32] found that copper surfaces formed by electrodeposition were self-affine.

To describe the surface growth quantitatively, the function of surface width $w(L, t)$ is introduced to characterize the roughness of the surface. The surface width $w(L, t)$, also known as the root mean square (rms) height of the surface, is the standard deviation of the surface height over length scale L consisting of N data points at growth time t and is defined by [77]

$$w(L,t) = \sqrt{\frac{1}{N}\sum_{i=1}^{N}[h_i(t) - \bar{h}(t)]^2} \qquad (4.2)$$

where $h_i(t)$ is the height of the surface at position i at time t and $\bar{h}(t)$ is the mean height of the surface over length scale L. The value of surface width $w(L, t)$ depends on the extent of the examined surface. With the increase of scale length used to measure $w(L, t)$, the value of $w(L, t)$ also increases up to a maximum magnitude w_{max}, which is characteristic of the system. It is the description and characterization of the scaling behavior of $w(L, t)$ that has developed into a powerful theoretical description of non-equilibrium growth processes.

Family and Vicsek[7] showed that self-affine width $w(L, t)$ can be expressed in the form

$$w(L,t) = L^{\alpha} f(\frac{t}{L^{\alpha/\beta}}) \qquad (4.3)$$

57

where two parameters α and β are the scaling and growth exponents respectively, also referred to as static and dynamic exponents. Self-affine surfaces are characterized by values of α between 0 and 1 whereas self-similar surfaces have $\alpha = 1$. Furthermore, in Eq. (4.3), $f(t/L^{\alpha/\beta})$ has the following properties: $f(t/L^{\alpha/\beta}) = $ constant for $t/L^{\alpha/\beta} \rightarrow \infty$, and $f(t/L^{\alpha/\beta}) = (t/L^{\alpha/\beta})^{\beta}$ for $t/L^{\alpha/\beta} \rightarrow 0$. Therefore, Eq. (4.3) comprises two limiting cases. At long time and short length scales, $t/L^{\alpha/\beta} \rightarrow \infty$, and

$$w(L) \propto L^{\alpha} \tag{4.4}$$

At short times and long length scales, $t/L^{\alpha/\beta} \rightarrow 0$, and

$$w(t) \propto t^{\beta} \tag{4.5}$$

The crossover between these two types of behavior occurs at $L = L_c$, which is referred as the critical length. The critical length increases with time.

The values of α and β can be derived from log-log plots of Eqs. (4.4) and (4.5), respectively. The surface width $\log(w)$ increases with the length scale $\log(L)$ of the area over which it is measured, but if L exceeds a critical value L_c the surface width has a constant value w_{max} that is independent of L. By plotting the surface width w as a function of L at various deposition times, it is possible to evaluate the scaling exponent α from the initial slope of the $\log(w)$ vs. $\log(L)$. The constant surface width w_{max} increases with deposition time t, and the slope of the $\log(w_{max})$ vs. $\log(t)$ line is equal to the growth exponent β. Reliable data for the two exponents can be derived from this procedure when scaling is made over wide length and time ranges. Comparison of measured scaling and

58

growth exponents with those predicted by theoretical models provides insight into the mechanisms operative in real surface growth.

Several investigators have applied the scaling analysis to copper electrodeposits, producing scaling exponents of 0 to 1 and growth exponents of up to 0.5.[6][31][32][79] More recently, Huo and Schwarzacher used an anomalous scaling relation, which had the form,[80]

$$w(L,t) = L^{\alpha} t^{\beta_{loc}} f(\frac{t}{L^{\alpha/\beta}}) \tag{4.6}$$

where the parameter β_{loc} is a 'local' growth exponent. This differs from normal scaling because surface width w is no longer independent of t for small L, but rather shows a power law dependent on L and t. As before, w shows a power law dependence on t for large L, this time scaling as $t^{\beta+\beta_{loc}}$. Huo and Schwarzacher reported a scaling exponent α of about 0.8 and a growth exponent β of about 0.4 independent of deposition rate. The local growth exponent β_{loc} varied from 0 to 0.44 and increased with increasing current density.

In this study, scaling analysis was employed to analyze the AFM images for the deposits obtained with all eight experimental conditions. Analysis was performed using a specifically developed code. The code calculated the surface width as a function of the image area size. For each ASCII data file exported from 8x8 μm AFM images, which consisted of 512x512 points, the surface was divided into squares of 8x8 points each and surface width was measured on each square. A total of 4096 resulting surface widths at this smallest surface area were calculated and a representative surface width value for the area was then obtained by averaging the 4096 values. The measured sample size was then

59

increased and the surface width was recalculated for this bigger sample size. The same procedure was followed until the surface width of the entire area (8x8 μm) was measured. The results were reported surface width vs. scaling length, and w was plotted against L.

Figure 4.9 shows the experimental relationship between surface width $w(L, t)$ and sample area L for copper deposits formed from an additive-free solution under air-saturated condition. Each set of points, which is obtained from one of AFM images shown in Figure 4.1, corresponds to a different deposition time t. The range of t that can be studied is limited. When t is too small, $w(L, t)$ is dominated by the substrate. When t is too large, the surface becomes too rough to measure reliably by AFM, and tip artifacts appear in the images. It can be seen from Figure 4.9 that at low L values, there is a linear dependence between $\log(w)$ and $\log(L)$, and the surface width $w(t, L)$ becomes constant at large L. The trend is observed in all eight studied conditions. According to Eq. (4.4), the scaling exponent α is equal to the slope of the linear regime of the log-log plots. In this case, α is determined to be 0.72.

A plot of the constant surface width w_{max} at different deposition times is used to determine the growth exponent β. Figure 4.10 is a log-log plot of w_{max} vs. t for copper deposits formed from an additive-free solution under air-saturated condition. It may be seen that the data does exhibit a simple linear dependence as predicted by Eq. (4.5). The solid line is the least-square fit to the data. From Eq. (4.5), β is equal to the slope of the line. In Figure 4.10, β is determined to be 0.24 with $R^2 = 0.979$.

60
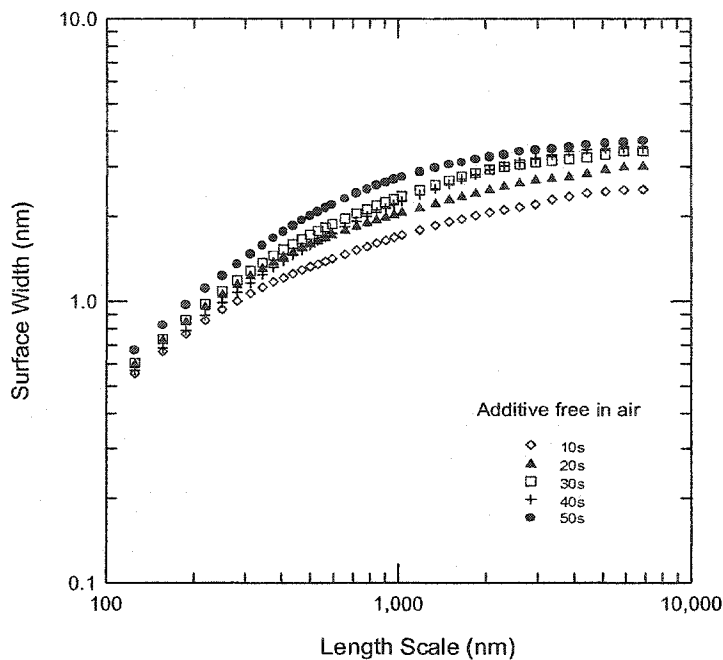
Figure 4.9 Plots of surface width vs. length scale for deposits obtained from air-saturated 0.2M $CuSO_4$/1.0M H_2SO_4 solution at different deposition times.
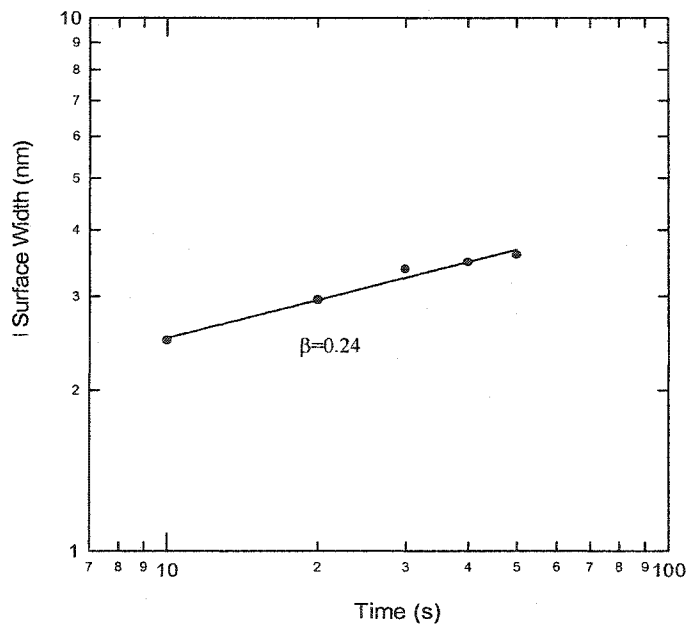
Figure 4.10 Plot of maximum surface width vs. deposition time for copper deposited from air-saturated 0.2M $CuSO_4$/1.0M H_2SO_4 solution.

61
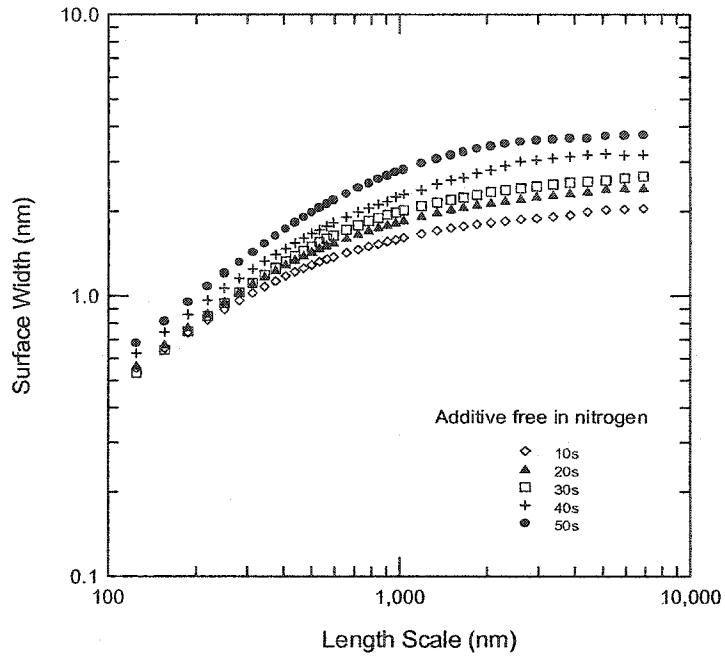
Figure 4.11 Plots of surface width vs. length scale for deposits obtained from deaerated 0.2M CuSO$_4$/1.0M H$_2$SO$_4$ solution at different deposition times.
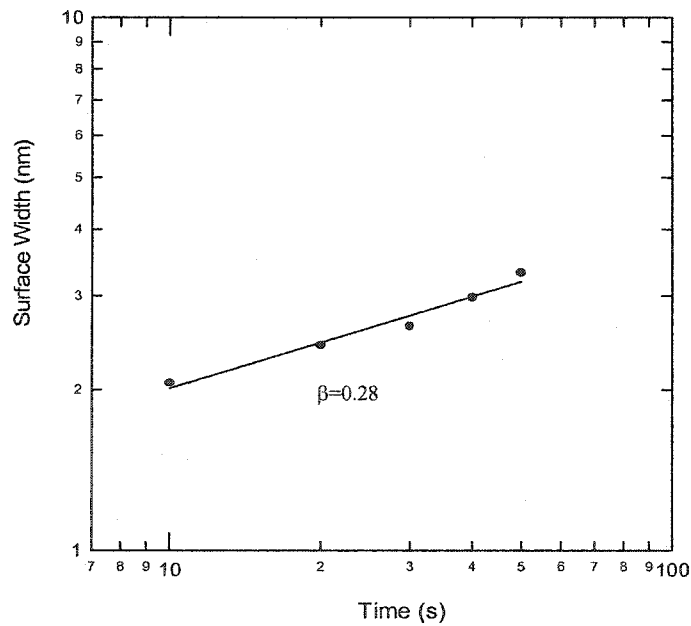
Figure 4.12 Plot of maximum surface width vs. deposition time for copper deposited from deaerated 0.2M CuSO$_4$/1.0M H$_2$SO$_4$ solution.

62
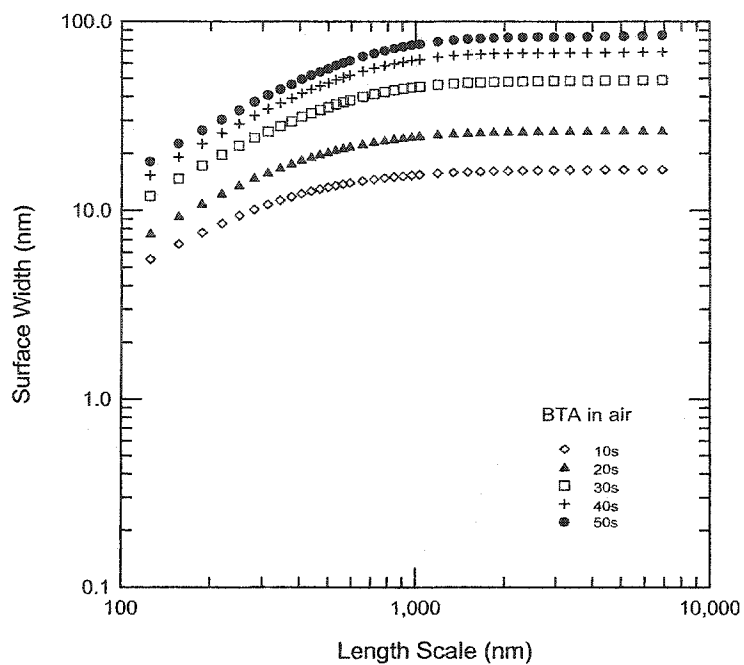
Figure 4.13 Plots of surface width vs. length scale for deposits obtained from air-saturated 0.2M CuSO$_4$/1.0M H$_2$SO$_4$/1.0mM HCl/0.1mM BTA solution at different deposition times.
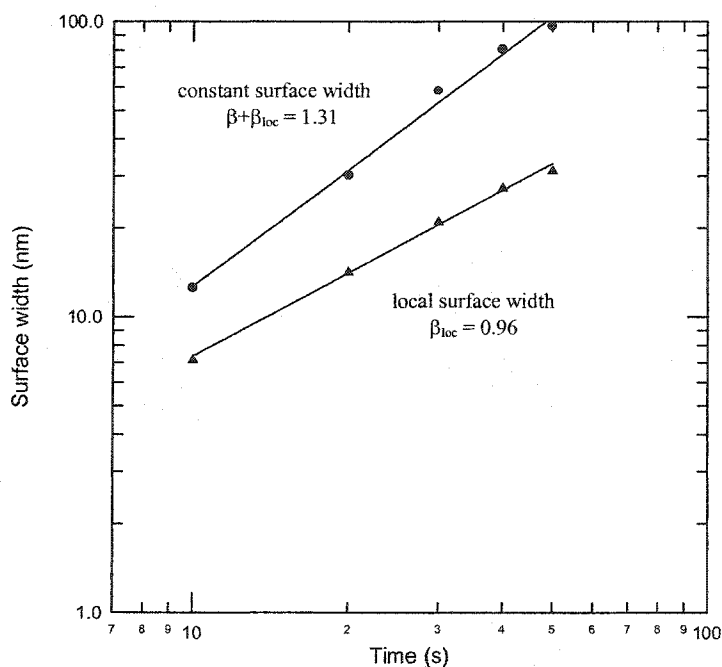
Figure 4.14 Plot of local surface width [$w(t, L)$ for $L = 200$ nm] and maximum surface width vs. deposition time for copper deposited from air-saturated 0.2M CuSO$_4$/1.0M H$_2$SO$_4$/1.0 mM HCl/0.1mM BTA solution.

63
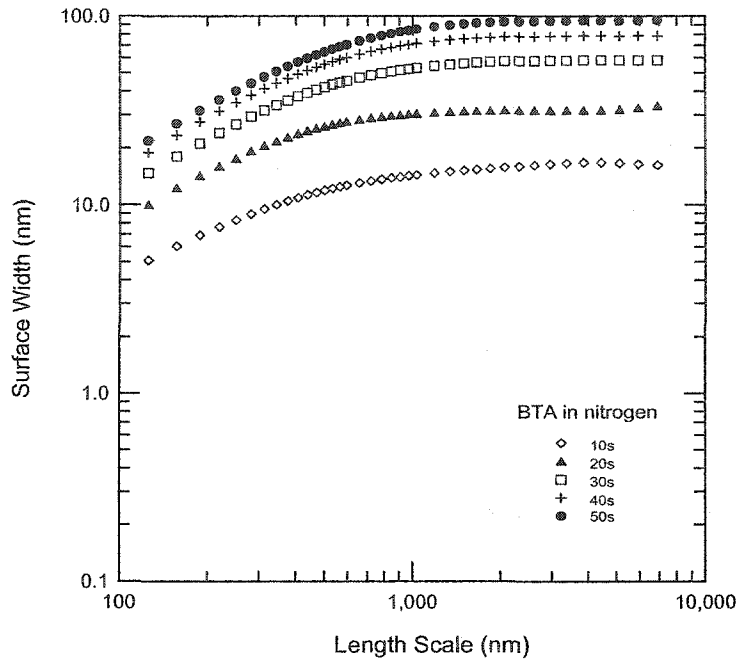
Figure 4.15 Plots of surface width vs. length scale for deposits obtained from deaerated 0.2M CuSO₄/1.0M H₂SO₄/1.0mM HCl/0.1mM BTA solution at different deposition times.
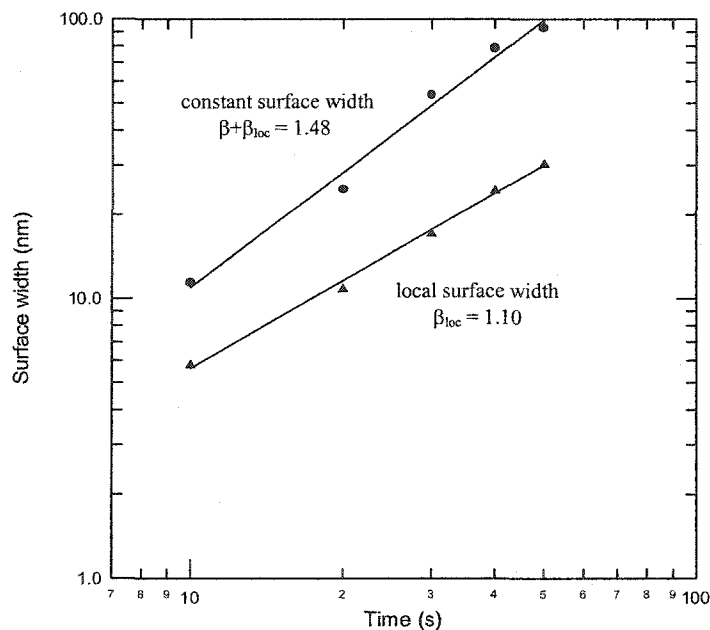
Figure 4.16 Plot of local surface width [$w(t, L)$ for $L = 200$ nm] and maximum surface width vs. deposition time for copper deposited from deaerated 0.2M CuSO₄/1.0M H₂SO₄ /1.0mM HCl/0.1mM BTA solution.

64
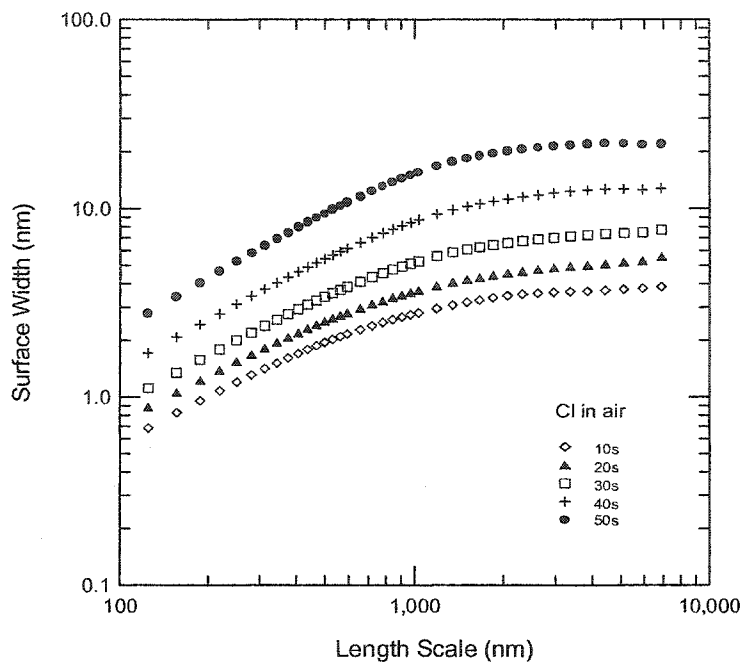
Figure 4.17 Plots of surface width vs. length scale for deposits obtained from air-saturated 0.2M CuSO$_4$/1.0M H$_2$SO$_4$/1.0mM HCl solution at different deposition times.
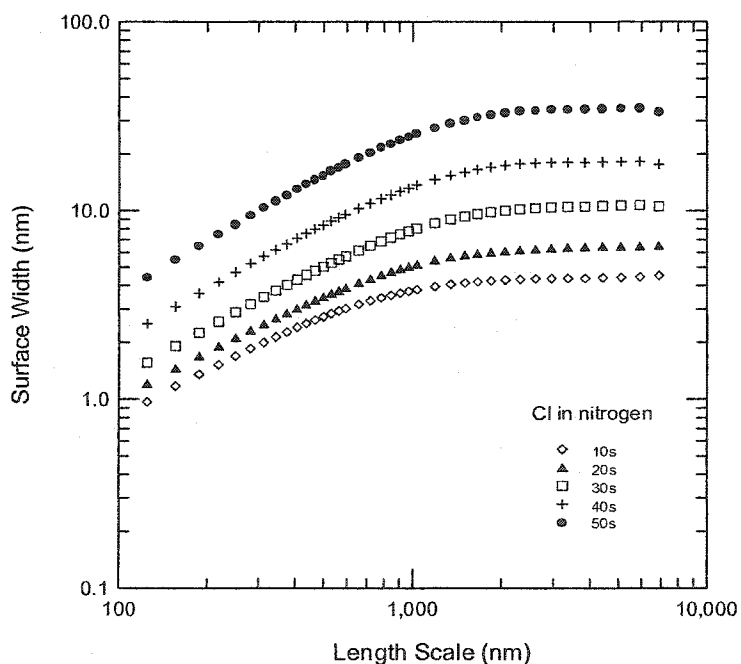
Figure 4.18 Plots of surface width vs. length scale for deposits obtained from deaerated 0.2M CuSO$_4$/1.0M H$_2$SO$_4$/1.0mM HCl solution at different deposition times.

65
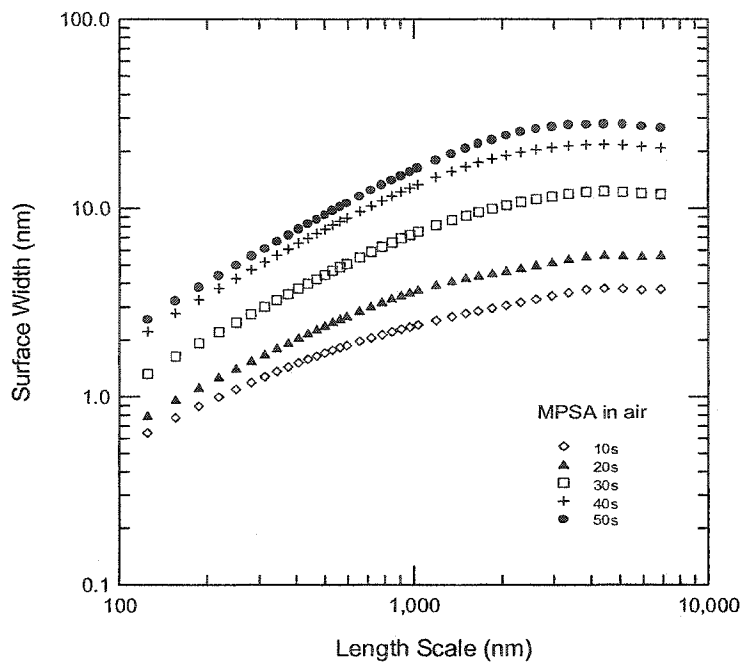
Figure 4.19 Plots of surface width vs. length scale for deposits obtained from air-saturated 0.2M CuSO$_4$/1.0M H$_2$SO$_4$/1.0mM HCl/0.1mM MPSA solution at different deposition times.
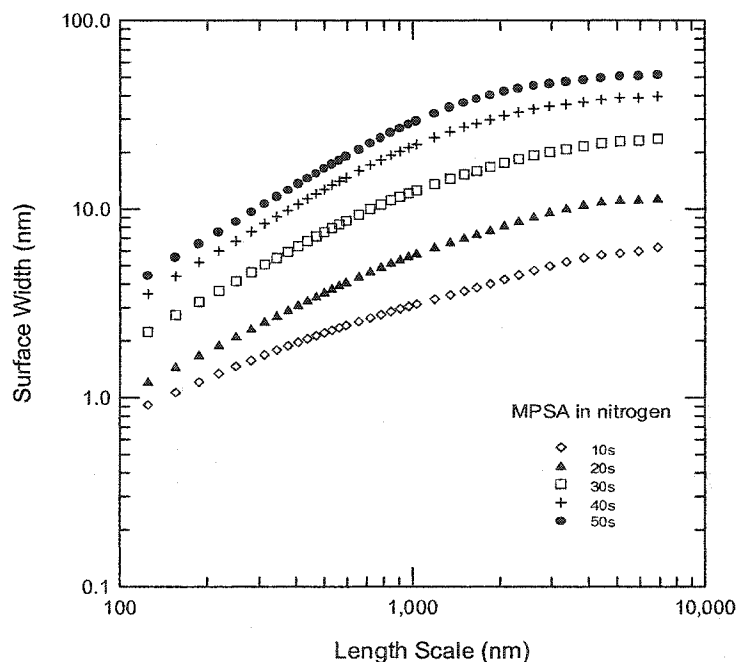
Figure 4.20 Plots of surface width vs. length scale for deposits obtained from deaerated 0.2M CuSO$_4$/1.0M H$_2$SO$_4$/1.0mM HCl/0.1mM MPSA solution at different deposition times.

66

The same procedure was followed for the scaling analysis of surfaces grown from additive-free solution under deaerated condition. Figure 4.11 illustrates the surface width w as a function of the length scale L for the surfaces shown in Figure 4.2. Again the dependence of w on L is linear at the small length scale, with a slope of $\alpha = 0.70$ but as the length scale increases the surface width reaches a constant value w_{max}. Figure 4.12 shows the maximum surface width dependence on deposition time for surfaces grown from additive-free solution under deaerated condition. The growth exponent β is equal to the slope of w_{max} with deposition time and was found to be equal to 0.28.

Figure 4.13 shows surface width $w(L, t)$ data for a series of films electrodeposited on Cu(100) surface from BTA+Cl⁻ solution under air-saturated condition. For each deposition time, w is approximately constant for large scale length L and $\log(w)$ shows a linear dependence on $\log(L)$ for small L, with a scaling exponent α of 0.86. For small L, $w(L, t)$ increases with deposition time, which means that the kinetic roughening cannot be described by the normal scaling relation Eq. (4.3). It can, however, be described by the anomalous scaling relation Eq. (4.6). As Figure (4.14) shows, $\log(w)$ varies linearly with $\log(t)$ in both the small L and large L regions. Figure (4.14) shows local surface width $w(L, t)$ for $L = 200$nm and maximum surface width w_{max} for $L > L_c$ as calculated from the data of Figure (4.13). The solid lines, which are the least-square fit to local and maximum surface width data, have slopes $\beta_{loc} = 0.96$ and $\beta + \beta_{loc} = 1.31$, respectively.

Surfaces of copper deposits grown from BTA+Cl⁻ solution under deaerated condition also demonstrated anomalous scaling as shown in Figures (4.15) and (4.16). The same analysis gives scaling exponents of $\alpha = 0.89$, $\beta_{loc} = 1.10$, and $\beta + \beta_{loc} = 1.48$ for this deposition condition.

Figures 4.17 to 4.20 show the scaling analysis of copper deposits obtained from Cl⁻ solutions and MPSA+Cl⁻ Solutions under air-saturated and deaerated conditions, respectively. These figures show that kinetic roughening during copper electrodeposition in the presence of additives obeys the anomalous scaling law, as described by Eq. (4.6).

Taken together, the results of scaling analysis of deposits grown from additive-free and additive-containing solutions show that at small length scales the surface width increases linearly with scaling length L. In additive-free solutions, surface width is independent of deposition time. In Cl⁻ and organic additives containing solutions, surface width continues to increases with deposition time. The fact that in all cases the scaling exponent α is between 0 and 1 serves as evidence of deposit self-affinity[75]. Information on the mechanism of surface growth can be obtained by comparison of the scaling exponents obtained here with values reported in the literature.

A summary of the scaling parameters for the different deposition systems is given in Table 4.1. These scaling exponents represent the average values obtained from all three experiments performed for each deposition system defined by the solution and the purge gas. Among the four solutions, the deposits obtained from additive-free solutions give the smallest α, while the deposits obtained from solutions containing MPSA+Cl⁻ yield the largest α. The presence of dissolved oxygen does not markedly affect values of α for either solution. The values of β fall between 0.16 and 0.38, and decrease when dissolved oxygen is present for each solution studied here. β_{loc} varies over a wide range. For the additive free solutions, β_{loc} equals 0, and for the additive containing solutions, β_{loc} is close to 1.

Table 4.1 Experimentally determined scaling exponents for copper electrodeposition.

System	α	β	β_{loc}
Additive-free with air	0.72	0.24	0
Additive-free with N_2	0.70	0.28	0
Cl^- with air	0.83	0.22	0.83
Cl^- with N_2	0.85	0.25	0.90
BTA+Cl^- with air	0.86	0.35	0.96
BTA+Cl^- with N_2	0.89	0.38	1.10
MPSA+Cl^- with air	0.92	0.16	0.96
MPSA+Cl^- with N_2	0.94	0.19	0.86

The maximum surface width in Cl^-+BTA solutions after 50 seconds was 100 nanometers, about twice the surface width of the deposits formed in Cl^-+MPSA solutions, about three times the surface width of the deposits formed in Cl^- solutions, and more than ten times the surface width of the deposits formed in additive-free solutions. In Cl^-+BTA solutions, the surface width jumps about ten-fold from the substrate to the first deposit image, which represents the deposit formed at 10 seconds. This is probably the result of nuclei formation across the entire substrate surface from the very initial stage of electrodeposition. In all four solutions, deposition after pre-equilibration of the solution under nitrogen results in a larger surface width than deposition with exposure of the solution to air.

From the scaling plots shown in Figure 4.13 to 4.20, the critical scaling length L_c was 700 nm for Cl^-+BTA solutions, 1000 nm for Cl^- solutions and 3000 nm for Cl^-+MPSA solutions. These scales correlate reasonably well with the size of dominant features visible in the AFM images (see Figure 4.3 to 4.8).

4.3.2 Scaling Analysis and Kinetic-Roughening Mechanism

A number of models have been introduced to describe the mechanisms involved in surface growth and predict the values of scaling exponents.[75][77] By comparing the experimentally found scaling exponents with those derived from different models, more understanding in the growth mechanism can be obtained.

The simplest growth model, called random deposition (RD), describes attachment of particles at random positions on the surface, resulting in deposition without lateral growth. The RD model predicts $\alpha = 0$ and $\beta = 0.5$. A more complicated growth model is the balllistic deposition (BD) model, which is similar to the RD model except lateral growth is allowed.[81] In BD, particles impinge on the surface along straight lines at an angle to the surface normal. They are capable of sticking to the edges of surface protrusions, leading to lateral growth. For a one-dimensional surface, $\alpha \sim 0.5$ and $\beta \sim 1/3$ were estimated.

Additionally, several modified-RD and modified-BD models have been proposed. Family investigated the effect of incorporating surface diffusion in the RD model on the scaling properties of the surface.[82] Surface diffusion implies a correlation between neighboring columns, resulting in a smoother surface. For d = 2, $\alpha \approx 0.5$ and $\beta \approx 0.25$ were estimated. The BD model with surface relaxation was also studied.[83] Introduction of surface relaxation leads to $\alpha = 0.36$ and $\beta = 0.22$ for $d = 3$.

In addition to these discrete growth models which consider microscopic processes, various continuum growth models have been developed, which describe surface growth as the result of competition between stochastic roughening, caused by random arrival of material at the surface and various smoothing mechanisms, such as surface diffusion.[7][75]

70

The simplest continuum growth model of the evolution of surface morphology by deposition is stochastic roughening. This model assumes random arrival of material to the surface and no mass transport along the surface, i.e. no smoothing processes.[84] As a result the surface height exhibits a Poisson distribution with no correlation between the height of the any two sites regardless of their distance. A continuum equation that models this stochastic roughening is

$$\frac{\partial h(\mathbf{r},t)}{\partial t} = F + \eta(\mathbf{r},t) \tag{4.6}$$

where $h(r, t)$ is the surface height at any position r on the surface. F is the local time-average growth rate set by the current density. $\eta(r, t)$ represents spatially uncorrelated, randomly fluctuating deposition rate. Surfaces grown by stochastic roughening exhibit scaling exponent $\alpha = 0$ and growth exponent $\beta = 0.5$.

Some terms depending on the spatial derivatives of surface height h have been introduced into Eq. (4.6). These terms have the effect of smoothing the surface and are local. Edwards and Wilkinson introduced the linear term $\nabla^2 h$ on the right hand of Eq. (4.6) to lead to the EW growth model, which has the form:[85]

$$\frac{\partial h(\mathbf{r},t)}{\partial t} = F + \nu\nabla^2 h + \eta(\mathbf{r},t) \tag{4.7}$$

The term $\nabla^2 h$ is the lowest order derivative that models the erosion of hills and the filling of valleys. ν is sometimes called a 'surface tension', for the $\nu\nabla^2 h$ term tends to smooth the interface. The EW equation can be solved exactly. Scaling exponents depend on the

dimension of the interface. In three dimensions, both α and β are zero. Growth for which $\alpha = \beta = 0$ apparently corresponds to the atomistic Frank van der Merwe model, where an initial flat surface grows without significant roughening. The EW model does not consider lateral growth and represents a class which can describe as a modified-RD model.

Kardar, Parisi and Zhang proposed an equation of motion to describe the spatial and temporal evolution of a non-equilibrium growing surface, known as the KPZ equation:[86]

$$\frac{\partial h(\mathbf{r},t)}{\partial t} = F + v\nabla^2 h + \frac{\lambda}{2}(\nabla h)^2 + \eta(\mathbf{r},t) \tag{4.8}$$

The nonlinear term $(\nabla h)^2$ is added to account for lateral growth, and v and λ are system-dependent parameters. The KPZ model applies to cases where the dominant surface relaxation mechanism is not surface diffusion. However, it takes into account smoothing processes on surface due to the erosion of protrusions and the filling of recesses as well as nonlinear effects expected in all physical systems. Numerical simulations have shown that surfaces that grow according to the KPZ model are characterized by $\alpha = 0.39$ and $\beta = 0.25$.[87] The values of the exponents are very close to those in the modified-BD models described earlier. The BD model is believed to belong to the same universality class as KPZ growth.

Wolf and Villain assumed that smoothing of growing surface may take place by surface diffusion, and presented thermodynamic arguments to show that a $-\nabla^4 h$ term would better model the process of smoothing by surface diffusion. They proposed the following WV equation to describe surface growth:[88]

72

$$\frac{\partial h(\mathbf{r},t)}{\partial t} = F - \omega \nabla^4 h + \eta(\mathbf{r},t) \tag{4.9}$$

where ω is a constant which incorporates the thermodynamic and transport parameters. The WV equation is linear and thus can be solved exactly in three-dimension to yield scaling exponents of $\alpha = 1$ and $\beta = 0.25$. The WV model is not applied to a smooth surface but rather to a surface which has substantial features.

Given the importance associated with the nonlinear term in the KPZ equation, Villian added such a term to the WV equation to yield:[89]

$$\frac{\partial h(\mathbf{r},t)}{\partial t} = F - \omega \nabla^4 h + \rho \nabla^2 (\nabla h)^2 + \eta(\mathbf{r},t) \tag{4.10}$$

where the physical interpretation of the nonlinear term is related to the growth of steps which act as sources or sink of atoms on a growing surface. This modified WV model or "WV + step flow" model leads to $\alpha = 0.67$ and $\beta = 0.2$ for $d = 3$.

Each of the models presented above represents a particular mechanism of deposit growth, which is characterized by a set of scaling and growth exponents. Comparison of experimentally derived scaling and growth exponents with the ones predicted by models such as the ones discussed above can be used to determine the processes responsible for deposit growth. Table 4.2 summarizes the predictions for the scaling and growth exponents of the various theoretical models and experimental values obtained from the present research. Notice that except for the stochastic model, all other models predict a small β, while the values of α suggested in the different models span a relatively wide range.

73

Table 4.2 Scaling exponents from theoretical models and experimental results

	α	β	Reference
Continuum Models			
Stochastic roughening	0	0.5	[75][84]
EW	0	0	[85]
KPZ	0.39	0.25	[86][87]
WV(surface diffusion)	1	0.25	[88]
WV + step flow	0.67	0.2	[89]
Experimental Results			
Additive-free with air	0.72	0.24	
Additive-free with N_2	0.70	0.28	
Cl^- with air	0.83	0.22	
Cl^- with N_2	0.85	0.25	
BTA+Cl^- with air	0.86	0.35	
BTA+Cl^- with N_2	0.89	0.38	
MPSA+Cl^- with air	0.92	0.16	
MPSA+Cl^- with N_2	0.94	0.19	

74

There were a few studies which employed scaling analysis to study copper electrodeposition in acid sulfate solution. Among prior studies, none are directly comparable to the present work because of differences in substrate, concentration of copper sulfate and additives, applied current density, and deposit thickness. Scaling analysis of the additive-free deposition of copper has been conducted. Previous studies by Mendez et al.[33] and Schmidt et al.[6] suggested that the growth followed the surface diffusion model. The scaling analysis for the additive-free deposition conducted by Iwamoto and others proposed that the nonlocal growth effect was in play.[79]

Scaling analysis has also been applied to study the effect of an additive on copper electrodeposition. Mendez and co-workers[33][90] investigated the action of thiourea, and the results showed that the growth followed the WV model at small length scales, and the EW model was operative at large length and time scales. Iwasaki and Yoshinobu[32] studied the effect of sulfonium-alkane-sulfonate compounds and proposed that the growth followed the KPZ model.

In the present study, the scaling and growth exponents experimentally derived from additive-free deposition were $\alpha = 0.72$, $\beta = 0.24$ in air-saturated solution and $\alpha = 0.70$, $\beta = 0.28$ in deaerated solution, respectively. Compared to the scaling exponents suggested by various models, the values of α and β obtained from additive-free deposition are in reasonably close agreement with those predicted by the "WV+step-flow" model. It suggests that for this case "WV+step-flow" mechanism is operative. Deposit growth is the result of competition between stochastic surface roughing and smoothing from surface diffusion and step growth. Direct evidence of a step growth mechanism was given from the AFM images of Figure 4.1 and 4.2 and is in agreement with the results of

75

scaling analysis. It is noteworthy that using electrochemical STM, electrodissolution of copper in pure sulfuric acid was found to start at steps as well.[91] In light of this, a reciprocal relationship may exist between the electrodissolution and electrodeposition processes. The reciprocal relationship was suggested in a study of copper deposition with a different additive by Iwamoto et al.[79]

For the solution containing Cl⁻, the values of α and β were found to be 0.83 and 0.22 for air-saturated condition, and 0.85 and 0.25 for deareated condition. They are similar to the additive-free system ($\alpha = 0.70\sim0.72$ and $\beta = 0.24\sim0.28$) and represent a similar surface growth mechanism in surface growth. The step growth was observed in the faces of pyramidal side in the AFM images obtained in the solution containing Cl⁻ (see Figure 4.3 and 4.4). The values for β in Cl⁻ containing solution are a little lower than those in additive free system. A little small value of β suggests that there is a weaker coupling between surface roughness and deposition time for Cl⁻ containing solution. Cl⁻ was known to accelerate the electron transfer reaction and may be the cause of the reduction in β value.

For the case of BTA+Cl⁻, the values of β (0.35 with air, 0.38 with nitrogen) are relatively large and close to the stochastic limit ($\beta = 0.5$). The relatively large β reflects the large and rapid increase in roughness from development of nodules formed across the entire surface and is suggestive of a roughening mechanism that can be described by the random roughening term of the stochastic model. Tong and Williams[75] proposed that an increase in β is due to an unknown roughening mechanism. The unknown roughening mechanism could be due to crystal growth in the deposit or electrochemical affects that

76

the continuum models were not designed to simulate. This reflects a more complex temporal and spatial scaling behavior.[89]

For the MPSA+Cl⁻ system, the values of α were found to be 0.92 with air and 0.94 with nitrogen, which are close to 1 which is the value predicted for the case where the only smoothing mechanism is that of surface diffusion. However, values of β found experimentally, 0.16 with air and 0.19 with nitrogen, are smaller than the value predicted by the surface diffusion growth model (0.25). From the growth exponents, it appears that the surface did not roughen as quickly as predicted from the model of a purely surface diffusion dominated process. The rate of roughening is even lower than that found for a process dominated by surface diffusion coupled with the lateral growth of surface steps. The lower value of β for the MPSA+Cl⁻ system suggests that none of the existing models describes sufficiently the surface growth mechanism for this case.

4.3.3 Pattern Recognition Analysis

Scaling analysis of deposit surfaces describes statistical measures of the surface roughness and represents highly averaged information. In contrast, pattern-recognition analysis provides a means of analyzing kinetic roughening processes that produce regular surface geometries with a characteristic size. It can be used to identify and analyze the shapes of individual surface features. In the present study, pattern-recognition procedures were used to identify the geometry of features of interest and to track their characteristic dimension during the course of copper electrodeposition with and without organic additives.

77

The pattern-recognition analysis proceeds through two steps.[87] The first step is to detect the local features by template matching. A suitable measure of the similarity between two images has been used in statistics for many years — the *correlation coefficient*. For an examined image a_{ij} and the template b_{ij} of equal size, the similarity between them can be evaluated quantitatively by calculation of the square of the correlation coefficient r:

$$r^2 = \frac{[\sum_{ij}(a_{ij} - \bar{a})(b_{ij} - \bar{b})]^2}{\sum_{ij}(a_{ij} - \bar{a})^2 \sum_{ij}(b_{ij} - \bar{b})^2} \qquad (4.7)$$

where $\bar{a}$ and $\bar{b}$ are the average values of a_{ij} and b_{ij}, respectively. The quantity r^2 varies between 0 and 1 and is 1 when there is a perfect match between a_{ij} and b_{ij}. As the examined image and the template become increasingly different, the value of the correlation coefficient falls towards 0.

Working out the correlation between the examined image and a number of templates can be very time-consuming if the formula given by Eq. (4.7) is used. In practice it is usual to normalize the average height of all the images that are being processed making it possible to use the simpler equation:

$$r^2 = \frac{(\sum_{ij} a_{ij} b_{ij})^2}{\sum_{ij} a_{ij}^2 \sum_{ij} b_{ij}^2} \qquad (4.8)$$

If the examined image and the template are normalized so that:

78

$$\sum_{ij} a_{ij}^2 = \sum_{ij} b_{ij}^2 = 1 \qquad\qquad (4.9)$$

then the measure of similarity becomes:

$$r^2 = (\sum_{ij} a_{ij} b_{ij})^2 \qquad\qquad (4.10)$$

This is a much simpler quantity to calculate and, as long as the template and the examined image are normalized, it still varies between 0, corresponding to no similarity between the template and the image, and 1, corresponding to a perfect match between the template and the image. Information on the vertical scale is lost, but it can be recovered in a subsequent step.

The template matching can provide a measure of similarity between two images, but as it stands it does not provide a method of local feature detection. That is, template matching can be used to classify an image into a given prototype, but cannot be used to detect all the occurrences of the pattern within the image. The reason for this is that template matching is sensitive to a shift in position. The solution to this problem is to compute the similarity of the image with a template shifted by every possible amount. If the image is identical to the template apart from a shift, then the similarity will be 1 for some position of the template.

This idea of working out the similarity of the image with a template shifted into every possible position is known as computing the convolution of the template with the image. The convolution of a template a_{ij} and the surface height h_{nm} where the template is smaller than the full image is defined by:

79

$$c_{nm} = \sum_{ij} a_{ij} h_{i-n,j-m} \qquad (4.11)$$

The convolution c_{nm} is a correlation coefficient based on the template and an area of the surface. Local maxima in c_{nm} indicate the presence of local features similar to the template, and the magnitude of a local maximum is a measure of the degree of similarity. Thus, to detect a local feature, all we need to do is to convolve the image with a template that is a prototype of the feature that we are looking for, and then pick out positions in the result which exceed a threshold value of similarity.

For a local feature, the template will usually be very much smaller than the image, and this gives rise to the notion of feature masks. Figure 4.21 illustrates the convolution with a 3x3 mask. Each element of the convolution c_{nm} is obtained by placing the top left-hand corner of the mask over a_{nm} and working out the sum of the products of corresponding elements.

80

Result at a_{00} = multiply and sum

$= m_{00}a_{00} + m_{01}a_{01} + m_{02}a_{02} + m_{10}a_{10}$

$+ m_{11}a_{11} + m_{12}a_{12} + m_{20}a_{20} + m_{21}a_{21} + m_{22}a_{22}$

Window positioned at a_{00}   **Image A**

3x3 Mask

m_{00}	m_{01}	m_{02}
m_{10}	m_{11}	m_{12}
m_{20}	m_{21}	m_{22}

Window positioned at a_{43}
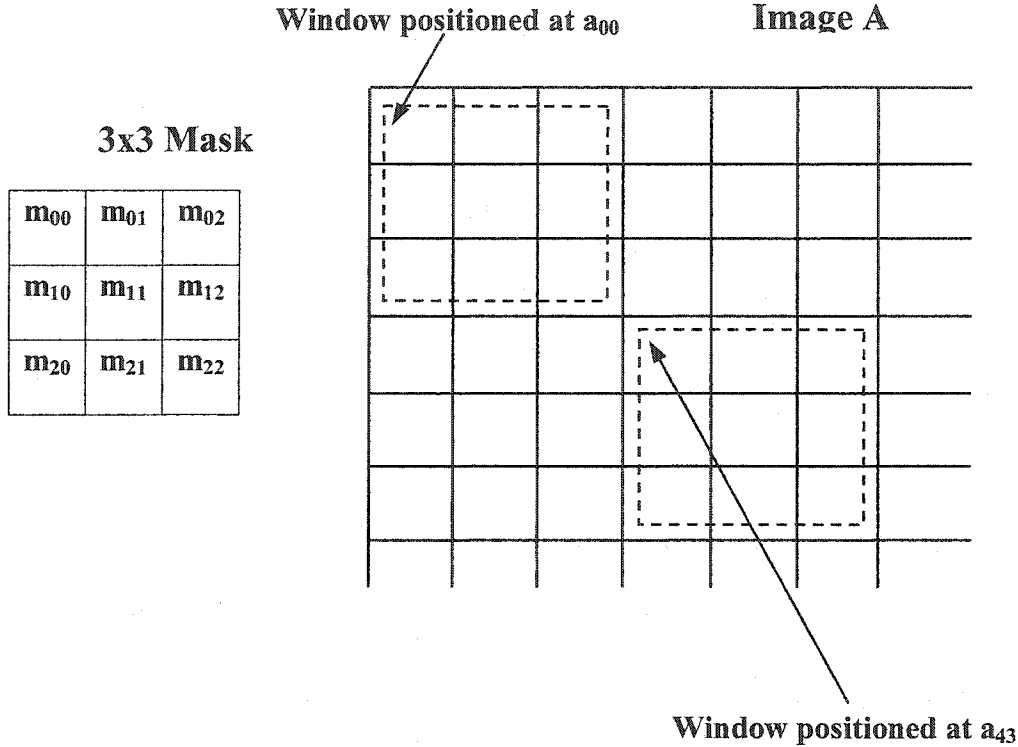
Result at a_{43} = multiply and sum

$= M_{00}a_{43} + m_{01}a_{44} + m_{02}a_{45} + m_{10}a_{53}$

$+ m_{11}a_{54} + m_{12}a_{55} + m_{20}a_{63} + m_{21}a_{64} + m_{22}a_{65}$

Figure 4.21 Schematic of convolution with a 3x3 mask.

The second step in the pattern-recognition procedure is to optimize the match between the template and surface feature at points where convolution c_{nm} is large. Because the convolution involves a normalization step, it contains no information about the height to length aspect ratio of the features of interest. In the optimization step, both the template and surface region are left un-normalized. The aspect ratio of the template is

81

then varied to find the optimum fit to the surface feature. For example, a template-matching procedure may identify a pyramid on the surface. The aspect ratio of the feature of interest is then determined by varying the aspect ratio of the template pyramid to minimize the root-mean-square deviation σ between the template and surface feature.

$$\sigma = \frac{1}{N}\sqrt{\sum_{ij}(a_{ij}-h_{ij})^2} \qquad (4.12)$$

In this study, the two steps of pattern-recognition procedures described above were performed for the deposits formed in the chloride, BTA, and MPSA solution using two developed FORTRAN programs, respectively. The templates used were square pyramid, cone, and hemisphere.

Table 4.3 shows the average slopes of square pyramid and correlation coefficients of the pyramid, cone and hemisphere templates with deposits formed in the air-saturated Cl⁻ solution at different deposition time. Results of pattern recognition analysis from two deposition experiments are included in Table 4.3. The two sets of data show good consistency. Table 4.4 shows the results of pattern recognition analysis with deposits formed in the deaerated Cl⁻ solution. From Table 4.3 and 4.4, it is clear that in the chloride solution, the square pyramid template provides the best fit, with a correlation coefficient over 90%. The other templates correlate to a lesser extent, with coefficients of 70 to 80%. The slope of the pyramid sides is given by the ratio of height to half the base width of the square pyramid template. Figure 4.22 shows the change of the slope with the deposition time. The slope increases monotonically, with no tendency to a steady or

selected value. The increase of slope in air-saturated solution is more dramatic than that in deaerated solution.

Table 4.5 and 4.6 show correlations of the pyramid, cone and hemisphere templates with deposits formed in the air-saturated and deaerated Cl⁻+BTA solution, respectively. In this solution, the hemisphere template provides the best fit, with correlation coefficients above 90%. The other templates correlate to a lesser degree, with coefficients of 70 to 80%. An aspect ratio is defined by the ratio of height to base-radius of the hemisphere. Figure 4.23 is a plot of aspect ratio versus deposition time. The aspect ratio increases linearly with deposition time in both air-saturated and deaerated Cl⁻+BTA solution.

The correlation of the pyramid, cone and hemisphere templates with deposits formed in the air-saturated and deaerated Cl⁻+MPSA solution are shown in Table 4.7 and 4.8. None of the three templates provided a satisfactory fit to the surface grown in Cl⁻+MPSA solution, and no further analysis was performed for these images. The result of this quantitative analysis is in agreement with direct observation of the AFM images. (See Figure 4.7 and 4.8)

Table 4.3 Correlation of the pyramid, cone and hemisphere templates with deposits formed in air-saturated Cl⁻ solution for two deposition experiments.

	Deposition time (s)	Slope of pyramid	Pyramid corr. coeff.	Cone corr. coeff.	Hemisphere corr. coeff.
#1	10	0.0193 ±0.0029	0.932	0.822	0.803
	20	0.0205 ±0.0036	0.924	0.831	0.805
	30	0.0252 ±0.0039	0.916	0.817	0.801
	40	0.0322 ±0.0078	0.922	0.824	0.795
	50	0.0637 ±0.0160	0.944	0.814	0.774
#2	10	0.0218 ±0.0022	0.938	0.837	0.816
	20	0.0245 ±0.0042	0.924	0.810	0.800
	30	0.0280 ±0.0065	0.922	0.818	0.804
	40	0.0440 ±0.0076	0.913	0.829	0.816
	50	0.0596 ±0.0049	0.912	0.821	0.811

Table 4.4 Correlation of the pyramid, cone and hemisphere templates with deposits formed in deaerated Cl⁻ solution for two deposition experiments.

	Deposition time (s)	Slope of pyramid	Pyramid corr. coeff.	Cone corr. coeff.	Hemisphere corr. coeff.
#1	10	0.0223 ±0.0046	0.925	0.818	0.803
	20	0.0264 ±0.0041	0.935	0.823	0.793
	30	0.0346 ±0.0043	0.926	0.824	0.809
	40	0.0597 ±0.0151	0.939	0.822	0.800
	50	0.1119 ±0.0280	0.943	0.801	0.784
#2	10	0.0245 ±0.0044	0.941	0.787	0.791
	20	0.0282 ±0.0049	0.914	0.829	0.822
	30	0.0353 ±0.0047	0.914	0.829	0.822
	40	0.0593 ±0.0151	0.915	0.828	0.824
	50	0.1119 ±0.0244	0.931	0.815	0.802
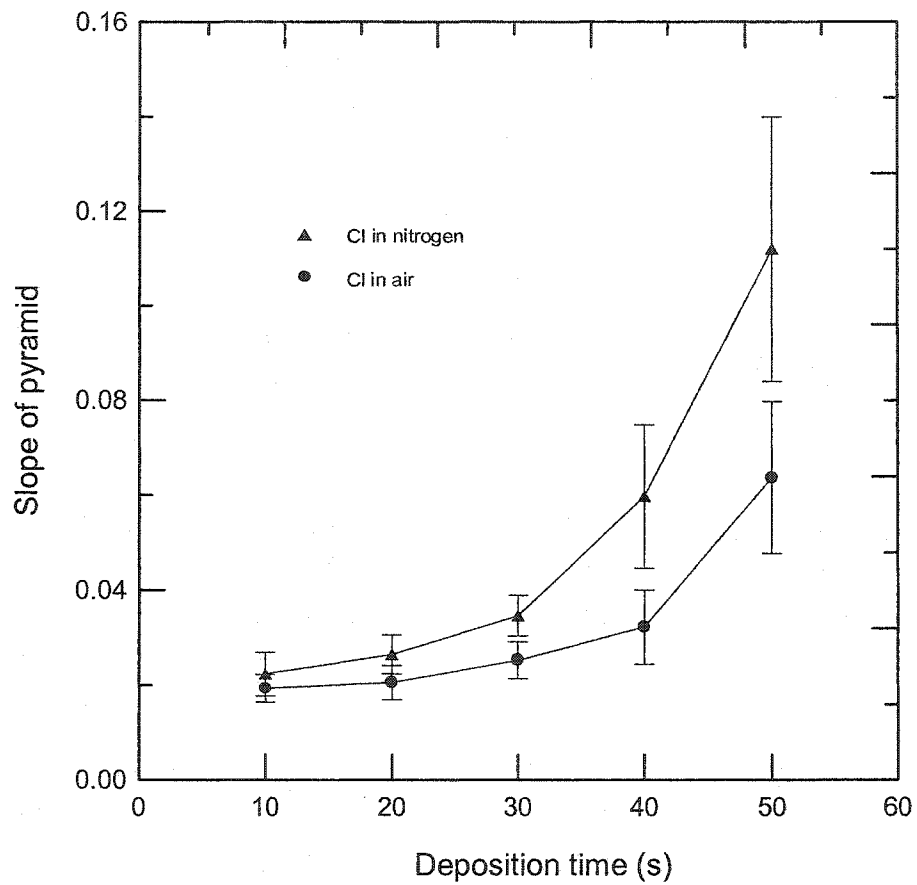
Figure 4.22 Average slope of pyramids versus deposition time with deposits formed in Cl⁻ solution.

Table 4.5 Correlation of the pyramid, cone and hemisphere templates with deposits formed in air-saturated Cl⁻+BTA solution for two deposition experiments.

	Deposition time (s)	Aspect ratio of hemisphere	Hemisphere corr. coeff.	Cone corr. coeff.	Pyramid corr. coeff.
#1	10	0.0891 ±0.0179	0.919	0.784	0.768
	20	0.1549 ±0.0256	0.921	0.814	0.801
	30	0.2045 ±0.0236	0.929	0.816	0.784
	40	0.2454 ±0.0321	0.925	0.796	0.784
	50	0.2839 ±0.0364	0.935	0.788	0.777
#2	10	0.0631 ±0.0119	0.915	0.792	0.776
	20	0.0934 ±0.0102	0.927	0.792	0.776
	30	0.1259 ±0.0125	0.923	0.810	0.800
	40	0.1652 ±0.0193	0.917	0.812	0.804
	50	0.2061 ±0.0240	0.920	0.801	0.793

Table 4.6 Correlation of the pyramid, cone and hemisphere templates with deposits formed in deaerated Cl⁻+BTA solution for two deposition experiments.

	Deposition time (s)	Aspect ratio of hemisphere	Hemisphere corr. coeff.	Cone corr. coeff.	Pyramid corr. coeff.
#1	10	0.1054 ±0.0148	0.930	0.799	0.785
	20	0.1748 ±0.0204	0.928	0.802	0.789
	30	0.2307 ±0.0474	0.922	0.811	0.799
	40	0.2907 ±0.0512	0.932	0.807	0.799
	50	0.3592 ±0.0647	0.928	0.821	0.809
#2	10	0.2325 ±0.0207	0.950	0.771	0.755
	20	0.2796 ±0.0244	0.936	0.790	0.776
	30	0.3172 ±0.0380	0.928	0.793	0.780
	40	0.2907 ±0.0451	0.930	0.803	0.793
	50	0.3973 ±0.0600	0.935	0.804	0.794
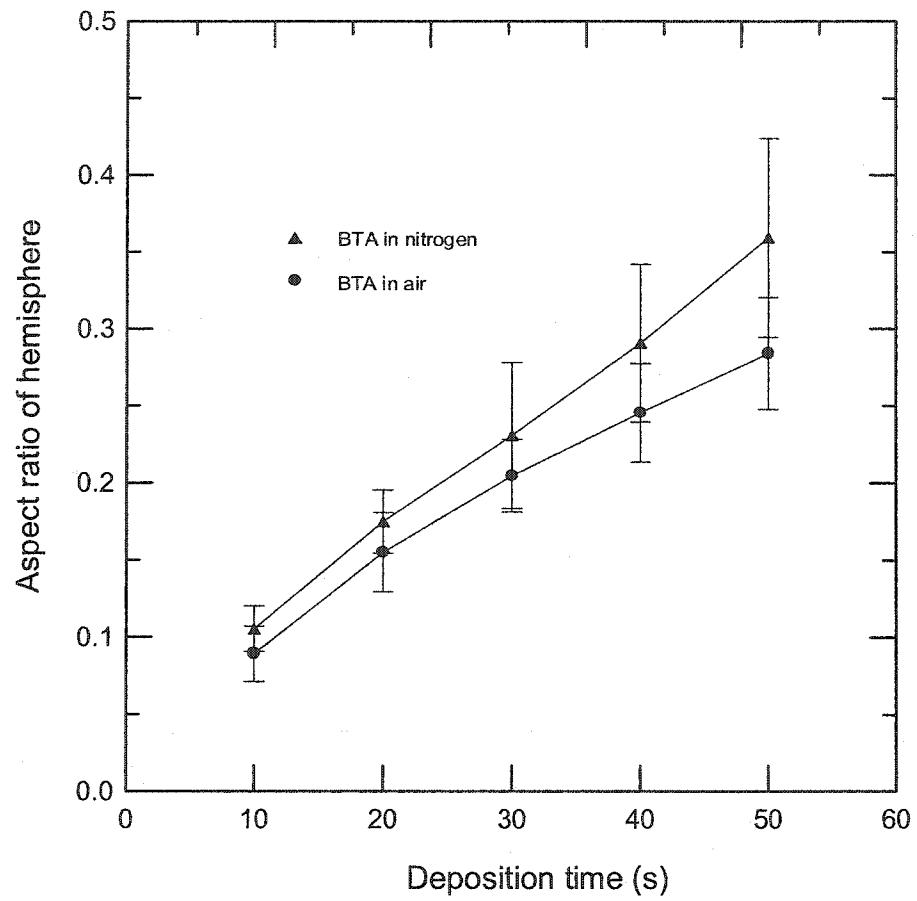
Figure 4.23 Average aspect ratio of hemispheres versus deposition time with deposits formed in Cl⁻+BTA solution.

Table 4.7 Correlation of the pyramid, cone and hemisphere templates with deposits formed in air-saturated Cl⁻+MPSA solution for two deposition experiments.

	Deposition time (s)	Hemisphere corr. coeff.	Cone corr. coeff.	Pyramid corr. coeff.
#1	10	0.867	0.877	0.879
	20	0.865	0.874	0.874
	30	0.861	0.868	0.872
	40	0.860	0.873	0.870
	50	0.868	0.881	0.865
#2	10	0.856	0.869	0.856
	20	0.852	0.872	0.861
	30	0.863	0.878	0.868
	40	0.858	0.870	0.859
	50	0.866	0.877	0.870

Table 4.8 Correlation of the pyramid, cone and hemisphere templates with deposits formed in deaerated Cl⁻+MPSA solution for two deposition experiments.

	Deposition time (s)	Hemisphere corr. coeff.	Cone corr. coeff.	Pyramid corr. coeff.
#1	10	0.870	0.878	0.890
	20	0.858	0.866	0.882
	30	0.862	0.868	0.882
	40	0.855	0.862	0.876
	50	0.854	0.859	0.871
#2	10	0.867	0.873	0.883
	20	0.861	0.870	0.880
	30	0.858	0.866	0.874
	40	0.853	0.863	0.877
	50	0.871	0.860	0.873

88

4.3.4 Mound Formation and the Effect of Organic Additives

Square-pyramidal mounds have been produced in epitaxial growth of the Cu(100) surface during both electrodeposition [92][93] and molecular beam epitaxy.[94] In the present study, square-pyramidal mounds were observed during copper electrodeposition on Cu(100) surface in the acid sulfate plating solution containing Cl⁻.

The theoretical interpretation of the mounding phenomenon has often been based on the step-edge diffusion bias[89] or the so-called Ehrlich-Schwoebel barrier (ES barrier) effect.[95][96] The basic idea of the ES barrier-induced mounding (often referred to as an instability) is simple: ES effect produces an additional energy barrier for diffusing adatoms on terraces from coming 'down' toward the layer below, thus inhibiting attachment of atoms to lower or down-steps and enhancing their attachment to upper or up-steps. The result is therefore mound formation because deposited atoms cannot come down from upper to lower terraces and so three-dimensional mounds or pyramids result as atoms are deposited on the top of already existing terraces. Furthermore, the slope of the mounds remains essentially constant and is determined by material parameters and growth conditions.[94]

There are other proposed mechanisms that lead to mounding without any explicit ES barrier. One of them invokes[97] a preferential attachment to up-steps compared with down-steps (the so-called 'step-adatoms' attraction), which, in effect, is equivalent to having an ES barrier because the attachment probability to down-steps is lower than that to up-steps exactly as it is in the regular ES barrier case. These two *energetic* mechanisms are physically indistinguishable. The second mounding alternative[98][99], which is a purely topologic-kinetic effect, is the so-called *step-edge-diffusion*-induced mounding,

89

where diffusion of adatoms around step edges is shown to lead to mound formation during surface growth in the absence of any finite ES barrier. More recently, Das Sarma et al.[100] used the *limited-mobility* surface diffusion model to explore the kinetic mechanism leading to mound formation.

All these theoretical models suggest that a kinetic instability amplifies the mounds under some growth conditions. The instability may appear if there exist energetic barriers to surface diffusion across steps, short-range interactions between adatoms and steps, a step-edge diffusion process or limited-mobility surface diffusion. Depending on the mechanism of surface diffusion and attachment of adatoms, the slope of the mounds may approach a steady state or 'selected' value.

In the present experiments, electrodeposition of copper on the Cu(100) surface in the acid sulfate copper plating solution containing only a low concentration of chloride produces square-pyramidal mounds. Theoretical models that predict pyramidal mounds invoke a diffusion process on a surface with well-defined steps. Because chloride stabilizes the Cu(100) surface, it imposes a step excess free energy resulting in the formation of planar regions interrupted by steps oriented along the 100 direction. The appearance of mounds on this surface in the present experiments conforms to predictions of models based on well-defined steps and surface diffusion. However, the results of pattern-recognition analysis indicate that mound slope increases with deposition time up to 1.5 C/cm^2 with no indication of slope selection (see Figure 4.22).

Because this type of kinetic instability to the growth of square-pyramidal mounds arises through surface processes, organic additives that are adsorbed during electrodeposition likely influence or suppress the formation of mounds. In our

90

experiments, addition of BTA to the plating solution eliminates mound formation in favor of nucleation-limited hemispheroidal growth centers whose height to base radius aspect ration increases linearly with deposition time, while MPSA produces an intermediate surface structure that does not correlate with either pyramidal or hemispheroidal templates.

Thus, the Cl^- solution produces expitaxial growth that is unstable to mound formation. BTA strongly inhibits the surface and forces growth to proceed by nucleation of growth centers. MPSA modifies crystal growth, but to a lesser degree than does BTA.

4.3.5 Effect of Oxygen on Growth Mechanism of Copper Electrodeposits

When oxygen is present in acid copper sulfate solution, it consumes the cuprous ion according to reaction (2.14). At high deposition rates where the cuprous ion concentration at the surface is low, oxygen does reach the interface and is reduced in competition with copper ions.[101] While it generally constitutes a small fraction of the deposition current, it may have an effect on discharge kinetics and surface growth.[102] The kinetic study conducted by our group has shown that the exchange current density on Cu(100) is larger in the oxygen-free solution that that in the oxygenated system.[55]

As shown in Figures 4.9 to 4.20, in all four studied solutions, deposition in dearated solution results in a larger surface width than deposition in air-saturated system. Also, pattern-recognition analysis shows that the slope of mounds formed in dearated Cl^- solution is larger for the same deposition time and increases faster than that in air-saturated Cl^- solution (Firgure 4.22). The same observation is obtained for the aspect ratio of hemispheres formed in dearated and air-saturated Cl^-+BTA solutions (Figure 4.23).

91

These results indicate that roughening of copper deposits in oxygen-free solution is faster than in oxygen rich solution. The results of scaling analysis and pattern-recognition analysis are in agreement with kinetic studies conducted by other researchers.

According to Table 4.1, the presence of dissolved oxygen in solutions does not remarkably affect values of the scaling exponent α for either solution. Although there is slight decrease in values of the growth exponent β, the presence of dissolved oxygen does not change the mechanisms of kinetic roughening of copper electrodeposition under studied conditions.

92

Chapter 5

CONCLUSIONS

Electrodeposition of copper in acid copper sulfate solutions with and without additives and/or dissolved oxygen was investigated on a copper single crystal surface with the orientation of (100) by means of atomic force microscopy (AFM) under galvanostatic pulse-current conditions. In addition to insights obtained by inspecting AFM images directly, quantitative information was extracted from AFM images. Scaling analysis and pattern-recognition analysis procedures were performed to provide a quantitative description of the effect of additives on copper electrodeposition.

In additive-free solutions copper deposits grew in a layer-by-layer mode from the earliest stage of deposition. The surface consisted of smooth terraces separated by steps. In Cl$^-$ containing solutions, at the early stages of deposition, the shape of the deposits was not well defined, but later the larger features developed very regular geometric shape. The deposits consisted of square pyramidal mounds. As more copper was deposited, the size of individual features increased, but no additional features formed after the formation of the initial ones. For Cl$^-$+BTA solutions, nucleation and growth of three-dimensional nodules started randomly across the entire surface. The number of growth centers did not increase during the deposition, and initial nodules did not merge with neighboring nodules. Compared to the very large pyramids formed in a solution containing only Cl$^-$,

93

the nodules were smaller in size. The number and density of nodules were much higher. In Cl⁻+MPSA solutions, deposits consisted of flat-topped mounds, which appeared to be intermediates between the clearly defined four-sided pyramids seen in Cl⁻ solution and the rounded nodules seen in Cl⁻+BTA solutions. The symmetry of the underlying metal surface was visible, but distinct pyramids did not appear.

The development of galvanostatic electrode surfaces was well described by a self-affine scaling process. The scaling and growth exponents (α, β) were different for each electrodeposition system. The values of α and β obtained from additive-free deposition were close to those predicted by the "WV+step-flow" model. It suggested that the scaling analysis result for this system was consistent with a process dominated by surface diffusion and step growth. For a solution containing Cl⁻, the values of α and β were similar to those obtained in the additive-free system and represented a similar scaling behavior, but indicated that surface diffusion was more dominant compared to the case of additive-free. The growth exponent β, calculated for deposition from BTA+Cl⁻ solutions, was large and close to the stochastic limit($\beta = 0.5$). The large β was suggestive of a roughening mechanism that can be described by the random roughening term of the stochastic model. The scaling exponent α, obtained for deposition from MPSA+Cl⁻ solutions, was close to 1 which is the value predicted for the case where the only smoothing mechanism is that of surface diffusion. However, β was smaller than the value predicted by the surface diffusion growth model. None of the existing models described sufficiently the surface growth mechanism for this case.

Pattern-recognition analysis of AFM images was a useful tool for identifying and characterizing the scale and shape of surface features. It has been used to demonstrate a

94

kinetic instability to mound formation on Cu(100). In acid-sulfate copper plating solution containing a low concentration of chloride, deposition of copper on the Cu(100) surface produced square-pyramidal mounds. Mound slope increased with deposition time up to 1.5 C/cm^2 with no indication of slope selection. Addition of BTA to the plating solution eliminated mound formation in favor of nucleation-limited hemispheroidal growth centers whose height to base radius aspect ratio increased linearly with deposition time. MPSA produced an intermediate surface structure that did not correlate with either pyramidal or hemispheroidal templates. The chloride solution thus produced epitaxial growth that was unstable to mound formation. BTA strongly inhibited the surface and confined growth to nucleation-limited centers. MPSA modified crystal growth, but to a lesser degree than did BTA.

Roughening of copper deposits in oxygen-free system was faster than in oxygen system. The results of scaling analysis and pattern-recognition analysis were in agreement with kinetic studies. The presence of dissolved oxygen in solutions did not remarkably affect the scaling behavior for each examined solution. Although there was slight decrease in values of the growth exponent β, the presence of dissolved oxygen did not change the mechanisms of kinetic roughening of copper electrodeposition under studied conditions.

95

Apendix A

DETERMINATION OF EQUILIBRIUM COMPOSITION

A.1 Thermodynamic Equilibrium Condition

The copper deposition reactions at acidic sulfate solution in the presence of chloride ions probably proceed as

$$Cu^{2+} + 2Cl^- + e^- \longrightarrow CuCl_2^- \qquad (A.1)$$

$$CuCl_2^- + e^- \longrightarrow Cu + 2Cl^- \qquad (A.2)$$
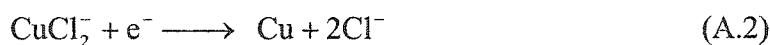
The Nernst equation gives the equilibrium potential E_{eq} for reaction (A.1) and (A.2):

$$E_{A1,eq} = E_{A1}^\theta - \frac{RT}{F} \ln\left(\frac{\{CuCl_2^-\}}{\{Cu^{2+}\}\{Cl^-\}^2} \right) \qquad (A.1a)$$

$$E_{A2,eq} = E_{A2}^\theta - \frac{RT}{F} \ln\left(\frac{\{Cu\}\{Cl^-\}^2}{\{CuCl_2^-\}} \right) \qquad (A.2a)$$

where E^θ is the standard potential, { } denotes activity [ ] denotes concentration. Activity is dimensionless, whereas concentration has units of moles/liter. If the activities of the ionic species are such that the equilibrium potential of reaction (A.1) equals that of

96

reaction (A.2), both reactions can be in equilibrium simultaneously and under this condition the metal and solution are in equilibrium.

The Gibbs free energy change for reaction (A.1) and (A.2) is calculated using the standard Gibbs free energy of formation data from Bard.[103]

$$\Delta G_f^0 (CuCl_2^-) = -240.5 kJ / mol \tag{A.3}$$

$$\Delta G_f^0 (Cu^{2+}) = 65.7 kJ / mol \tag{A.4}$$

$$\Delta G_f^0 (Cl^-) = -131.0563 kJ / mol \tag{A.5}$$

Therefore, the standard Gibbs free energy changes for reaction (A.1) and (A.2)

$$\Delta G_{A1}^0 = \Delta G_f^0 (CuCl_2^-) - \Delta G_f^0 (Cu^{2+}) - 2\Delta G_f^0 (Cl^-) \tag{A.6}$$

$$\Delta G_{A1}^0 = -240.5 - 65.7 - 2(-131.0563) = -44.087 kJ / mole$$

$$\Delta G_{A2}^0 = \Delta G_f^0 (Cu) + 2\Delta G_f^0 (Cl^-) - \Delta G_f^0 (CuCl_2^-) \tag{A.7}$$

$$\Delta G_{A2}^0 = 0 + 2(-131.0563) - (-240.5) = -21.613 kJ / mole$$

Then, standard potential can be calculated from the standard Gibbs free energy change. Standard potential for reaction (A.1)

$$E_{A1}^\theta = \frac{-\Delta G_{A1}^0}{nF} \tag{A.8}$$

$$E_{A1}^\theta = \frac{(44.087 kJ / mole)(1000 J / kJ)(V / J / C)(1000 mV / V)}{(1 eq / mole)(96485 C / eq)}$$

97

$$E^{\theta}_{A1} = 457mV$$

Standard potential for reaction (A.2)

$$E^{\theta}_{A2} = \frac{-\Delta G^{0}_{A2}}{nF} \tag{A.9}$$

$$E^{\theta}_{A1} = \frac{(21.613kJ/mole)(1000J/kJ)(V/J/C)(1000mV/V)}{(1eq/mole)(96485C/eq)}$$

$$E^{\theta}_{A1} = 224mV$$

At equlibrium, $E_{A1,eq} = E_{A2,eq}$, equating equation (A.1a) and (A.2a) yield:

$$E^{\theta}_{A1} - \frac{RT}{F}\ln\left(\frac{\{CuCl^{-}_{2}\}}{\{Cu^{2+}\}\{Cl^{-}\}^{2}}\right) = E^{\theta}_{A2} - \frac{RT}{F}\ln\left(\frac{\{Cu\}\{Cl^{-}\}^{2}}{\{CuCl^{-}_{2}\}}\right) \tag{A.10}$$

$$\frac{RT}{F} = 25.69mV$$

$$457mV - (25.69mV)\ln\left(\frac{\{CuCl^{-}_{2}\}}{\{Cu^{2+}\}\{Cl^{-}\}^{2}}\right) = 224mV - (25.69mV)\ln\left(\frac{\{Cu\}\{Cl^{-}\}^{2}}{\{CuCl^{-}_{2}\}}\right)$$

assuming unit activity of copper metal, the above equation can be simplified to

$$\ln\left(\frac{\{CuCl^{-}_{2}\}^{2}}{\{Cu^{2+}\}\{Cl^{-}\}^{4}}\right) = 9.07 \tag{A.11}$$

98

A.2 Stability Constants

When copper metal is exposed to a chloride solution, the copper metal corrodes to form various cuprous and cupric chloride complexes. The cuprous ion is very unstable and reacts with chloride ions to form many cuprous complexes. The principal cuprous species are $CuCl_2^-$, $CuCl_3^{2-}$, with Cu^+, CuCl and $Cu_2Cl_4^{2-}$, comprising a small fraction of the total species. The most prevalent cupric complex is $CuCl^+$, with $CuCl_2$, $CuCl_3^-$, and then $CuCl_4^{2-}$ encompassing a decreasing fraction of the total cupric complexes, respectively. If the production of the concentration of uncomplexed cuprous ions and uncomplexed chloride ions exceeds the solubility product constant, K_{sp}, a solid precipitate of cuprous chloride is formed. Cuprous chloride is sparingly soluble in chloride solutions. To calculate the electrolyte equilibrium composition the following species were considered: Cu^+, Cu^{2+}, Cl^-, $(CuCl)_{aq}$, $CuCl_2^-$, $CuCl_3^{2-}$, $Cu_2Cl_4^{2-}$, $CuCl^+$, $CuCl_2$, $CuCl_3^-$, and $CuCl_4^{2-}$.

Stability constants are applied in complex formation reactions and are analogous to equilibrium constants, except they are based on concentration, not activity, and are valid for a given ionic strength. All stability constants referenced below are valid at an ionic strength of $5.0M$. The ionic strength I_s of an electrolyte solution is defined as follows:

$$I_s = \frac{1}{2} \sum z_i^2 C_i \qquad (A.12)$$

where n_i is the charge number of species i, n is the total number of ionic species and C_i is the concentration of species i. The ionic strengths of the electrolyte solution is 3.8M for 0.2M $CuSO_4$/1.0M H_2SO_4/1.0mM HCl.

The cuprous stability constants are taken from Smith and Martell.[104][105]

99

$$[Cu^+][Cl^-] = 4.169 \times 10^{-8} = K_{sp} \qquad (A.13)$$

$$\frac{[CuCl]}{[Cu^+][Cl^-]} = 501.2 = K_1 \qquad (A.14)$$

$$\frac{[CuCl_2^-]}{[Cu^+][Cl^-]^2} = 1.15 \times 10^6 = K_2 \qquad (A.15)$$

$$\frac{[CuCl_3^{2-}]}{[Cu^+][Cl^-]^3} = 1.0 \times 10^6 = K_3 \qquad (A.16)$$

$$\frac{[Cu_2Cl_4^{2-}]}{[Cu^+][Cl^-]^4} = 1.0 \times 10^{13} = K_4 \qquad (A.17)$$

The cupric stability constants are taken from Ramette.[106][107]

$$\frac{[CuCl^+]}{[Cu^{2+}][Cl^-]} = 2.31 = K_5 \qquad (A.18)$$

$$\frac{[CuCl_2]}{[Cu^{2+}][Cl^-]^2} = 0.65 = K_6 \qquad (A.19)$$

$$\frac{[CuCl_3^-]}{[Cu^{2+}][Cl^-]^3} = 0.38 = K_7 \qquad (A.20)$$

$$\frac{[CuCl_4^{3-}]}{[Cu^{2+}][Cl^-]^4} = 0.082 = K_8 \qquad (A.21)$$

A.3 Chloride Ion Mass Balance

A chloride ion mass balance yields:

$$[Cl^-]_{Total} = [Cl^-]_{free} + [CuCl]_{aq} + 2[CuCl_2^-] + 3[CuCl_3^{2-}] + 4[Cu_2Cl_4^{2-}] +$$
$$[CuCl^+] + 2[CuCl_2] + 3[CuCl_3^-] + 4[CuCl_4^{2-}] \qquad (A.22)$$

100

A.4 Electroneutrality

The electroneutrality condition yields:

$$\sum n_i C_i = 0$$

$$[Cu^+] + 2[Cu^{2+}] - [Cl^-]_{free} - [CuCl_2^-] - 2[CuCl_3^{2-}] - 2[Cu_2Cl_4^{2-}] +$$
$$[CuCl^+] - [CuCl_3^-] - 2[CuCl_4^{2-}] + [H^+] - 2[SO_4^{2-}] = 0 \qquad (A.23)$$

A.5 Solution Techniques

The equilibrium concentrations are solved simultaneously using four cuprous stability constant equations, four cupric stability constant equations, a chloride mass balance equation and the electroneutrality condition. To determine the equilibrium composition, the system at equilibrium is assumed free of any solid precipitate of cuprous chloride. Then equations (A.11) and (A.14) through (A.23) are solved simultaneously. The resulting concentration of free cuprous ions and free chloride ions are inserted into equation (A.13), the solubility product equation for CuCl. If the solubility product od cuprous and chloride ions is smaller than the saturation value, the assumption of no precipitate is valid. Otherwise, the solid CuCl must be taken into account.

For the electrolyte 0.2M CuSO$_4$/1.0M H$_2$SO$_4$/1.0mM HCl, the following species are present at equilibrium: Cu$^+$, Cu^{2+}, Cl$^-$, (CuCl)$_{aq}$, CuCl$_2^-$, CuCl$_3^{2-}$, Cu$_2$Cl$_4^{2-}$, CuCl$^+$, CuCl$_2$, CuCl$_3^-$, CuCl$_4^{2-}$, H$^+$, and SO$_4^{2-}$.

101

Define x1 through x14 as follows:

x1=[Cu$^+$]   x2=[Cu^{2+}]   x3=[Cl$^-$]

x4=[CuCl]$_{aq}$ x5=[CuCl$_2^-$]   x6=[CuCl$_3^{2-}$]

x7=[Cu$_2$Cl$_4^{2-}$]   x8=[CuCl$^+$]   x9=[CuCl$_2$]

x10=[CuCl$_3^-$]   x11=[CuCl$_4^{2-}$]   x12=[H$^+$]=2.001 M

x13=[SO$_4^{2-}$]=1.2 M   x14=[Cl$^-$]=0.001 M

Assuming unit activity coefficients equation (A.11) can be expressed as:

$$\ln\left(\frac{[CuCl_2^-]^2}{[Cu^{2+}][Cl^-]^4}\right) = 9.07 = \ln\left(\frac{(x5)^2}{(x2)(x3)^4}\right)$$

Taking the exponential of both sides of the above equation yields:

$$\frac{[CuCl_2^-]^2}{[Cu^{2+}][Cl^-]^4} = e^{9.07} = 8690.624 = \frac{(x5)^2}{(x2)(x3)^4} = \beta$$

and can be written as:

$$\beta(x2)(x3)^4 - (x5)^2 = 0 \tag{A.11a}$$

$$\frac{[CuCl]}{[Cu^+][Cl^-]} = 501.2 = K_1 = \frac{(x4)}{(x1)(x3)} \tag{A.14}$$

$$(K_1)(x1)(x3) - (x4) = 0 \tag{A.14a}$$

$$\frac{[CuCl_2^-]}{[Cu^+][Cl^-]^2} = 1.15 \times 10^6 = K_2 = \frac{(x5)}{(x1)(x3)^2} \tag{A.15}$$

$$(K_2)(x1)(x3)^2 - (x5) = 0 \tag{A.15a}$$

102

$$\frac{[CuCl_3^{2-}]}{[Cu^+][Cl^-]^3} = 1.0 \times 10^6 = K_3 = \frac{(x6)}{(x1)(x3)^3} \tag{A.16}$$

$$(K_3)(x1)(x3)^3 - (x6) = 0 \tag{A.16a}$$

$$\frac{[Cu_2Cl_4^{2-}]}{[Cu^+][Cl^-]^4} = 1.0 \times 10^{13} = K_4 = \frac{(x7)}{(x1)^2(x3)^4} \tag{A.17}$$

$$(K_4)(x1)^2(x3)^4 - (x7) = 0 \tag{A.17a}$$

$$\frac{[CuCl^+]}{[Cu^{2+}][Cl^-]} = 2.31 = K_5 = \frac{(x8)}{(x2)(x3)} \tag{A.18}$$

$$(K_5)(x2)(x3) - (x8) = 0 \tag{A.18a}$$

$$\frac{[CuCl_2]}{[Cu^{2+}][Cl^-]^2} = 0.65 = K_6 = \frac{(x9)}{(x2)(x3)^2} \tag{A.19}$$

$$(K_6)(x2)(x3)^2 - (x9) = 0 \tag{A.19a}$$

$$\frac{[CuCl_3^-]}{[Cu^{2+}][Cl^-]^3} = 0.38 = K_7 = \frac{(x10)}{(x2)(x3)^3} \tag{A.20}$$

$$(K_7)(x2)(x3)^3 - (x10) = 0 \tag{A.20a}$$

$$\frac{[CuCl_4^{3-}]}{[Cu^{2+}][Cl^-]^4} = 0.082 = K_8 = \frac{(x11)}{(x2)(x4)^4} \tag{A.21}$$

$$(K_8)(x2)(x3)^4 - (x11) = 0 \tag{A.21a}$$

$$[Cl^-]_{Total} = [Cl^-]_{free} + [CuCl]_{aq} + 2[CuCl_2^-] + 3[CuCl_3^{2-}] + 4[Cu_2Cl_4^{2-}] +$$
$$[CuCl^+] + 2[CuCl_2] + 3[CuCl_3^-] + 4[CuCl_4^{2-}] \tag{A.22}$$

103

$$(x14) = (x3) + (x4) + 2(x5) + 3(x6) + 4(x7) + (x8) + 2(x9) + 3(x10) + 4(x11) \quad \text{(A.22a)}$$

$$[Cu^+] + 2[Cu^{2+}] - [Cl^-]_{free} - [CuCl_2^-] - 2[CuCl_3^{2-}] - 2[Cu_2Cl_4^{2-}] +$$
$$[CuCl^+] - [CuCl_3^-] - 2[CuCl_4^{2-}] + [H^+] - 2[SO_4^{2-}] = 0 \quad \text{(A.23)}$$

$$(x1) + 2(x2) - (x3) - (x5) - 2(x6) - 2(x7) + (x8) - (x10) -$$
$$2(x11) + (x12) - 2(x13) = 0 \quad \text{(A.23a)}$$

The system of non-linear equations is solved with Engineering Equation Solver (EES) academic version 6.548N from F-Chart Software Inc. The solution to system of non-linear equations is:

x1=3.662x10^{-5}	x2=0.1997	x3=6.519x10^{-4}
x4=1.183x10^{-5}	x5=1.771x10^{-5}	x6=1.003x10^{-8}
x7=2.342x10^{-9}	x8=3.007x10^{-4}	x9=5.516x10^{-8}
x10=2.102x10^{-11}	x11=2.957x10^{-15}	

The product of $[Cu^+]*[Cl^-]=(x1)*(x3)=2.36118\times10^{-8}$ is less than the solubility product constant, $K_{sp}=4.169\times10^{-8}$. Therefore, the assumption that no CuCl precipitate is present at equilibrium is valid.

NOMENCLATURE

a_{ij}	Surface height of the examined image
b_{ij}	Surface height of the template
c	convolution
C	Concentration, mol/l
D	Dimension
D	Diffusion coefficient, m^2/s,
E_{eq}	Equilibrium potential, mV
E^{θ}	Standard potential, mV
F	Faraday constant, A·s/mol, or local time-average growth rate, nm/s
ΔG_f^0	Gibbs free energy of formation, kJ/mole
H,h	Surface height, nm
i	Current density, mA/cm^2
i_0	Exchange current density, mA/cm^2
i_l	Limiting current density, mA/cm^2
I_s	Ionic strength, moles/liter
k_l	Mass transfer coefficient
L	Length scale, nm
n	Number of electrons transferred
N	Molar flux, molar/m^2·s
r	Correlation coefficient
R	Gas constant, 8.31 J/mol·K

t	Deposition time, s
T	Temperature, K
V	Fluid velocity, m/s
$\tilde{V}$	Molar volume of metal, cm^3/mol
w	Surface width, nm

Greek letters

α_a	Anodic transfer coefficient
α_c	Cathodic transfer coefficient
α	Scaling exponent
β	Growth exponent
Φ	Electrode potential, V
Φ_e	Equilibrium potential, V
ϑ	Growth velocity of deposits, mm/s
η	Random fluctuating deposition rate, nm/s
η_s	Surface overpotential, V
μ	Mobility of an ion
ν	System dependent parameter defined in Eq. (4.7)
λ	System dependent parameter defined in Eq. (4.8)
ω	Constant defined in Eq. (4.9)
ρ	Constant defined in Eq. (4.10)
σ	Root mean square deviation

106

REFERENCES

[1] F.C. Walsh and M.E. Herron, *Journal of Physics D: Applied Physica*, **24**, 217 (1991).

[2] J. Newman, "Electrochemical Systems", Prentice-Hall, Englewood Cliffs, NJ (1991).

[3] W. Lorenz, *Z. Naturforsch.*, **7a**, 750 (1952).

[4] W. Lorenz, *Z. Phys. Chem.*, **202B**, 275 (1953).

[5] W. Lorenz, *Z. Phys. Chem.*, **19**, 377 (1959).

[6] W.U. Schmidt, R.C. Alkire, and A.A. Gewirth, *J. Electrochem. Soc.*, **143**, 3122 (1996).

[7] F. Family and T. Vicsek, *J. Phys. A*, **18**, L75 (1985).

[8] S. Mehdizadeh, J.O. Dukovic, P.C. Andricacos, L.T. Roman, and H.Y. Cheh, *J. Electrochem. Soc.*, **139**, 78-91 (1992).

[9] P. Bindra, S.L. Levine, W.T. Plmbley, R.R. Schaffer, J. Reid, W.L. Underkofler, and R.T. Galasco, *Metal deposition*; D.P. Seraphim, R.C. Lasky, and C.-Y. Li, Eds., McGraw-Hill , New York (1989).

[10] U. Bertocci and D.R. Turner, "Copper", in *Encyclopedia of Electrochemistry of the Elements*, Ed. A. J. Bard,Vol. 2, Ch. 6, 384, Marcel Dekker, New York (1974).

[11] U. Bertocci, *Electrochim. Acta*, **11**, 1261 (1966).

[12] E. Mattison and J.O'M. Bockris, *Trans. Faraday Soc.*, **55**, 1586 (1959).

[13] J. O'M. Bockris and M. Enyo, *Trans. Faraday Soc.*, **58**, 1187 (1962).

[14] O.R. Brown and H.R. Thirsk, *Electrochim. Acta*, **10**, 383 (1965).

[15] Q.J.M. Slaiman and W.J. Lorenz, *Electrochim. Acta*, **19**, 791 (1974).

[16] T. Hurlen, G. Ottesen, and A. Staurset, *Electrochim. Acta*, **23**, 39 (1978).

[17] J.A.Harrison, D.R. Sandbah, and P.J. Stronach, *Electrochim. Acta*, **24**, 179 (1979).

[18] H. Gerischer, *Electrochim. Acta*, **2**, 1 (1960).

[19] H.C. Albaya and W.J. Lorenz, *Z. Phys., Chem. N. F.*, **81**, 294 (1972).

[20] E. Chassaing and R. Wiart, *Electrochim. Acta*, **29**, 649 (1984).

[21] A. De Agostini, E. Schmidt, and W.J. Lorenz, *Electrochim. Acta*, **34**, 1243 (1989).

[22] D. Pletcher and F.C. Walsh, *Industrial Electrochemistry*, Chapman and Hall, New York (1990).

[23] P.C. Andricacos, *Interface*, **8**, 32 (1999).

[24] M. Schlesinger and M. Paunovic, *Modern Electroplating*, 4th ed., John Wiley & Sons, New York (2000).

[25] J.P. Healy, D. Pletcher, and M. Goodenough, *J. Electroanal. Chem.*, **338**, 155 (1992).

[26] J.P. Healy, D. Pletcher, and M. Goodenough, *J. Electroanal. Chem.*, **338**, 167 (1992).

[27] J.P. Healy, D. Pletcher, and M. Goodenough, *J. Electroanal. Chem.*, **338**, 179 (1992).

[28] J.J. Kelly and A.C. West, *J. Electrochem. Soc.*, **145**, 3472 (1998).

[29] E.E. Farndon, F.C. Walsh, and S.A. Campbell, *J. Appl. Electrochem.*, **25**, 574 (1995).

[30] C. Alonso, A.B. Salomon, and H.D. Abruna, *Z. Phys. Chem.*, **210**, 15 (1999).

[31] T.Y. Leung, M. Kang, B.F. Corry, and A. A. Gewirth, *J. Electrochem. Soc.*, **147**, 3326 (2000).

[32] H.Iwasaki and T. Yoshinobu, *Phys. Rev. B*, **48**, 8282 (1993).

[33] S. Mendez, G. Andreasen, P. Schilardi, M. Figueroa, L. Vazquez, R.C. Salvarezza, and A. J. Arvia, *Langmuir*, **14**, 2515 (1998).

[34] M.A. Schineeweiss and D.M. Kolb, *Phys. Status Solidi A*, **173**, 51 (1999).

[35] J.J. Kelly, C.Y. Tian, and A.C. West, *J. Electrochem. Soc.*, **146**, 2540 (1999).

[36] P. Scgilardi, S. Mendez, R.C. Salvarezza, and A.J. Arvia, *Langmuir*, **14**, 4308 (1998).

[37] R. Walker, R. Walker and R.C. Benn, *Electrochim. Acta*, **16**, 1081 (1971).

[38] B.S. Sheshadri and T.H.V. Setty, *Indian J. Chem.*, **11**, 927 (1973).

[39] M.J. Armstrong and R.H. Muller, *J. Electrochem. Soc.*, **138**, 2303 (1991).

[40] S.M. Mayanna ans T.H.V. Setty, *Indian J. Chem.*, **10**, 295 (1972).

[41] M.R. Vogt, R.J. Nichols, O.M. Manussen, and R.J. Behm, *J. Phys. Chem. B*, **102**, 5859 (1998).

[42] D. Thierry and C. Leygraf, *J. Electrochem. Soc.*, **132**, 1009 (1985).

[43] H.Y.H. Chan and M.J. Weaver, *Langmuir*, **15**, 3348 (1999).

[44] J. Rubim, I.G.R.Gutz, O.Sala, and W.J.Orville-Thomas, *J. Mol. Struct.*, **100**, 571 (1983)

[45] Y.M. Loshkarev, V.A. Omel'cheko, V.F. Vargalyuk, V.V. Trofimmko, L.P. Snetkova, and A.A. Rysakov, *Soviet Electrochem.*, **10**, 691 (1974).

[46] M.M. Musiani, G. Mengoli, M. Fleischmann, and R.B. Lowry, *J. Electroanal. Chem.*, **217**, 187 (1987).

[47] J.K. Prall and L.L. Shreir, *Trans. Inst. Met. Finish.*, **41**, 29 (1964).

[48] E.E. Farndon, F.C. Walsh, and S.A. Campbell, *J. Appl. Electrochem.*, **25**, 574 (1995).

[49] J.J. Kelly and A.C. West, *Electrochem. Solid-State Lett.*, **2**, 561 (1999).

[50] T.P. Moffat, J.E. Bonevich, W.H. Huber, A. Stanishevsky, D.R. Kelly, G.R. Stafford, and D. Josell, *J. Electrochem. Soc.*, **147**, 4524 (2000).

[51] Z. Shi, S. Wu, and J. Lipkowski, *J. Electroanal. Chem.*, **384**, 171 (1995).

[52] J.R. White, *J. Appl. Electrochem.*, **17**, 977 (1987).

[53] M. Braun and K. Nobe, *J. Electrochem. Soc.*, **126**, 1666 (1979).

[54] S. Yoon, M. Schwartz, and K. Nobe, *Plating & Surface Finishing*, **81**, 65 (1994).

[55] Q. Wu, PhD thesis, University of New Hampshire (1998).

[56] C.B. Ehlers, I. Villegas, and J.L. Stickney, *J. Electroanal. Chem.*, **284**, 403 (1990).

[57] G. Gunawardena, G. Hills, and I. Montenegro, *J. Electroanal. Chem.*, **184**, 357 (1985).

[58] W.F.Getchell, Master Thesis,University of New Hampshire (2001).

[59] Z. Nagy, J.P. Blandeau, N.C.Hung, L.A. Curtiss, and D.J. Zurawski, *J. Electrochem. Soc.*, **142**, L87 (1995).

[60] N. Pradhan, P.G. Krisshna, and S.C. Das, *Plating and Surface Finishing*, **83**, 56 (1996).

[61] W.H. Gauvin and C.A. Winkler, *J. Electrochem. Soc.*, **99**, 71 (1952).

[62] S. Nageswar and T.H.V. Setty, *Proc. Ind. Acad. Sci. Sect. A*, **68**, 178 (1968).

[63] S. Nageswar, *Materials Chemistry*, **4**, 169 (1979).

[64] T.P. Moffat, *Mat. Res. Soc. Symp. Proc.*, Vol. **451**, 75 (1997).

[65] T.P. Moffat, *J. Phys. Chem. B*, **102**, 10020 (1998).

[66] M.R. Vogt, F.A. Moller, C.M. Schilz, O.M. Magnussen, and R.J. Behm, *Surf. Sci.*, **367**, L33 (1996).

[67] Q. Wu and D.P. Barkey, *J. Electrochem. Soc.*, **144**, L261 (1997).

[68] Q. Wu and D.P. Barkey, *J. Electrochem. Soc.*, **147**, 1038 (2000).

[69] J.D. Reid and A.P. David, *Plating & Surface Finishing*, **74**, 66 (1987).

[70] L. Oniciu and L. Muresan, *J. Appl. Electrochem.*, **21**, 565 (1991).

[71] L.H. Jenkins, *J. Electrochem. Soc.*, **113**, 75 (1966).

[72] D.P. Barkey, F. Oberholtzer, and Q. Wu, *J. Electrochem. Soc.*, **145**, 590 (1998).

[73] A.A Gewirth and B.K. Niece, *Chem. Rev.*, **97**, 1129 (1997).

[74] G. Binnig, C. F. Quate and Ch. Gerber, *Phys. Rev. Lett.* **60**, 1314 (1988).

[75] W. M. Tong, R. S. Williams, *Annu, Rev, Phys. Chem.*, **45**, 401 (1994).

[76] J. C. Puippe and F. Leaman, *Theory and Practice of Pulse Plating*, American Electroplaters and Surface Finishers Society, Orlando, FL (1986).

[77] A.-L. Barabasi and H.E. Stanley, *Fractal Concepts in Surface Growth*, Cambridge University Press, New York (1995).

[78] Mike James, *Pattern Recognition*, John Wiley and Sons, New York (1988).

[79] H. Iwamoto, T. Yoshinobu and H. Iwasaki, *Phys. Rev. Lett.*, **72**, 4025-4028 (1994).

[80] S. Huo and W. Schwarzacher, *Phys. Rev. Lett.*, **86**, 256-259 (2001).

[81] P. Meakin, P. Ramanlal, L.M. Sander, and R.C. Ball, *Phys. Rev. A*, **34**, 5091 (1986).

[82] F. Family, *J. Phys. A*, **19**, L441 (1986).

[83] P. Meakin and R. Jullien, *Europhys. Lett.*, **4**, 1385 (1989).

[84] J. Krug and H. Spohn, *Solids Far From Equilibrium*, C. Godreche, Ed., Cambridge University Press, New York (1992).

[85] S.F. Edwards and D.R. Wilkinson, *Proc. R. Soc. London A*, **382**, 17 (1982).

[86] M. Kardar, G. Parisi, and Y.-C. Zhang, *Phys. Rev. Lett.*, **56**, 889 (1986).

[87] J.G. Amar and F. Family, *Phys. Rev. A*, **41**, 3399 (1990).

[88] D.E. Wolf and J. Villain, *Europhys. Lett.*, **13**, 389 (1990).

[89] J. Villain, *J. Phys. I*, **1**, 19 (1991).

[90] L. Vazquez, R.C. Salvarezza, and A.J. Arvia, *Phys. Rev. Lett.*, **79**, 709 (1997).

[91] M.R. Vogt, W. Polewska, O.M. Magnussen, and R.J. Behm, *J. Electrochem. Soc.*, **144**, L113 (1997).

[92] A. Damjanoovic, M. Paunovic, and J. O'M. Bockris, *J. Electroanal. Chem.*, **9**, 93 (1965).

[93] T. Hayashi, S. Higuchi, H. Kinoshita, and T. Ishida, *J. Electrochem. Soc. Japan*, **37**, 64 (1969).

[94] H.J. Ernst, F. Fabre, R. Folkerts, and J. Lapujoulade, *Phys. Rev. Lett.*, **72**, 112 (1994).

[95] R.L. Schwoebel and E.J. Shipsey. *J. Appl. Phys.*, **37**, 3682 (1966).

[96] G. Ehrlich and F.F. Hudda, *J. Chem. Phys.*, **44**, 1039 (1966).

[97] J. Amar and F. Family, *Phys. Rev. Lett.*, **77**, 4584 (1996).

[98] O. Pierre Loouis, M.R. D'Orsogna, and T.L. Eistein, *Phys. Rev. Lett.*, **82**, 3661 (1999).

[99] M.V. Ramana Murthy and B.H. Cooper, *Phys. Rev. Lett.*, **83**, 352 (1999).

[100] S. Das Sarma, P. Punyindu, and Z. Toroczkai, *Surf. Sci.*, **457**, L369 (2000).

[101] R.J. Nichols, W. Beckmann, N. Batina, and D.M. Kolb, *J. Electroanal. Chem.*, **330**, 381 (1992)

[102] J.R. LeGraff and A.A. Gewirth, *J. Phys. Chem.*, **98**, 11246 (1994).

[103] A.J. Bard, R. Parsons, and J. Jordan, "Standard Potentials in Aqueous Solutions", Marcel Dekker, NY (1985)

[104] R.M. Smith and A.E. Martell, "Critical Stability Constants, Inorganic Complexes", Volume 4, Plenum Press, NY (1976)

[105] R.M. Smith and A.E. Martell, "Critical Stability Constants, First Supplement", Volume 5, Plenum Press, NY (1982)

[106] R.W. Ramette and G. Fan, *Inorganic Chemistry*, **22**, 3323 (1983)

[107] R.W. Ramette, *Inorganic Chemistry*, **25**, 2481 (1986)